ABSTRACT

Title of Dissertation: RESPONSE OF HYPERSONIC BOUNDARY-LAYER DISTURBANCES TO COMPRESSION AND EXPANSION CORNERS

Cameron Butler
Doctor of Philosophy, 2021

Dissertation Directed by: Professor Stuart Laurence
Department of Aerospace Engineering

An experimental campaign was conducted at the University of Maryland - College Park to examine the impact of abrupt changes in surface geometry on hypersonic boundary-layer instability waves. A model consisting of a 5° conical forebody was selected to encourage the dominance of second-mode wavepackets upstream of the interaction region. Interchangeable afterbody attachments corresponding to flow deflections of -5° to +15° in 5° increments were considered. The adverse pressure gradient imposed by the +10° and +15° configurations caused the boundary layer to separate upstream, creating a region of recirculating flow. High-speed schlieren ($440 - 822\,\mathrm{kHz}$) was employed as the primary means of flow interrogation, with supplemental surface measurements provided by PCB132B38 pressure transducers. A lens calibration was applied to the images to provide quantitative fluctuations in density gradient.

The high frame rate made possible the use of spectral analysis techniques throughout the entire field of view. This analysis reveals complex growth and decay trends for incoming second-mode disturbances. Additional, low-frequency content is generated by the deflected configurations. This is most pronounced for the separated cases where distinct, shear-generated disturbances are observed. Spectral proper orthogonal decomposition (SPOD) is demonstrated as a powerful tool for resolving the flow structures tied to amplifying frequencies.

Nonlinear interactions are probed through bispectral analysis. Resonance of low-frequency structures is found to play a large role in nonlinear energy transfer downstream of the compression corners, particularly for the separated cases. Concave streamline curvature appears to result in concentrated regions of increased nonlinearity. These nonlinear interactions are shown to be spatially correlated with coherent flow structures resolved through SPOD.

Finally, a limited computational study is carried out to demonstrate the ability of linear stability theory and the parabolized stability equations to reproduce experimental results obtained for the $+10^\circ$ extension. The development of the second-mode and shear-generated disturbances resolved by the computational analysis shows excellent agreement with the experimental results.

RESPONSE OF HYPERSONIC BOUNDARY-LAYER DISTURBANCES TO COMPRESSION AND EXPANSION CORNERS

by

Cameron Butler

Dissertation submitted to the Faculty of the Graduate School of the
University of Maryland, College Park in partial fulfillment
of the requirements for the degree of
Doctor of Philosophy
2021

Advisory Committee:
Professor Stuart Laurence, Chair/Advisor
Professor James Baeder
Professor Kenneth Yu
Professor Christoph Brehm
Professor Johan Larsson

Acknowledgments

It seems appropriate to begin by thanking my advisor, Stuart Laurence, without whom this body of work would have been impossible. His guidance has proven invaluable over the past six-and-a-half years and shaped me into the researcher I am today. I would also like to extend my thanks to the members of my dissertation committee: Professors Kenneth Yu, James Baeder, Christoph Brehm and Johan Larsson. Their input led me to examine facets of this work which may otherwise have gone unexplored and what I present here is undoubtedly improved as a result.

Equally important throughout this endeavor have been my loving wife, Emily, and my beautiful dog, Korra. Having someone to celebrate in my triumphs has meant more than I can say, and I could not ask for a better partner at my side through the adventure that is life.

Thanks to all my colleagues in the High-speed Aerodynamics and Propulsion Lab. Our discussions in the lab and office made my experience at Maryland far more memorable and I count myself lucky for having worked alongside you. Special thanks to Alvin Pee for being my partner in crime getting HyperTERP in a functional state, and to Sam Maszkiewicz for his assistance in running the facility during many of the tests presented here.

Others who deserve credit in this work include the talented machinists I have relied on in designing and constructing HyperTERP and the test articles used throughout this work. Mike Perna, Bruce Rowley, Dave Cogsworth and Tommy Tamarkin have always been there to talk me through any hardware design issues, or to just shoot the breeze.

I would also like to acknowledge past mentors who have had a significant impact on my trajectory towards a PhD. I first gained a sense of self-actualization regarding research activities thanks to the guidance of Dr. Godfrey Sauti during a summer internship at NASA Langley. Under the tutelage of Dr. Eric Loth at the University of Virginia I became acquainted with CFD tools. I am a far more well-rounded researcher today thanks to his expertise.

Finally, thanks to my parents, Gail and Wayne Butler, for their love and support all my life. I know I would not be here today without them. And shouts out to my brother and one of my best friends, Chris, who I can always count on for a refreshing time.

I was supported financially by a National Defense Science and Engineering Graduate Fellowship sponsored by the Air Force Office of Scientific Research, for which I am exceedingly grateful.

Table of Contents

Acknowledgements ii

Table of Contents iv

List of Tables vi

List of Figures vii

List of Abbreviations x

Chapter 1: Introduction 1
- 1.1 Second-mode Instability 2
- 1.2 Shock-wave/Boundary-layer Interactions 5
- 1.3 Expansion Corner Interactions 9
- 1.4 Present Work 11

Chapter 2: Experimental Methodology 14
- 2.1 HyperTERP Facility 14
- 2.2 Test Conditions 18
- 2.3 Nozzle Characterization 20
- 2.4 Test Article and Instrumentation 22
- 2.5 Calibrated Schlieren 25

Chapter 3: Schlieren Observations 29
- 3.1 Straight (+0°) Extension 29
- 3.2 -5° Extension 34
- 3.3 +5° Extension 37
- 3.4 +10° Extension 42
- 3.5 +15° Extension 48

Chapter 4: Low-order Spectral Analysis 56
- 4.1 Second-mode Behavior 56
- 4.2 N Factors 64
- 4.3 Low-frequency Behavior 70
- 4.4 Bandpass-filtered Images 76

Chapter 5: Spectral Proper Orthogonal Decomposition 82

5.1 +0 ° Extension . . . 82
5.2 -5 ° Extension . . . 87
5.3 +5 ° Extension . . . 92
5.4 +10 ° Extension . . . 98
5.5 +15 ° Extension . . . 102
5.6 Propagation Speeds . . . 107

Chapter 6: Bispectral Analysis 114
6.1 +0 ° Extension . . . 118
6.2 -5 ° Extension . . . 122
6.3 +5 ° Extension . . . 126
6.4 +10 ° Extension . . . 131
6.5 +15 ° Extension . . . 136

Chapter 7: LASTRAC 142
7.1 Mean Flow . . . 144
7.2 LST Results . . . 146
7.3 LPSE Results . . . 147

Chapter 8: Conclusions 150

Bibliography 158

List of Tables

2.1 Test condition matrix. 18
2.2 PCB sensor locations. 24

3.1 +10° configuration separation/reattachment locations. 43
3.2 +15° configuration separation/reattachment locations. 48

5.1 Parameters for SPOD computations. 83
5.2 Upstream and downstream propagation speeds computed with the correlation method. 112

7.1 Inflow properties for STABL2D. 144

List of Figures

1.1 Mean flow topologies for compression and expansion corners. 5
1.2 Computational results from Balakumar et al., 2002. 8

2.1 HyperTERP schematic. 14
2.2 Schematic of double-diaphragm system. 16
2.3 Sample reservoir pressure traces at each condition. 20
2.4 Nozzle characterization results. 23
2.5 Test article schematics. 24
2.6 Alignment procedure for test article. 26
2.7 Sample alignment PCB spectra. 26
2.8 Calibration image and intensity profile. 28

3.1 +0° configuration image sequence at condition Re33. 31
3.2 +0° configuration image sequence at condition Re45. 32
3.3 +0° configuration image sequence at condition Re52. 33
3.4 +0° configuration PCB spectra. 33
3.5 -5° configuration image sequence at condition Re45. 35
3.6 -5° configuration image sequence at condition Re52. 36
3.7 -5° configuration PCB spectra. 37
3.8 +5° configuration image sequence at condition Re33. 39
3.9 +5° configuration image sequence at condition Re45. 40
3.10 +5° configuration image sequence at condition Re52. 41
3.11 +5° configuration PCB spectra. 42
3.12 +10° configuration image sequence at condition Re33. 44
3.13 +10° configuration image sequence at condition Re45. 45
3.14 +10° configuration image sequence at condition Re52. 47
3.15 +10° configuration PCB spectra. 47
3.16 +15° configuration shear-mode image sequence at condition Re33. . . 50
3.17 +15° configuration second-mode image sequence at condition Re33. . 51
3.18 +15° configuration shear-mode image sequence at condition Re45. . . 53
3.19 +15° configuration second-mode image sequence at condition Re45. . 54
3.20 +15° configuration image sequence at condition Re52. 55

4.1 High-frequency spatial PSD contours for condition Re33. 57
4.2 Pseudo-streamline spectra for condition Re33. 58
4.3 High-frequency spatial PSD contours for condition Re45. 60

4.4 Pseudo-streamline spectra for condition Re45. 61
4.5 High-frequency spatial PSD contours for condition Re52. 64
4.6 Pseudo-streamline spectra for condition Re52. 65
4.7 Pseudo-streamline N-factors for condition Re33. 67
4.8 Pseudo-streamline N-factors for condition Re45. 69
4.9 Pseudo-streamline N-factors for condition Re52. 71
4.10 Low-frequency spatial PSD contours for condition Re33. 73
4.11 Low-frequency spatial PSD contours for condition Re45. 74
4.12 Baroclinic instability production from Dwivedi et al., 2019. 74
4.13 Low-frequency spatial PSD contours for condition Re52. 75
4.14 Example of second-mode bandpass filtering. 76
4.15 Example of shear-mode bandpass filtering. 77
4.16 Shear-generated disturbance revealed for the +10° configuration. . . . 78
4.17 Low-frequency structures observed along +5° extension. 79
4.18 Second-mode harmonic revealed by bandpass-filtering. 80
4.19 Harmonic/fundamental wavelength comparison. 81

5.1 SPOD mode energy for the +0° extension. 84
5.2 SPOD mode shapes for the +0° configuration at condition Re33. . . . 85
5.3 SPOD mode shapes for the +0° configuration at condition Re45. . . . 86
5.4 SPOD mode shapes for the +0° configuration at condition Re52. . . . 87
5.5 SPOD mode energy for the -5° extension. 88
5.6 SPOD mode shapes for the -5° configuration at condition Re33. . . . 90
5.7 SPOD mode shapes for the -5° configuration at condition Re45. . . . 91
5.8 SPOD mode shapes for the -5° configuration at condition Re52. . . . 92
5.9 SPOD mode energy for the +5° extension. 93
5.10 SPOD mode shapes for the +5° configuration at condition Re33. . . . 95
5.11 SPOD mode shapes for the +5° configuration at condition Re45. . . . 97
5.12 SPOD mode shapes for the +5° configuration at condition Re52. . . . 98
5.13 SPOD mode energy for the +10° extension. 99
5.14 SPOD mode shapes for the +10° configuration at condition Re33. . . 100
5.15 SPOD mode shapes for the +10° configuration at condition Re45. . . 101
5.16 SPOD mode shapes for the +10° configuration at condition Re52. . . 102
5.17 SPOD mode energy for the +15° extension. 103
5.18 SPOD mode shapes for the +15° configuration at condition Re33. . . 104
5.19 SPOD mode shapes for the +15° configuration at condition Re45. . . 106
5.20 SPOD mode shapes for the +15° configuration at condition Re52. . . 106
5.21 Propagation speeds computed at condition Re33 using the SPOD-based methodology. 109
5.22 Second-mode propagation speeds for the -5° and +0° configurations. . 111
5.23 Second-mode propagation speeds for the +5° and +10° configurations. 113

6.1 Illustration of frequency domain for bicoherence spectra. 116
6.2 Bicoherence results from Kimmel and Kendall, 1991, and Chokani, 1999. 117

6.3 Bicoherence spectra for the +0° configuration at condition Re33. . . . 120
6.4 Spatial bicoherence contours for the +0° configuration at condition Re33. 120
6.5 Bicoherence spectra for the +0° configuration at condition Re45. . . . 121
6.6 Spatial bicoherence contour for the +0° configuration at condition Re45. 121
6.7 Bicoherence spectra for the -5° configuration at condition Re33. . . . 122
6.8 Spatial bicoherence contours for the -5° configuration at condition Re33. 123
6.9 Bicoherence spectra for the -5° configuration at condition Re45. . . . 125
6.10 Spatial bicoherence contours for the -5° configuration at condition Re45. 125
6.11 Bicoherence spectra for the +5° configuration at condition Re33. . . . 127
6.12 Spatial bicoherence contours for the +5° configuration at condition Re33. 128
6.13 Bicoherence spectra for the +5° configuration at condition Re45. . . . 129
6.14 Spatial bicoherence contours for the +5° configuration at condition Re45. 130
6.15 Bicoherence spectra for the +10° configuration at condition Re33. . . 132
6.16 Spatial bicoherence contours for the +10° configuration at condition Re33. 133
6.17 Bicoherence spectra for the +10° configuration at condition Re45. . . 135
6.18 Spatial bicoherence contours for the +10° configuration at condition Re45. 135
6.19 Bicoherence spectra for the +15° configuration at condition Re33. . . 138
6.20 Spatial bicoherence contours for the +15° configuration at condition Re33. 138
6.21 Bicoherence spectra for the +15° configuration at condition Re45. . . 140
6.22 Spatial bicoherence contours for the +15° configuration at condition Re45. 141

7.1 STABL2D computational grid. 145
7.2 Mean flow comparison to experiments. 146
7.3 LST amplification rates and N-factors. 147
7.4 LPSE eigenfunctions for second-mode disturbance. 148
7.5 LPSE eigenfunctions for shear-generated disturbance. 149

List of Abbreviations

Acronyms

CFD	Computational Fluid Dynamics
DNS	Direct Numerical Simulation
FLDI	Focused Laser Differential Interferometry
HyperTERP	Hypersonic Tunnel for Educational and Research Purposes
IT	Inner Triangle
LASTRAC	Langley Stability and Transition Analysis Code
LST	Linear Stability Theory
OT	Outer Triangle
PSD	Power Spectral Density
PSE	Parabolized Stability Equations
QPC	Quadratic Phase Coupling
RANS	Reynolds Averaged Navier Stokes
SPOD	Spectral Proper Orthogonal Decomposition
STABL	Stability and Transition Analysis for Hypersonic Boundary Layers
SWBLI	Shock-Wave/Boundary-Layer Interaction

Variables

b^2	Squared Bicoherence
F	Frequency
F_s	Sampling Frequency
L	Optical Integration Path Length
L_hann	Hann Window Length
M	Mach
n	Index of Refraction
N_f	Number of Frames
P	Pressure
R	Stability Reynolds Number
Re_m	Freestream Unit Reynolds Number
t	Time
T	Temperature
U	Velocity
X	Streamwise Surface Coordinate

Y	Vertical Coordinate
α	Complex Streamwise Wavenumber
β	Complex Azimuthal Wavenumber
ΔN	Change in N factor
δ	Boundary-Layer Thickness
ϵ	Deflection Angle
γ	Specific Heat Ratio
λ	Disturbance Wavelength
κ	Gladstone-Dale Constant
ψ	Disturbance Shape Function
ρ	Density
θ	Characteristic Vibrational Temperature
χ	Disturbance Mode Shape

Chapter 1: Introduction

Throughout the history of hypersonic flight, interest in the field has waxed and waned with global political dynamics. We currently find ourselves in a period of renewed interest, with the United States pressing for the development of highly-maneuverable hypersonic cruise vehicles. This is coupled with increasing interest within the space sector for reusable space-launch systems. The design of practical hypersonic vehicles is constrained by the extreme thermo-mechanical surface loads which occur when travelling within the stratosphere at high Mach number (typically >5). This is further complicated by the dramatic increase in surface heat-flux and skin friction which accompanies the laminar-turbulent transition of the vehicle boundary layer.

Failing to account for these factors in the design of a vehicle with a desired mission duration of minutes can have catastrophic results, as evidenced by the X-15A crash in 1967. Due to incomplete understanding of the hypersonic transition process and inadequate modelling capabilities, these issues are presently avoided by over-designed thermal protection systems; however, these come with significant weight penalties, restricting vehicle and mission design. Safe and efficient vehicle design thus requires advances in our understanding of hypersonic boundary-layer transition and the underlying physics.

1.1 Second-mode Instability

In the low-disturbance environments typical of hypersonic flight (or most ground-test facilities), the path to boundary-layer transition on slender, smooth bodies at small incidence is characterized by linear growth of instabilities within the boundary-layer leading up to nonlinear modal interactions and breakdown [5]. Early stability theory was built upon the decomposition of the Navier Stokes equations into mean and fluctuating terms and then linearizing based on the assumption of small disturbances. Disturbances here take the form

$$q(x, y, z, t) = Q(y) \exp[i(\alpha x + \beta z - \omega t)], \tag{1.1}$$

where α and β are the complex wavenumbers in the streamwise and lateral directions, respectively, and ω is the disturbance frequency. The dominant instability for sharp, near-axisymmetric configurations at low incidence and high Mach numbers is the "second mode," defined by Mack [6]. The second mode is an acoustic instability, largely consisting of density fluctuations. Furthermore, the most unstable second-mode disturbances are two-dimensional ($\beta = 0$). Early investigators [7, 8, 9] were able to obtain single schlieren images of second-mode disturbances, confirming their existence experimentally and revealing their "rope-like" structure with wavelengths of approximately twice the boundary-layer thickness. Extensive studies performed by Stetson [10] and Stetson and Kimmel [11] on a 7° half-angle cone at Mach 8 provided a characterization of second-mode behavior and variation of stability with nose bluntness, wall-cooling and Reynolds number. A particularly notable result from these tests was the appearance of the first harmonic of the second mode, which was not predicted by linear analysis. These early studies relied almost entirely on hot-wire anemometry. While this is a powerful technique capable of high bandwidths, it is necessarily intrusive and requires long test durations for a full traverse of the boundary layer.

In reviewing the effects of tunnel noise on transition, Schneider [12] noted that measurements of transition location in conventional testing facilities may not be extrapolated to flight conditions. Instead, measurements of disturbance development are needed which elucidate the physics underlying the transition process. Advances in optical technology have allowed researchers to obtain unobtrusive, time-resolved measurements of hypersonic boundary-layer instability waves through high-speed schlieren photography. Laurence et al. [13] first implemented high-speed schlieren to track individual disturbances, employing image-processing techniques to compute structural characteristics (such as disturbance wavelength) and propagation speeds. Laurence et al. [14, 15] expanded upon this work by developing a pulsed-laser schlieren apparatus, allowing image spacing as low as $2.8\,\mu$s. This removed any former ambiguity from the propagation speed calculations and providing a more detailed view of instability growth. They were also able to probe the distribution of second-mode energy as a function of wall-normal distance, observing two peaks of roughly equal magnitude: one at the wall and one at $y/\delta = 0.7 - 0.75$. Casper et al. [16] performed similar tests on a 7° cone at Mach 5 and 8. Aside from determining propagation speeds, they developed a methodology to detect the presence of second-mode wavepackets within individual images and computed intermittency curves along the model surface.

More recently, Kennedy et al. [17] implemented these image processing techniques with a calibrated schlieren setup to make global, quantitative measurements of second-mode disturbances, leading to the compution of amplification rates. Good agreement was obtained between the experimental amplification rates and computational predictions. They also employed a spatial reconstruction technique to increase the effective framerate of the tests and were able to resolve higher harmonic content generated from nonlinear resonance of the second-mode.

Piezoelectric surface pressure transducers have also proven useful for characterizing second-mode disturbances. The previously mentioned schlieren observations of Casper et al. [16] were accompanied by surface measurements from PCB132 pressure transducers. These signals were sampled at 2.5 MHz but low-pass filtered at 1 MHz. Significant broadening of the dominant second-mode peak was observed where the boundary layer was transitional. Grossir et al. [18] conducted tests on a 7° cone at Mach 10 and performed a wavelet analysis on the observed surface pressure fluctuations. They observed substantial energy content confined within a narrow spectral range which showed excellent agreement with linear stablity theory at the reported freestream conditions. They also identified harmonic content in the PCB spectra.

All this is to say that the second-mode instability is today well-characterized on simple model configurations. Unfortunately, the outer mold line of true flight

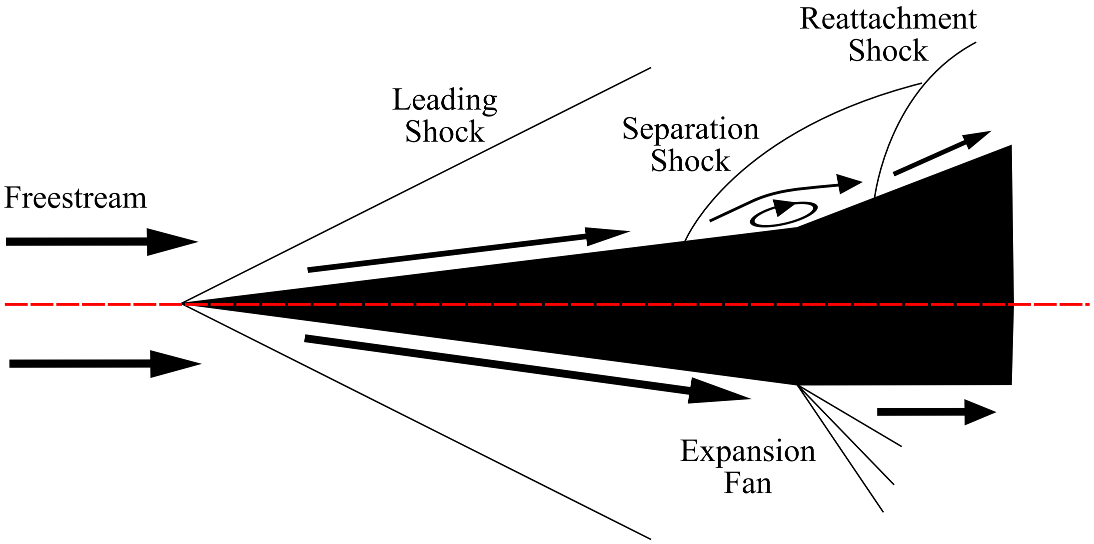

Figure 1.1: Mean flow field over a supersonic (top) compression and (bottom) expansion corner.

vehicles does not always consist of smoothly varying surfaces, and may exhibit sudden changes in geometry, e.g., at a control surface or intake. It is thus of critical importance to understand how the boundary layer and boundary-layer disturbances may interact with such configurations.

1.2 Shock-wave/Boundary-layer Interactions

When supersonic flow encounters a compression corner (positive flow deflection), an oblique shock wave forms, creating a shock-wave/boundary-layer interaction (SWBLI). This imposes an adverse pressure gradient on the incoming boundary layer which, for sufficient turning angles, will cause the boundary layer upstream of the corner to separate. This produces a complex mean flow field, illustrated by the upper portion of figure 1.1, which incoming boundary-layer disturbances must then traverse, potentially leading to complex unsteady interactions.

These SWBLIs can give rise to new instability mechanisms, particularly in the separated case. For instance, the resulting streamline curvature has been seen to induce a centrifugal instablity, leading to the formation of Görtler vortices. These vortices were first observed for compression ramps in the surface oil flow visualization of Miller et al. [19]. Researchers have since attributed surface heating streaks in reattaching flows to these streamwise-oriented vortices. The impact of ramp angle on the structure of Görtler vortices was examined by Roghelia et al. [20]. They found the length scale required for breakdown of the vortices to decrease with increasing ramp angle. A separate global instability was observed by Sidharth et al. [21] by applying global stability analysis and direct numerical simulation to the study of a 12° -22° double-wedge configuration. This global instability was found to arise from a local inviscid instability due to streamwise deceleration within the separation region. Dwivedi et al.[2] applied input-output analysis to the study of Mach 8 flow over a 15° compression ramp to investigate the development of the aforementioned heat streaks near reattachment. They observed substantial amplification of streamwise-oriented vortical disturbances of small spanwise wavelength. Furthermore, the heat streaks were found to be caused by a baroclinic instability as opposed to the oft-attributed Görtler vortices.

Much of the prior work on 2-D SWBLIs has sought to characterize transitional effects on flow topology (e.g. separation length and unsteadiness) and thermo-mechanical surface loading. Heffner, Chpoun and Lengrand [22] conducted tests on a hollow-cylinder/flare model at Mach 5 with interchangeable flares with 10° , 20° , and 30° half-angles. Critically, they confirmed the laminar state of the boundary-layer upstream of separation, resulting in a transitional SWBLI. They employed oil-flow and sublimation surface visualization techniques to obtain separation and reattachment locations and revealed the development of Görtler vortices along the flare. Surface heat-flux measurements rapidly attained turbulent levels in the vicinity of reattachment for the larger flare angles; this occurred within several boundary-layer thicknesses of reattachment for the 10° configuration. This work was expanded upon by Benay et al. [23] who took a hybrid experimental/computational approach. They focused largely on the formation of Görtler vortices, determining them to be organized, three-dimensional flow structures and not purely a transition mechanism.

Bicone models with relatively large flare angles (≥34°) have been tested in the AFRL Mach 6 Ludwieg Tube by Running et al. [24, 25], where infrared thermography was employed to study the thermal striations created by Görtler vortices. The azimuthal extent of the thermal streaks was found to increase with increasing flare angle. They also studied geometric effects, finding that increasing the nosetip bluntess or compression angle caused an increase in the separation length while increasing Re_∞ caused the separation bubble to shrink.

Focused laser differential interferometry (FLDI) measurements obtained by Benitez et al. [26] on a cone-cylinder-flare model in the Boeing/AFOSR Mach 6 Quiet Tunnel represent some of the only off-wall measurements of incoming boundary-layer instabilities in an axisymmetric SWBLI. One of the primary results from this campaign was the identification of low-frequency ($50 - 170\,\mathrm{kHz}$) travelling waves downstream of the compression corner. However, these waves were only observed under quiet flow conditions and the researchers were unable to locate these distur-

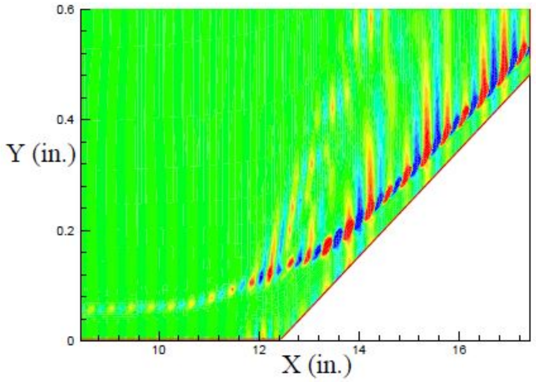

Figure 1.2: Density fluctuations computed for a low-frequency mode within the separation region taken from Balakumar et al. [1].

bances within the separation region. Furthermore, the point-like FLDI measurements give no information regarding the structure of these instabilities. Second-mode disturbances were found to amplify and increase in peak frequency along the flare.

Only a limited number of studies have elucidated transition dynamics or the impact of the SWBLI on pre-existing disturbances. Balakumar et al. [1] used both linear stability theory (LST) and direct numerical simulation (DNS) to study 2-D, fixed-frequency disturbances in a flat-plate boundary-layer encountering a 5.5° compression corner at Mach 5.373. LST revealed the existence of multiple unstable modes within narrow regions of the separation bubble, while DNS showed the second-mode waves to be of neutral stability while traversing the separated shear-layer but to grow exponentially upstream of separation and downstream of reattachment. The unstable low-frequency mode within the separaton region was found to have a frequency of 38% of the dominant second-mode frequency. This low-frequency mode was also shown to emanate energy from the boundary layer at a point just above the corner, as shown in figure 1.2.

Novikov et al. [27] carried out DNS of three-dimensional, broad-spectrum wavepackets on this same configuration. Both oblique-wave- and second-mode-dominated wavepackets were examined; the latter were found to be neutrally stable within the upstream part of the separation region before amplifying downstream. Strong forcing resulted in significant streamwise stretching of the wavepacket tail and the formation of a turbulent spot downstream of reattachment.

Transition of a laminar boundary layer encountering an axisymmetric 15° compression ramp at Mach 5 was computed by Lugrin et al. [28] using quasi-direct numerical simulation. White noise forcing was used to excite a range of convective instabilities. Spectral proper orthogonal decomposition was then applied to the unsteady results to identify key flow structures. They observed a transition scenario dominated by streamwise streaks resulting from nonlinear interaction of oblique first modes. The shear layer and reattachment regions then triggered linear amplification of these streaks, ultimately leading to breakdown.

1.3 Expansion Corner Interactions

The alternative configuration wherein the flow meets a convex corner and thus passes through an expansion fan has received comparably little attention, though it may also be encountered on high-speed vehicle configurations. In the case of a laminar boundary layer, the expansion process is generally characterized by three mechanisms: upstream influence of the corner through the subsonic portion of the boundary layer; largely inviscid flow-turning in the vicinity of the corner; and downstream interaction between the boundary layer and the external flowfield to complete the expansion process [29]. For hypersonic boundary layers with relatively mild turning angles, Sullivan theorized that the downstream interaction would dominate the process.

Sternberg performed ballistic tests on a 29° half-angle cone/cylinder model at Mach 3.02 and 3.55 both with and without boundary-layer trips, the focus of this campaign being surface recovery temperatures. In cases where the boundary layer transitioned on the cone, the surface temperature fell to levels characteristic of a laminar boundary layer for a significant region downstream of the corner before reverting to turbulent levels. Sternberg explained these results as "relaminarization" whereby the incoming turbulent boundary layer serves as the noisy "free stream" for a new laminar boundary layer which begins to grow at the corner. The significantly elevated "free stream" turbulence for this new laminar boundary layer means it is highly susceptible to transition. Shadowgraph images also revealed a qualitative reduction in the turbulence level of the incoming boundary layer due to the acceleration around the corner. This idea of "relaminarization" was strengthened by the work of Zakkay, Toba and Kuo [30] who acheived good agreement between between experimental heat-flux measurements on various cone-cylinder test articles and theoretical predications based on a laminar sub-layer model. It should be noted, however, that the relatively large cone angle employed resulted in shock-layer Mach numbers below 2 upstream of the corner for most cases. In the case examined by Zakkay, Toba and Kuo [30] where the upstream Mach number was 3.8, the downstream heat-flux more closely matched turbulent predictions. Similarly, Bloy [31] observed heat transfer rates downstream of 5-15° expansions at Mach 16 which closely approximated turbulent predictions. It is thus ambiguous to what extent this "relaminarization" occurs at higher free-stream Mach numbers.

Chung and Lu [32] found that surface pressure fluctuations for a 2-D, Mach 8 turbulent flow were attenuated by at least 40% even for small (<4.25°) expansions. A Mach 3, fully-developed, turbulent boundary layer interacting with 2-D expansion configurations was studied experimentally by Dawson, Samimy and Arnette [33]. They observed an immediate shift in surface pressure fluctuations to lower frequencies across the expansion due to the dilation of small-scale structures. The development of new $15 - 30\,\mathrm{kHz}$ features with high spanwise coherence was noted, though no physical structure could be assigned to these observations.

The prevailing theme in all these works is a bias towards turbulent boundary layers and a focus on thermo-mechanical surface loading and global flow features with little attention paid to the process of transition or incoming disturbances. There is a particularly striking lack of off-surface measurements of individual disturbances. Furthermore, the cone-cylinder models tested have historically been far from slender, resulting in relatively low Mach numbers upstream of the corner.

1.4 Present Work

The preceding discussion should make plain that there exist sizable gaps in the literature surrounding high-speed boundary-layer transition over geometries with noncontinuous surface angles. The objective of the present work is thus to improve our understanding of the interactions of hypersonic laminar boundary-layer disturbances - in particular second-mode waves - with the mean flow structures introduced by a sudden change in surface inclination. To this end, an experimental campaign was carried out in the Hypersonic Tunnel for Educational and Research Purposes (HyperTERP) at the University of Maryland - College Park, a Mach 6 reflected-shock tunnel. The forebody of the employed test article is a 5° half-angle cone, meant to promote the growth of second-mode disturbances, with a nominally sharp nosetip. We focus on compression and expansion-corner interactions with modest (-5 to +15°) turning angles. The higher compression angles were sufficient to produce flow separation at the conditions examined but still within the range that one might expect to encounter on a practical hypersonic vehicle. High-speed schlieren is employed as the primary means of flow interrogation to provide a global view on instability development. This is supplemented by high-speed surface pressure fluctuations.

While the experimetal data set obtained throughout this study is of lower quality than could be expected in a conventional (non-impulse) or quiet facility, we demonstrate powerful image analysis techniques enabled by the extremely high frame rates employed ($440 - 822\,\mathrm{kHz}$). After providing details about the experimental apparatus in chapter 2, the general, qualitative development of disturbances observed for each configuration is described in chapter 3. The spatial development of spectral content is then presented in chapter 4, revealing amplification and decay trends for the boundary-layer disturbances. Spectral proper orthogonal decomposition is employed to resolve coherent disturbance structures in chapter 5. Nonlinear interactions between these modal disturbances are investigated in chapter 6 through bispectral analysis. Finally, in chapter 7, experimental results are compared to numerical predictions for the +10° compression-corner.

Chapter 2: Experimental Methodology

2.1 HyperTERP Facility

All experiments were performed in HyperTERP, a small-scale tunnel operated by the University of Maryland. A schematic view of the facility, measuring approximately 15 m in length, is presented in figure 2.1. HyperTERP is operated as a reflected-shock-tunnel, consisting of a high pressure “driver” section and a low pressure “driven” section that are separated by a diaphragm block. The driven tube contains the test gas (typically air or nitrogen) and is isolated from the nozzle by a secondary diaphragm. The desired driver gas composition, which is a mixture of helium and air, is achieved according to Dalton’s Law of Partial Pressures. Filling typically takes around 15 minutes, allowing suffcient time for the driver gas to become well-mixed.

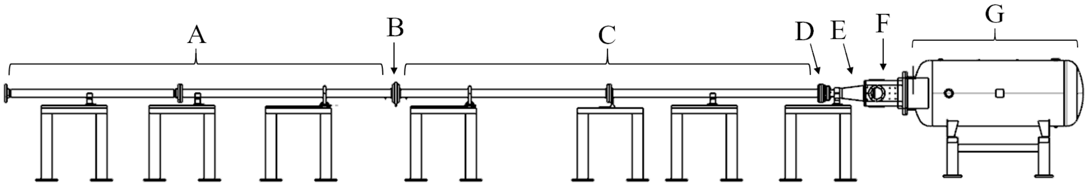

Figure 2.1: Schematic of HyperTERP with components labelled: (A) driver tube; (B) diaphragm block; (C) driven tube; (D) secondary diaphragm; (E) nozzle; (F) test section; and (G) dump tank.

The tunnel employs a modular design, allowing the nozzle and test section to be swapped out depending on experimental needs. For the present campaign, HyperTERP was equipped with a contoured Mach-6 nozzle with a 22 cm exit diameter exhausting into a 30.5 cm diameter free-jet test section. The test section was designed with four 15.2 cm diameter windows for optical access.

We employ a double-diaphragm system using polyester film (thickness of $250-500\,\mu$m), illustrated by figure 2.2, to gain precise control over the timing and repeatability of the tests. The filling procedure begins with valve A in the "open" position and valve B (an electronically-controlled solenoid) in the "closed" position, with all regions fully evacuated. The driven section is then filled with the desired test gas before we begin filling the driver. Once the driver tube is approximately halfway filled, valve A is closed; this isolates the gas in the diaphragm block and allows us to continue increasing the driver pressure to the requisite level without exceeding the burst pressure of the downstream diaphragm. To initiate a test, solenoid B is opened, exhausting the small volume of gas within the diaphragm block into the larger vacuum tank (which is separate from the facility's dump tank). This creates a pressure differential across the upstream diaphragm which causes the material to burst.

Actuating the diaphragm block thus brings the driver and test gases into contact, causing a shock wave to propagate downstream through the driven tube and an expansion wave to travel in the opposite direction. This incident shock wave then reflects off the driven-tube end wall, bursting the secondary diaphragm and creating a stagnant, high-pressure, high-temperature reservoir which can then be

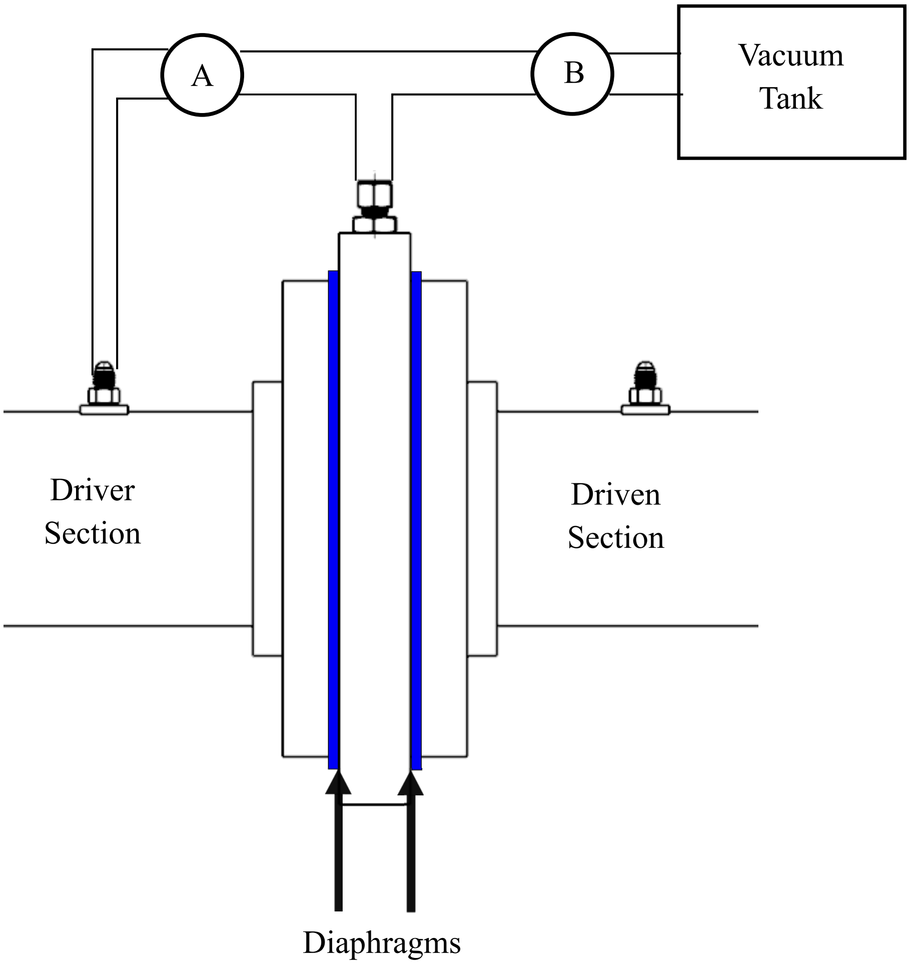

Figure 2.2: Schematic of double-diaphragm system.

expanded through the nozzle. The expansion wave likewise reflects from the driver tube end wall and eventually arrives in the reservoir, bringing the steady-state test to an end.

The propagation of the incident shock is measured by four PCB 113B26 pressure transducers sampled at 100 kHz. The sensors are located at three different stations along the driven-tube wall and the signals are conditioned using a PCB 482C05 signal conditioner. The sensor stations are positioned $186.7\,cm$, $58.4\,cm$ and $8.9\,cm$ upstream of the nozzle. The most downstream station is instrumented with two of the PCB sensors and is where the reservoir pressure is measured during a test. This shock-speed measurement provides an indirect way to determine the reservoir temperature. From the initial driven gas temperature (assumed to be room temperature), the normal shock equations will give the temperature jump caused by the incident shock. By then assuming the incident shock reflects so as to bring the induced gas velocity back to zero, the initial reservoir conditions may be calculated. Finally, the gas in this theoretical state is isentropically expanded or compressed to the instantaneous pressure recorded by the PCB sensors, yielding the instantaneous reservoir temperature. Because the air is heated substantially during this process, a calorically imperfect gas model must be implemented where the specific heat ratio varies with temperature according to

$$\gamma = 1 + \frac{\gamma_p - 1}{1 + (\gamma_p + 1)\left[(\frac{\theta}{T})^2 \frac{e^{\theta/T}}{(e^{\theta/T} - 1)^2}\right]}. \tag{2.1}$$

The subscript p here refers to the variable under a perfect-gas assumption and θ is

Condition	Re33	Re45	Re52
Re_m $[10^6/m]$	3.33	4.49	5.24
P_0 [bar]	10.0	13.5	15.8
T_0 [K]	890	890	890
U_∞ [m/s]	1266	1266	1266
P_∞ [Pa]	642	866	1006
T_∞ $[K]$	111	111	111
ρ_∞ [kg/m^3]	0.020	0.027	0.032

Table 2.1: HyperTERP test condition matrix.

the characteristic vibrational temperature of the test gas [34]. For air, a value for θ of 3056 K is a satisfactory approximation for the temperature range of interest. Note that the energy equation across a normal shock for a thermally perfect gas takes the form

$$\frac{u_2^2}{2} - \frac{u_1^2}{2} + \frac{\gamma_p}{\gamma_p - 1} R(T_2 - T_1) + R\theta \left(\frac{1}{e^{\theta/T_2} - 1} - \frac{1}{e^{\theta/T_1} - 1} \right) = 0. \tag{2.2}$$

2.2 Test Conditions

The total specific enthalpy was held approximately constant throughout the campaign at 0.89 MJ/kg, with unit Reynolds numbers of 3.33, 4.49 and 5.24×10^6 m^{-1} achieved by varying the reservoir pressure. Reservoir and corresponding freestream properties for each condition are detailed in table 2.1. Although HyperTERP is capable of reaching reservoir temperatures as high as 1400 K, this lower enthalpy configuration was selected to yield higher unit Reynolds numbers and dynamic pressures, as well as longer test durations.

To optimize campaigns conducted in HyperTERP, some effort was expended in tailoring of the facility. Tailoring refers to the proper selection of initial driver gas composition and driver-to-driven-section pressure ratio to produce a stationary contact surface, thereby achieving steady conditions in the reservoir and test section [35, 36]. If the initial conditions are improperly chosen, then additional disturbances will be produced when the reflected shock intersects the contact surface, perturbing the reservoir gas and resulting in temporal variations in the supply pressure. Over-tailoring refers to the case where the incident shock is too weak and a shock wave reflects off the contact surface, causing an increasing pressure with time. Conversely, under-tailoring results in an expansion wave propagating back into the reservoir and occurs when the incident shock is too strong. Although tailored conditions are known theoretically, shock-wave attenuation and other imperfect-shock effects mean that iteration over several facility runs is required to determine the correct fill properties.

The result of these tailoring endeavors is demonstrated by the sample reservoir pressure traces in figure 2.3 for each condition. While there is some degree of unsteadiness up until 5 ms, conditions are steady for the next 7 ms up until approximately 12 ms when the expansion wave arrives. Across all tests and conditions, the steady test time is ∼6 ms, during which the reservoir-pressure unsteadiness is typically 2% (standard deviation). Shot-to-shot variation in the mean pressure is of the order of 1.3%, while systematic uncertainty (combined calibration and nonlinearity) is estimated as 1.6%. Shock-speed estimates are accurate to ±5 m/s, contributing 0.4% uncertainty in the reservoir temperature.

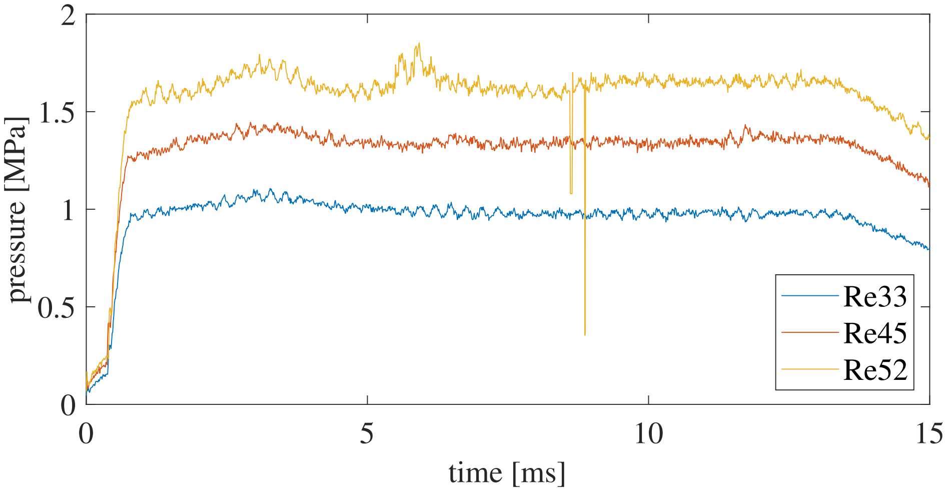

Figure 2.3: Sample reservoir pressure traces at each condition.

2.3 Nozzle Characterization

The contoured nozzle employed for this work was designed through a hybrid approach using the method of charactistics (MoC) and computational fluid dynamics (CFD). First, an inviscid nozzle contour was generated based on the rotational method of characteristics including vibrational-relaxation effects. This contour was then altered with a viscous boundary-layer correction estimated using the von Karman momentum-integral equation. This boundary-layer correction was then calibrated iteratively by comparison to axisymmetric RANS computations. A full description of this iterative procedure and implementation is given by Starshak, Butler and Laurence [37].

A limited pitot rake characterization study was performed with the rake positioned both at the nozzle exit plane and 160 mm downstream to ascertain flow uniformity at condition Re33. The rake was instrumented with an array of Kulite XCE-062 pressure transducers sampled at 100 kHz. Resulting values of P_0/P_{pitot}

as a function of radial distance from the nozzle centerline are given in figure 2.4. Included on this plot are lines corresponding to freestream Mach numbers of 5.8 and 6.0. The high reservoir temperature here again means we cannot ignore the effects vibrational excitation, leading to two theoretical scenarios for the expansion through the nozzle. The first of these assumes the gas is in vibrational equilibrium throughout the nozzle, meaning the specific heat ratio varies with temperature according to equation 2.1. The integrated form of the energy equation for a thermally perfect gas,

$$M^2 = \frac{2T_0}{\gamma T}\left[\frac{\gamma_p}{\gamma_p - 1}\left(1 - \frac{T}{T_0}\right) + \frac{\theta}{T}\left(\frac{1}{e^{\theta/T_0} - 1} - \frac{1}{e^{\theta/T} - 1}\right)\right], \tag{2.3}$$

may be used to determine the temperature at the nozzle exit for a given freestream Mach number. The pressure may then be determined from the isentropic relationship

$$\frac{P}{P_0} = \left(\frac{e^{\theta/T_0} - 1}{e^{\theta/T} - 1}\right)\left(\frac{T}{T_0}\right)^{\frac{\gamma_p}{\gamma_p - 1}} \exp\left[\left(\frac{\theta}{T}\right)\frac{e^{\theta/T}}{e^{\theta/T} - 1} - \left(\frac{\theta}{T_0}\right)\frac{e^{\theta/T_0}}{e^{\theta/T_0} - 1}\right]. \tag{2.4}$$

At these low-density conditions, however, there is a high likelihood of vibrational freezing within the nozzle. For the frozen scenario, we consider the gas to be in vibrational equilibrium up until the throat, at which point we revert to a calorically perfect gas assumption with a γ of 1.4 until the nozzle exit. The primary effect of noneqilibrium here is to increase the freestream pressure for a given Mach number, reducing the expected P_0/P_{pitot}.

Regardless of the flow model employed for the nozzle expansion, the normal shock upstream of the probe and the subsequent isentropic expansion are treated with a calorically perfect gas assumption (the calculated vibrational-relaxation time behind the shock being orders of manitude larger than the shock stand-off distance), meaning the pressure ratio is given by

$$\frac{P_{02}}{P_\infty} = \frac{(\gamma_p + 1)^2 M^2}{4\gamma_p M^2 - 2(\gamma - 1)}^{\frac{\gamma_p}{\gamma_p - 1}} \frac{1 - \gamma_p + 2\gamma_p M^2}{\gamma_p + 1}, \tag{2.5}$$

where P_{02} refers to the pressure measured by the pitot rake.

The experimental data presented in figure 2.4 most closely aligns with the frozen, Mach 6 pressure ratio; moreover, visualization of the shock generated by a sharp-edged planar ramp at various angles of incidence indicated a Mach number of 5.99 ± 0.09. In light of this and the fact that the frozen scenario is more physically realistic, it is for this condition that the freestream properties of table 2.1 are computed. This figure also shows little variation as a function of radial or streamwise location, suggesting that the core flow is fairly uniform with minimal flow divergence.

2.4 Test Article and Instrumentation

Two configurations of the primary test article are pictured in figure 2.5; both consist of a 410 mm, 5° half-angle frustum and a 76.2 mm extension. The top schematic depicts the -5° configuration, which creates a 5° expansion by employing a cylindrical afterbody. The afterbody of the lower configuration has a 15° half-angle, creating a +10° compression. Compression angles of +5° and +15° were also

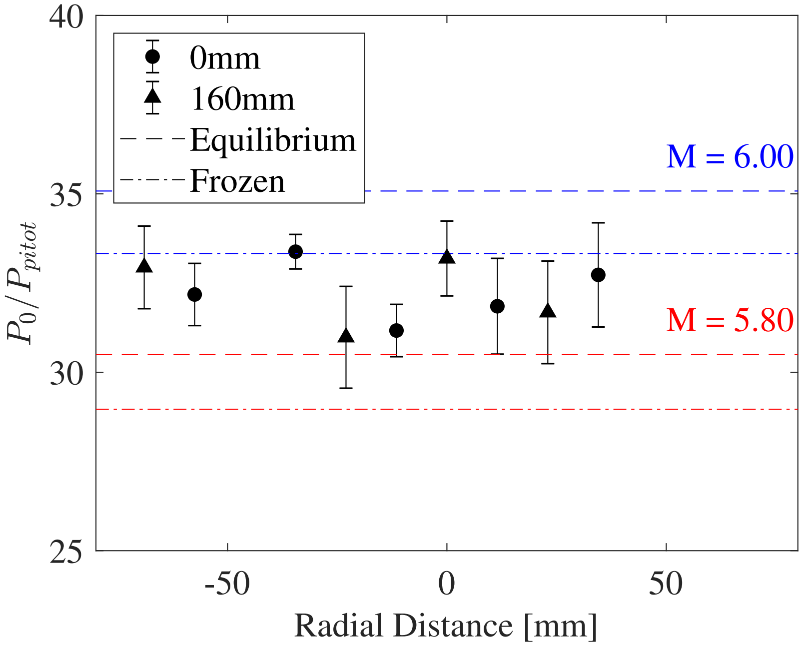

Figure 2.4: Pitot pressure ratio as a function of radial distance from the centerline.

studied, though these configurations are not pictured. A straight-cone configuration (5° half-angle extension) was tested to provide comparisons against an undisturbed boundary layer. Thus, this study includes five distinct model configurations (-5°, +0°, +5°, +10°, and +15°). The same, nominally-sharp nosetip was used in all tests; the true bluntness radius was measured to be 0.10 mm using a SmartScope optical gage.

A single streamwise row of PCB 132B38 pressure transducers was installed along the upper surface of the cone as shown in figure 2.5 (U1-D5), held in place using clear nail polish following the methodology of Ort and Dosch [38]. The surface coordinate of each station relative to the nosetip is given in table 2.2. These sensors were sampled at 2 MHz with a 600 kHz lowpass filter to remove aliasing effects, though it should be noted that [38] observed resonances at frequencies above 300 kHz

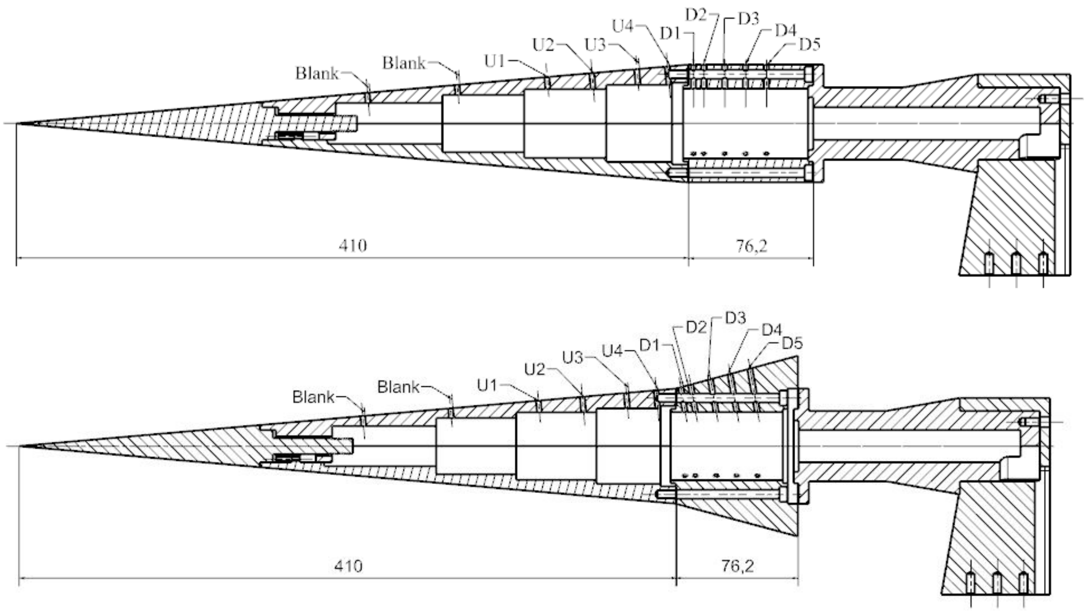

Figure 2.5: Model schematic for the (top) -5° and (bottom) +10° configurations showing sensor layout with dimensions in millimeters.

Station	U1	U2	U3	U4	D1	D2	D3	D4	D5
s [mm]	326	353	381	399	415	422	434	447	460

Table 2.2: Surface coordinate of PCB stations.

for this model. Indeed, a 300 kHz peak was observed in many of the spectra in the present experiments, and results near this frequency should be treated with caution.

The model was initially installed at approximately zero incidence by sight with the aid of a laser level, as illustrated in figure 2.6, by aligning the model seam and PCB array with the horizontal and vertical centerlines of the nozzle. Obviously, this method suffers from significant inaccuracy as it relies entirely on the researcher's eyesight. For this reason, tests were performed late in the campaign where an additional PCB sensor was instrumented on the underside of the model opposite station U1. The results from these tests were extrapolated to gain confidence in tests conducted early in the campaign. The dominant fundamental frequency of second-mode disturbances is highly sensitive to angle of attack, meaning that zero incidence is achieved when there is a frequency match between the top and bottom surfaces. Resulting spectra from two tests at condition Re45 are shown in figure 2.7 for which the angle of attack was altered by 0.3° between tests using shims. The peak frequency on the upper surface is seen to increase from 235 kHz in the left plot to 275 kHz in the right plot. The match in frequencies in the right plot suggests nearly zero incidence. The dominant second-mode frequencies observed at station U1 for all tests analyzed throughout this work (at condition Re45) were between $250-275$ kHz. Assuming the second-mode frequency varies linearly for small changes in incidence, this suggests the error in angle of attack for this study is less than 0.2°. Furthermore, because the dominant frequency is consistently below the matching frequency of 275 kHz, we can conclude that the upper surface of the model is also the leeward side throughout this work. Although no comparable corrections were made regarding model yaw, small yaw variations are expected to have a negligible effect on the flow behavior in the regions of interest.

2.5 Calibrated Schlieren

High-speed flowfield visualization was obtained from a standard Z-type schlieren with a horizontal knife-edge and serves as the primary means of flow interrogation throughout this work. Light pulses of 20 ns duration were provided by a Cavilux HF laser and a Phantom v2512 camera was used to capture the images at $440-822$ kHz, allowing resolution of spectral content up to 411 kHz. The frame rates were chosen

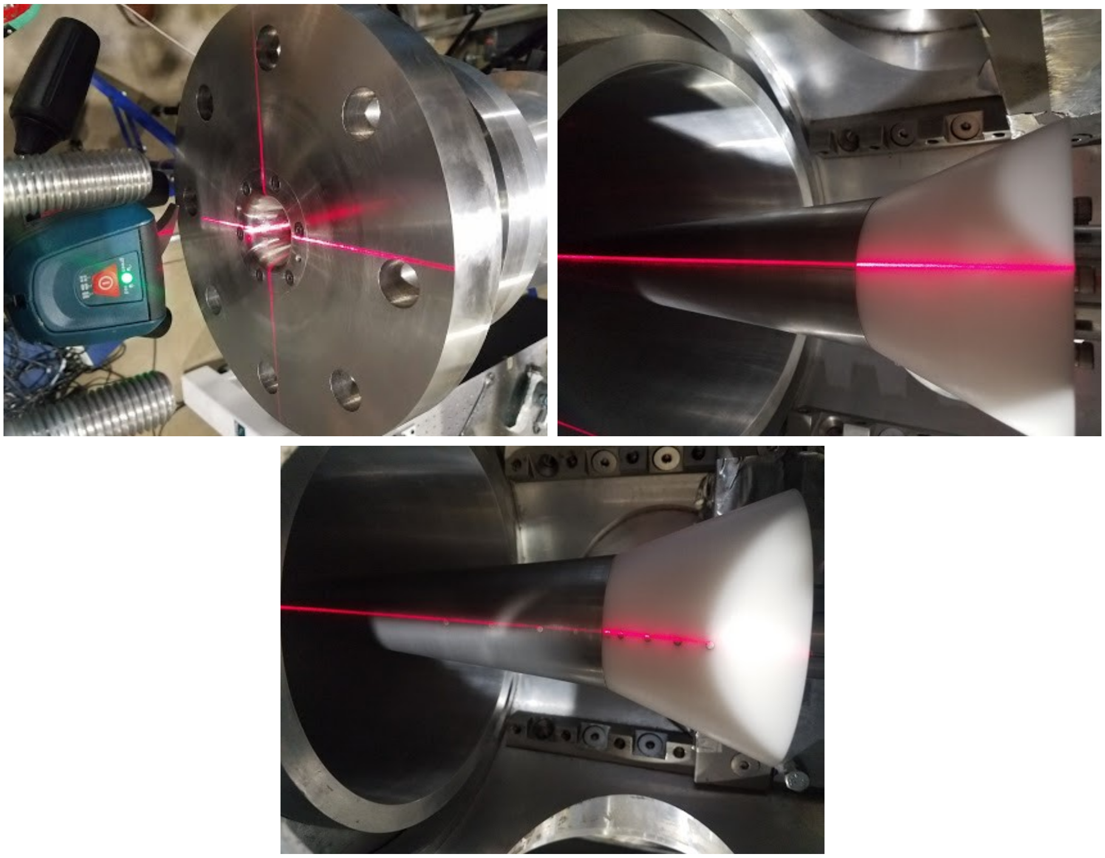

Figure 2.6: Images of the alignment procedure when installing the model.

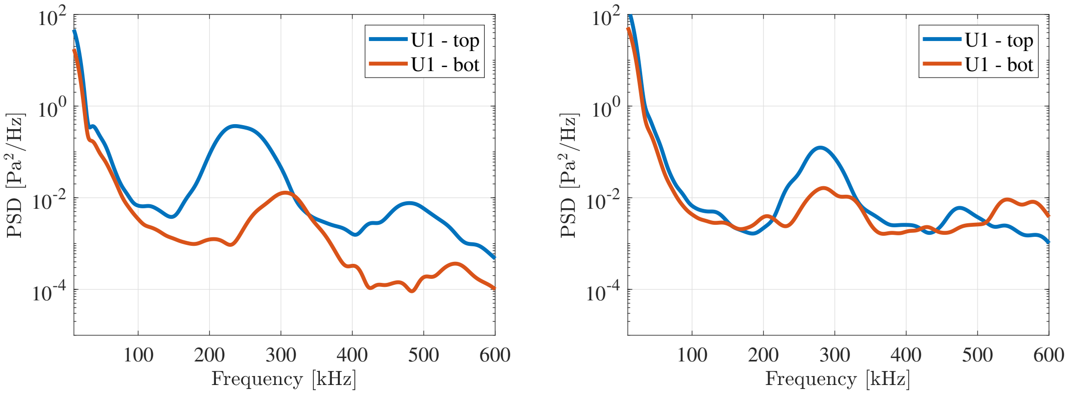

Figure 2.7: PCB spectra for the top and bottom model surfaces with the angle of attack increased by 0.3° between runs.

to be higher than the Nyquist sampling rate of the dominant boundary-layer disturbances (typically second-mode waves). The field of view ranged from 512×32 pixels at 822 kHz to 640×64 pixels at 440 kHz, with the camera rotated to maximize the region of flow visualized. The magnification of the optical setup resulted in a length scale of 0.112 mm/pixel for the -5° and +15° configurations and 0.139 mm/pixel for all others (+0° , +5° , and +10°). The theoretical, undisturbed boundary-layer thickness at the corner junction ranged from $1.44 - 1.81$ mm depending on the condition. This gives a boundary layer resolution of at least 10 pixels in the lesser magnification runs, though it should be noted that this number will be lower far upstream of the corner and along the compression flares due to the reduced boundary-layer thickness.

By using a calibration procedure described by Hargather and Settles [39] and Kennedy [40], the pixel intensities of each image were converted to density gradients. Following their implementation, a spherical lens with a known deflection angle profile was placed into the field of view and a reference image captured, as in the left image of figure 2.8. A plano-convex lens was employed for this study with a focal length, f, of 10 m and a diameter of 25.4 mm. The intensity profile along the lens face was then mapped to the known deflection profile by assuming that zero deflection corresponds to 92% of the background pixel intensity (to account for the 8% absorption specific to the calibration lens). A sample intensity profile is shown in the right image of figure 2.8. For a weak lens where the focal length is much greater than the diameter, the deflection angle, ϵ, is given as a function of radial distance from the lens center,

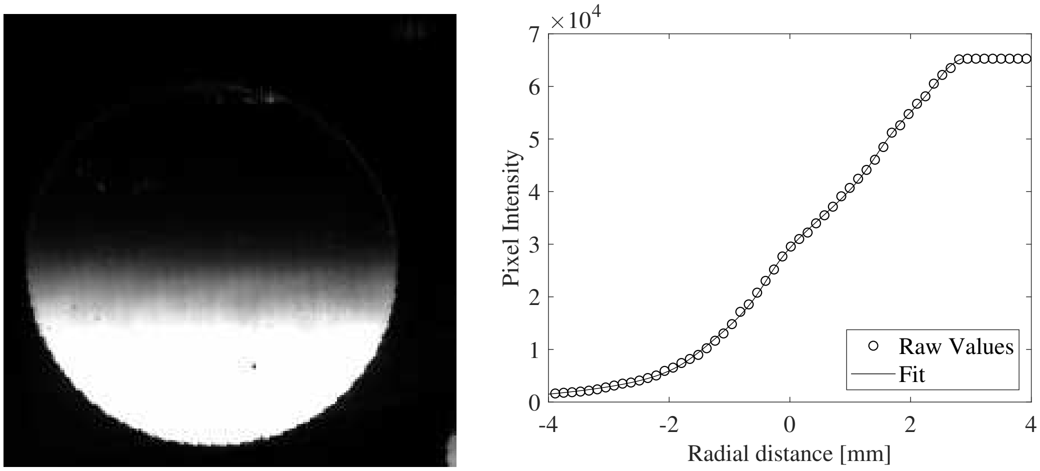

Figure 2.8: (Left) Sample calibration lens image and (right) pixel intensity profile over lens face.

r, according to

$$\frac{r}{f} = \tan\epsilon \approx \epsilon, \tag{2.6}$$

The deflection profile is then mapped to the density gradient of the test gas by

$$\epsilon = \frac{\kappa L}{n_\infty}\frac{\partial\rho}{\partial y}, \tag{2.7}$$

where L is the integration path-length of the light, κ is the Gladstone-Dale constant, ρ refers to the gas density and n_∞ is the index of refraction of air at laboratory conditions.

Chapter 3: Schlieren Observations

3.1 Straight (+0°) Extension

We begin by examining the behavior of the undisturbed boundary layer at each condition in the +0° configuration through the time-resolved schlieren sequences presented in figures 3.1, 3.2, and 3.3 with inter-image spacings of $9.7\,\mu$s, $9.4\,\mu$s, and $10.2\,\mu$s, respectively. The images have been rotated to align the abscissa with the frustum surface and X refers to the distance from the nosetip. At the top of each sequence is shown an average flow-on image to highlight the mean flow features. Subsequent images are reference-subtracted using a 40-image sliding average to emphasize transient features. Red triangles denote the locations of PCB sensors, which are labelled in the mean flow image, while red bars are used to bracket regions of interest and approximate the propagation of the disturbances. Power spectral densities (PSDs) for select PCB sensors are presented in figure 3.4 corresponding to each image sequence.

Distinct, rope-like waves are seen upstream of U3 in the first image of figure 3.1 (condition Re33), corresponding to a second-mode wavepacket, with additional second-mode content visible within the vicinity of D3. The PCB spectra show that the peak second-mode frequency shifts from approximately 210 kHz to 190 kHz as the waves propagate from U1 to U3. Note that these frequencies are somewhat lower than the peak frequencies observed at this condition in other tests, likely due to the previously discussed angle of attack errors. The disturbances amplify over this region, increasing in N-factor (integrated amplification rate) by 0.59. The wavepacket appears to intensify as it propagates along the cone surface, correlating with the continued amplification observed in the PCB spectra from U3 to D3 where the N-factor increases by an additional 0.61. The last three images of the sequence show the packet in a transitional state with its periodic structure deteriorating. This behavior aligns with the spectral broadening observed in the spectra for sensors D3 and D5. Note that the 300 kHz peak at station D5 is likely an example of anomalous sensor resonance and not attributable to flow features. While this schlieren sequence is intended to be representative, the transition process is stochastic by nature and the freestream noise environment of impulse facilities like HyperTERP is somewhat more variable than in conventional facilities. This resulted in occasionally significant variation in wavepacket behavior, with some breaking down over the frustum and others traversing the entire cone surface without obviously transitioning. This variation in behavior is a consistent theme throughout this work.

A wavepacket exhibiting transitional behavior at condition Re45 is highlighted in figure 3.2. The wavepacket does not obviously grow in intensity from the first image and begins to lost its structure at around X=405 mm in the fourth and fifth images of the sequence. The PCB spectra indicate saturation occurs between U1 and U3, as the fundamental peak (now at 260 kHz) experiences no growth while frequencies above and below the second mode amplify by nearly an order of mag-

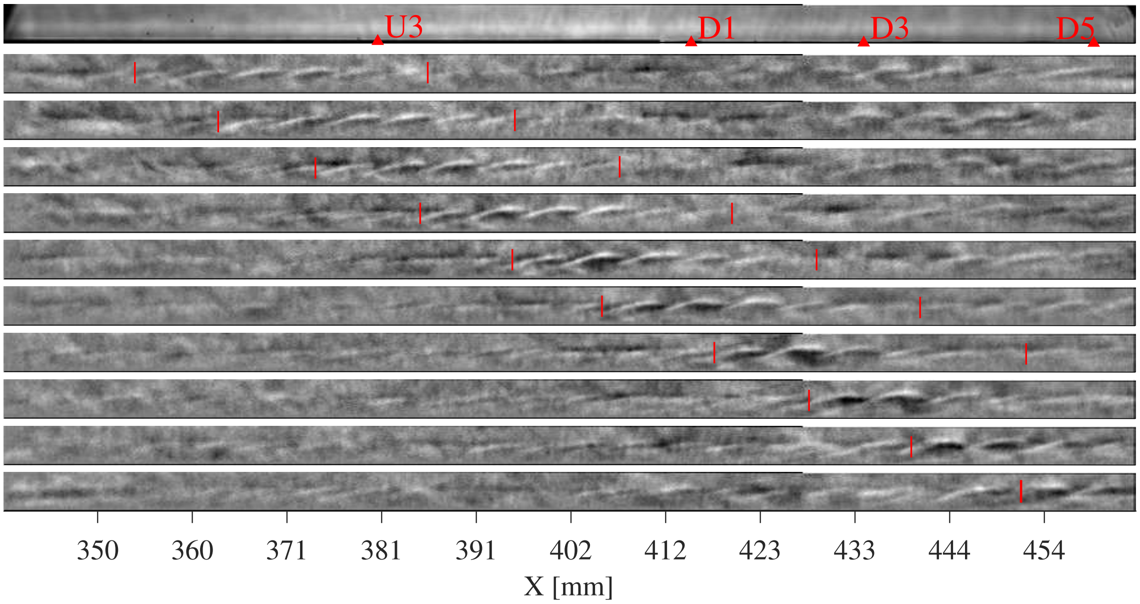

Figure 3.1: Reference-subtracted image sequence captured for the +0° configuration at condition Re33 with inter-image spacing of 9.7 μs.

nitude. This spectral broadening continues along the length of the model, though the second-mode peak is still strongly apparent at D5, indicating that (on average) the boundary-layer is not fully turbulent. The final image of the sequence shows transitional content entering the field of view, once again demonstrating the range of boundary-layer states which occur within individual experiments. There appears to be harmonic second-mode content in the U1 spectrum at 520 kHz which may be linked to the 480 kHz peak at D1 and the 440 kHz peak at D3, though these observations must be treated with skepticism due to sensor resonance.

The upstream movement of the transition front continues at condition Re52, as exemplified by figure 3.3. The highlighted wavepacket in this sequence breaks down as it passes over X=400 mm, resulting in a young turbulent spot over much of the extension. The PCB spectra in figure 3.4 reveal essentially the same trends regarding saturation and spectral broadening as those for condition Re45. Resonance

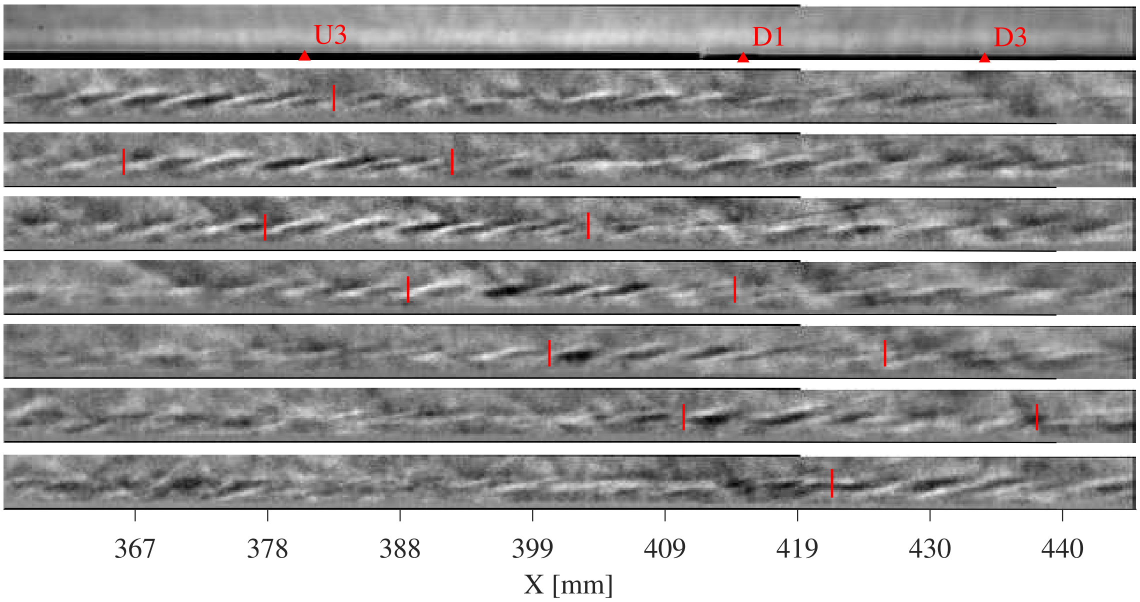

Figure 3.2: Reference-subtracted image sequence captured for the +0° configuration at condition Re45 with inter-image spacing of 9.4 μs.

in sensors D3 and D5 now overlaps with the second-mode peak making it difficult to discern the true amplitude of the disturbances.

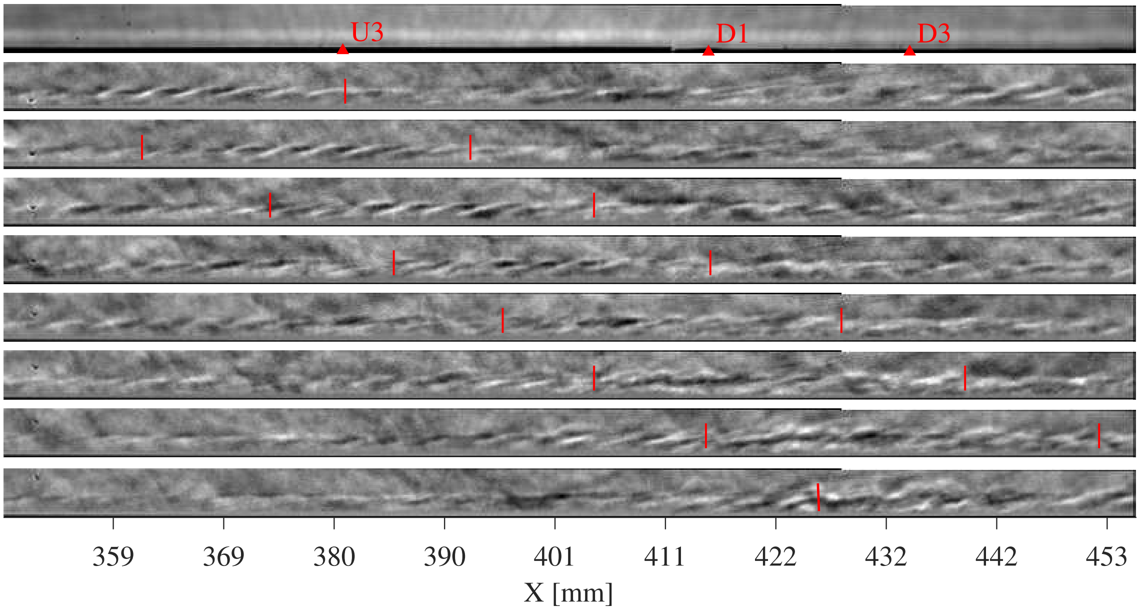

Figure 3.3: Reference-subtracted image sequence captured for the +0° configuration at condition Re52 with inter-image spacing of 10.2 μs.

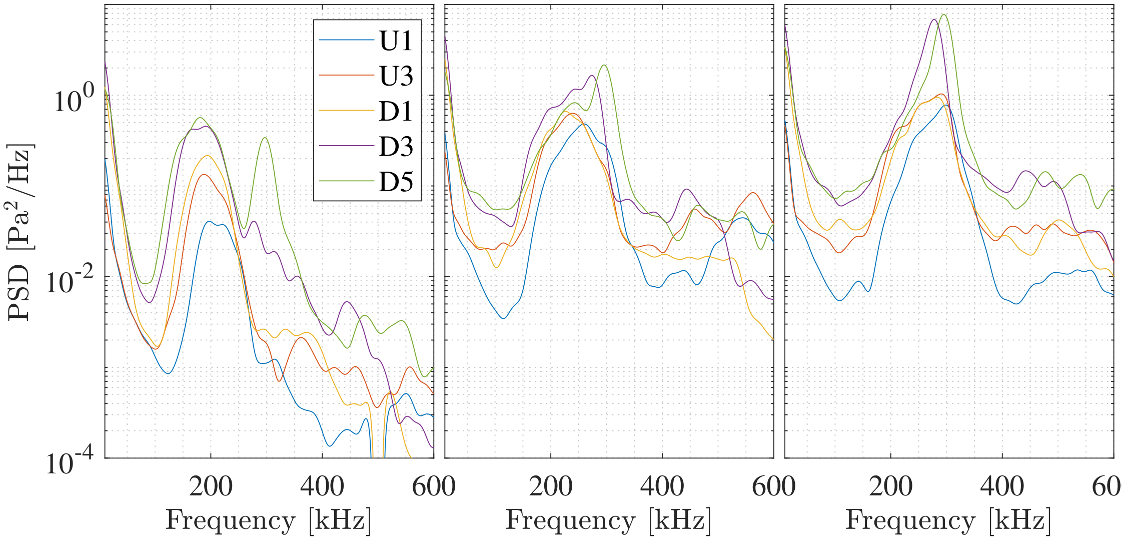

Figure 3.4: Power spectral densities at select PCB stations for the +0° configuration at (left) condition Re33, (middle) condition Re45, and (right) condition Re52.

3.2 -5° Extension

The image sequences of figures 3.5 and 3.6 demonstrate the interaction of second-mode wavepackets with the 5° expansion at conditions Re45 and Re52, respectively; figure 3.5 is also representative of the wavepacket behavior at condition Re33. At conditions Re33 and Re45, the second-mode disturbances are seen to dampen significantly as they propagate through the expansion and along the extension. The wavepacket in figure 3.5 appears to stretch out and gradually vanish as it approaches the edge of the field of view. This is accompanied by a marked decrease in the PCB spectra (see figure 3.7) for frequencies at and above the second-mode fundamental in sensors D3 and D5; the second-mode N-factor drops by 0.55 between U3 and D3. The wavepackets also propagate at a greater off-wall distance downstream of the corner, though this may simply be due to the increased momentum thickness of the boundary layer. At condition Re33, a significant 420 kHz peak persists just downstream of the corner at D1 which may correspond to the first harmonic of the second mode; a similar peak is observed around 480 kHz at condition Re45. For both conditions, D5 demonstrates an increase in spectral energy in lower frequencies. This makes sense, as the increased boundary layer thickness downstream of the corner will tend to promote the amplification of lower-frequency disturbances. A notable phenomenon observed in the image sequence of figure 3.5 is emanation of high-frequency energy along the head of the expansion fan. This behavior, highlighted by red arrows in the third and fourth images of the sequence, is more easily identified when viewing the full videos.

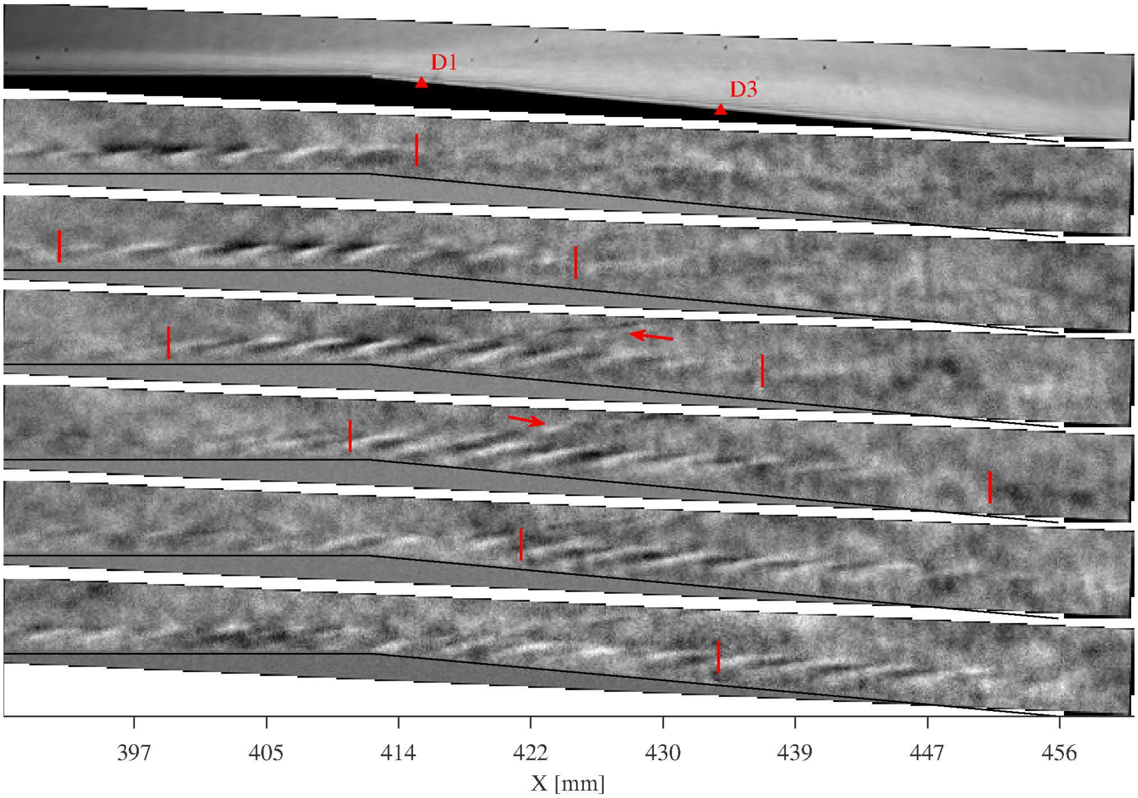

Figure 3.5: Reference-subtracted image sequence for the -5° extension at condition Re45 with inter-image spacing of 10.9 μs.

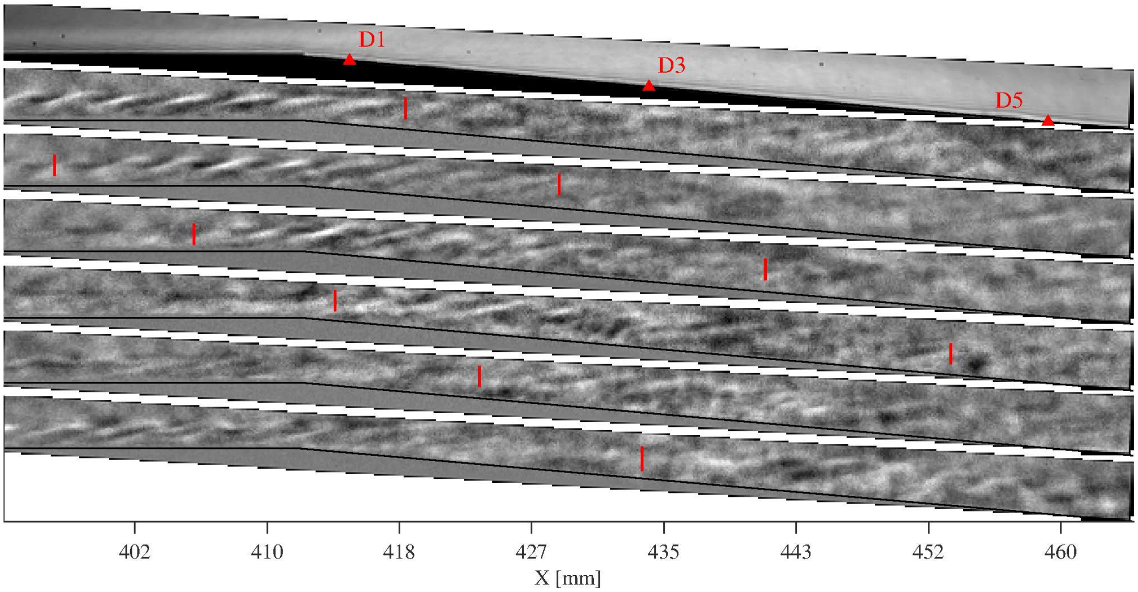

Figure 3.6: Reference-subtracted image sequence for the -5° extension at condition Re52 with inter-image spacing of 10.7 μs.

Transitional behavior prior to the corner becomes commonplace at condition Re52, with one such occurence illustrated in figure 3.6; in this case the incoming wavepacket seemingly breaks down as it passes over the corner. The expansion still has a damping effect on the turbulent content, however, with the structures becoming largely indistinct downstream. Though there is an obvious reduction in second-mode power in the PCB spectra at stations D3 and D5, sensor resonance makes it difficult to quantify the decay due to overlap with the fundamental frequency of the disturbances. These sensors also demonstrate greater persistance of high frequencies (> 400 kHz) at the model surface than at lower Re_m.

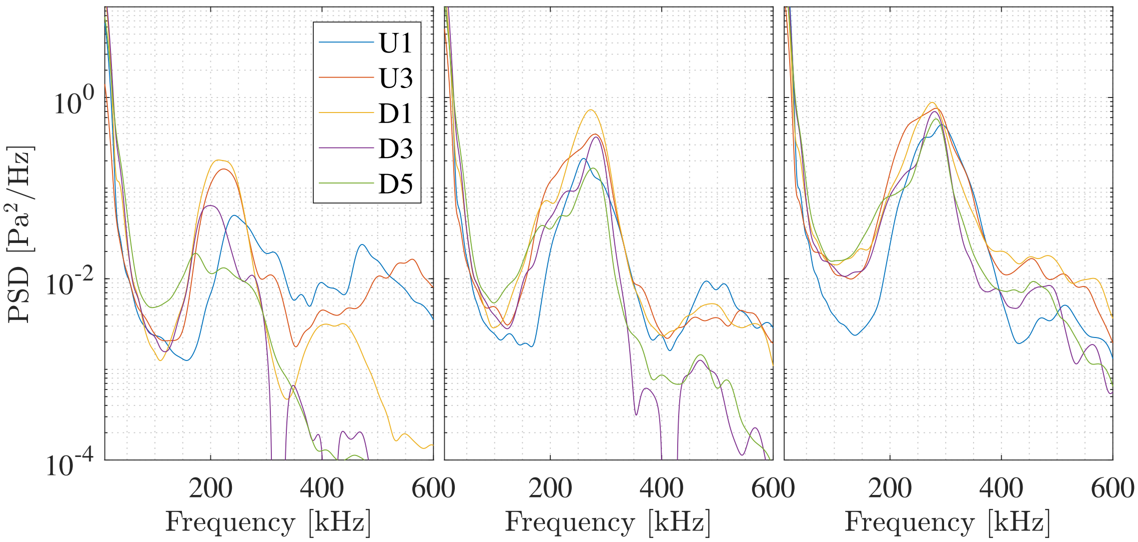

Figure 3.7: Power spectral densities at select PCB stations for the -5° configuration at (left) condition Re33, (middle) condition Re45, and (right) condition Re52.

3.3 +5° Extension

Contrasting starkly with the expansion case, the compression-flare configurations and the resulting corner SWBLIs serve largely to promote disturbance growth and transition. Figure 3.8 presents an image sequence captured at condition Re33 with the +5° configuration, again focusing on an incoming second-mode wavepacket. The field of view for this test is focused primarily on the flare to better capture the downstream development of the boundary-layer disturbances. When the wavepacket encounters the SWBLI, energy is radiated away along the shock (indicated by the red arrow in the fifth and sixth images of the sequence). This radiation is apparent for nearly all wavepackets, has a periodicity similar to the second-mode, and typically appears to emanate from the tail of a wavepacket. A similar phenomenon appeared in computations performed by Sawaya et al. [41] of second-mode waves interacting with two-dimensional wall deformations. Downstream of the corner the wavepackets retain their “rope-like” appearance, but the structure angle of the disturbances decreases such that they appear flatter relative to the model surface. This continued growth is confirmed by the PCB spectra of figure 3.11, as the wavepackets do not appear to saturate until downstream of D3. The tail of the wavepacket then appears to transition around X=450 mm as the head of the packet leaves the field of view, seemingly without breaking down. Note that the first three images of figure 3.8 depict the tail of a wavepacket exiting the field of view intact, providing a counter-example to this transitional behavior. The PCB spectra along the flare, particularly D5, demonstrate a notable shift in the second-mode peak to higher frequencies brought about by the reduced boundary-layer thickness. The compression may also promote the development of harmonic content, as the D3 and D5 spectra display strong peaks at 435 kHz and 470 kHz, respectively. The spectra also display substantial low-frequency growth downstream of the corner.

The PCB spectra in the middle plot of figure 3.11, corresponding to condition Re45, show reduced growth in the second-mode peak along the frustum relative to condition Re33. In other respects, the behavior observed at condition Re45 mimics that at lower Re_m, including the apparent saturation and decay of wavepackets in the vicinity of D3. Importantly, the broadband amplification observed between sensors D1 and D3 exceeds that of the $+0°$ configuration, implying acceleration of the transition process relative to the undisturbed boundary-layer. The sequence in figure 3.9 again demonstrates the tendency for the radiation to propagate from the wavepacket tail and for this to be the portion of the disturbance which first

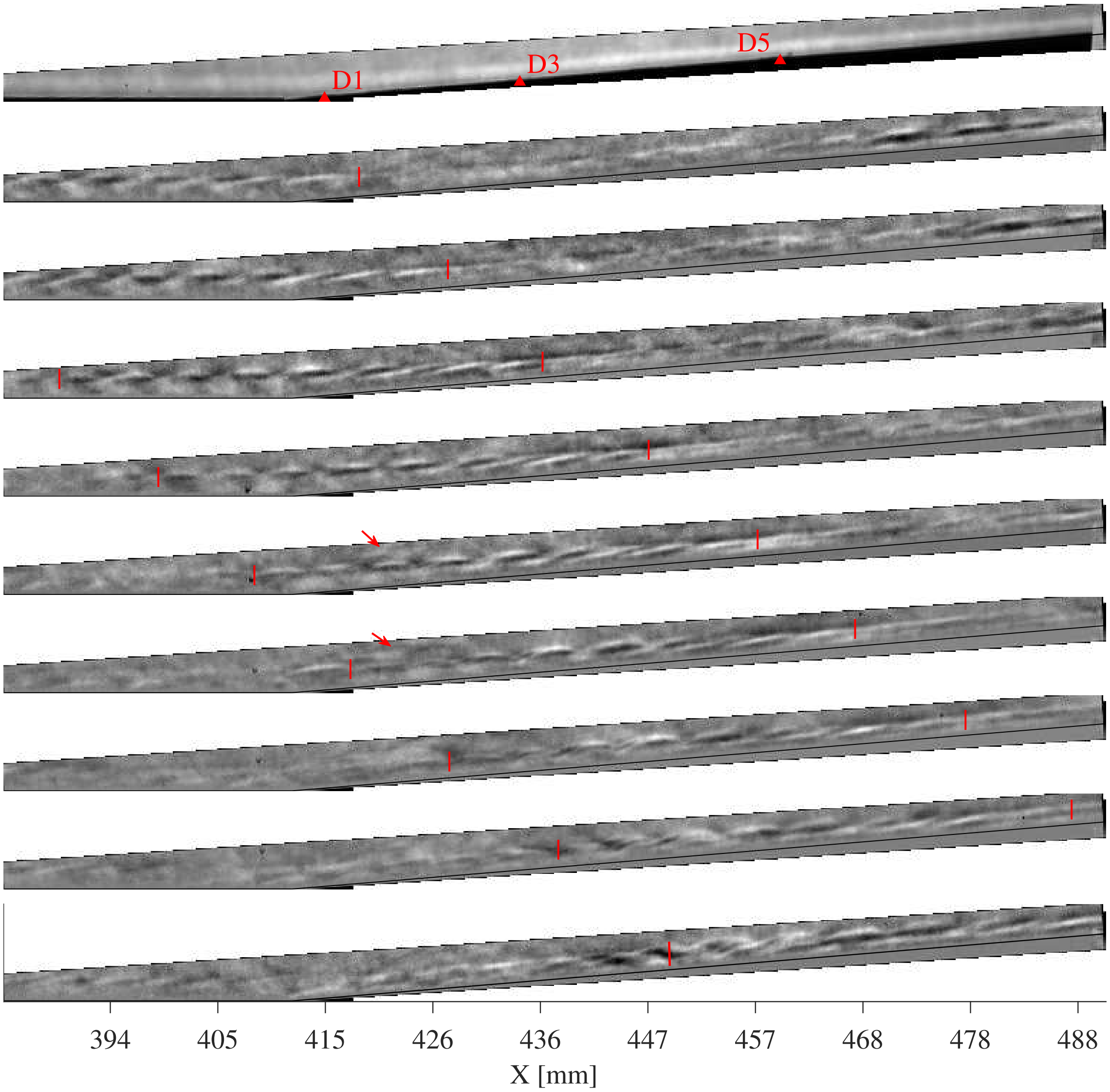

Figure 3.8: Reference-subtracted image sequence captured for the +5° configuration at condition Re33 with inter-image spacing of 8.8 μs.

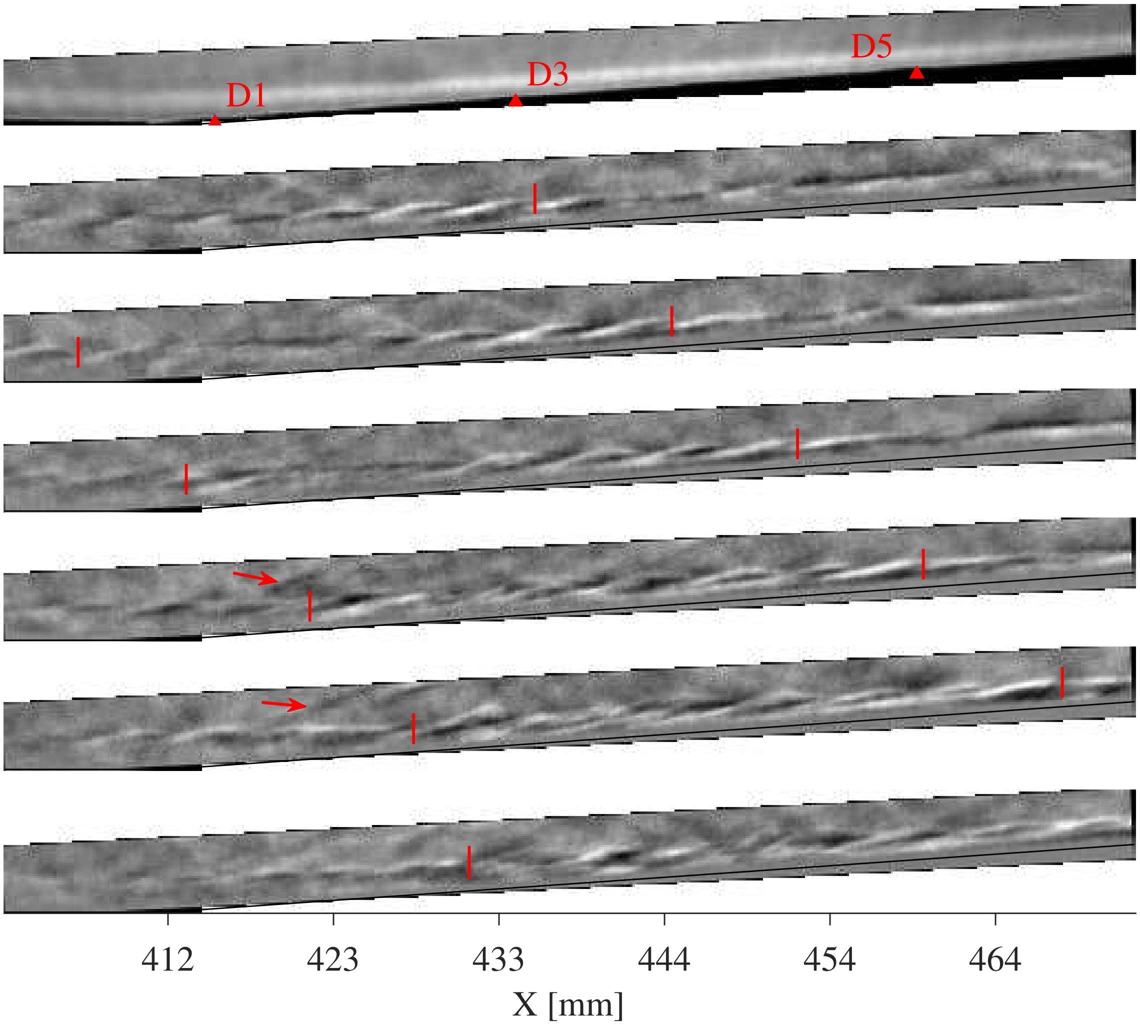

Figure 3.9: Reference-subtracted image sequence captured for the +5° configuration at condition Re45 with inter-image spacing of 7.3 μs.

transitions.

At condition Re52, the PCB spectra along the flare (D1, D3 and D5) in the rightmost plot of figure 3.11 show significant amplification in frequencies above and below the second-mode peak relative to the undisturbed spectra obtained with the +0° configuration. It is unclear to what extent the spike in second-mode power at D3 and D5 is due to sensor resonance, but it is clear the signal becomes largely broadband along the flare, indicative of the onset of a turbulent boundary layer.

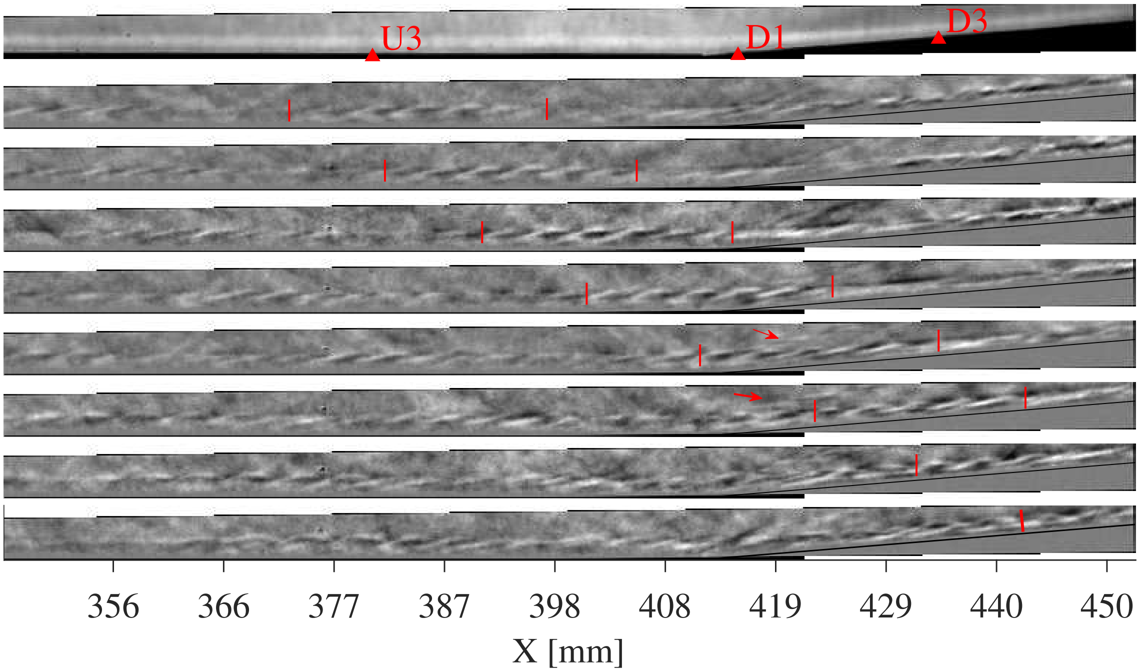

Figure 3.10: Reference-subtracted image sequence captured for the +5° configuration at condition Re52 with inter-image spacing of 8.8 μs.

Indeed, the full test video shows this is typically the case, with many packets already transitioning upstream of the flare. The selected image sequence in figure 3.10 shows a packet which retains some periodicity through the compression, though the tail of the packet transitions immediately upon reaching the flare. Red arrows in the fifth and sixth images highlight radiation away from the packet even as it enters a transitional state. When contrasted with the undisturbed case, the results for this configuration suggest that the non-separated SWBLI here accelerates boundary-layer transition for sufficiently high Re_m.

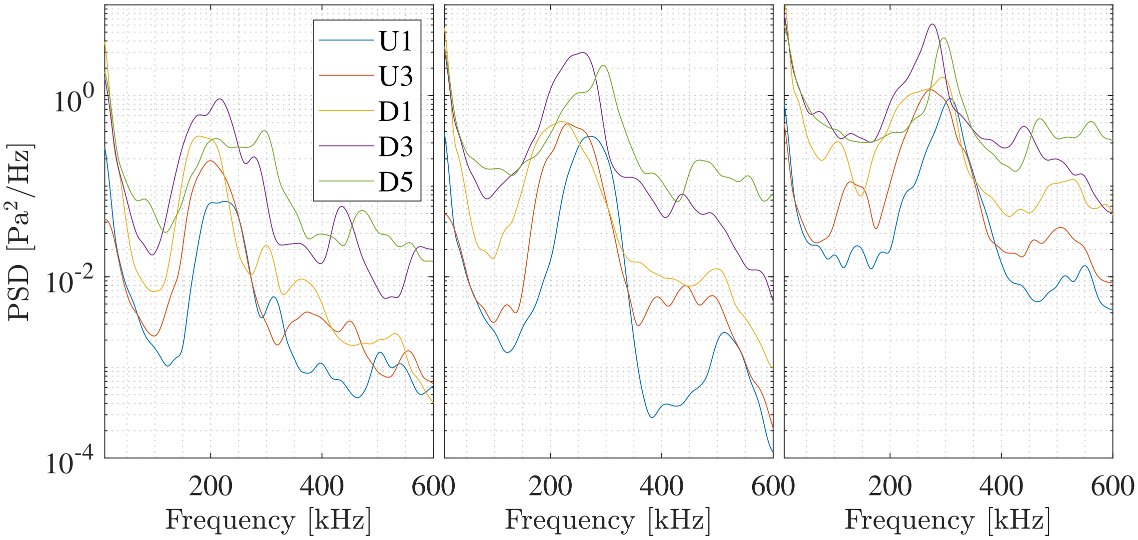

Figure 3.11: Power spectral densities for select PCB stations at the +5° configuration at (left) condition Re33, (middle) condition Re45, and (right) condition Re52.

3.4 +10° Extension

The visualization sequences presented in figures 3.12, 3.13, and 3.14 show the development of second-mode wavepackets at each condition for the +10° configuration. The adverse pressure gradient imposed by this compression is sufficient to separate the boundary layer upstream of the flare. Approximate separation and reattachment locations are represented in each image sequence by vertical, dashed lines and are given in table 3.1. These locations were identified as points at which the pseudo-streamline profiles reported in section 4.1 exhibited a sudden change in slope; reasonable agreement was obtained between these results and preliminary numerical simulations presented in chapter 7. The uncertainty in each location is estimated as ±3 mm.

The images in figure 3.12 depict a single wavepacket traversing the resulting

	Re33	Re45	Re52
$X_{separation}$ [mm]	391	396	403
$X_{reattachment}$ [mm]	432	428	424

Table 3.1: Approximate separation and reattachment locations for the +10° configuration.

separation region at condition Re33. In the mean image, the boundary layer separates roughly halfway between sensor U3 and the corner junction, and reattaches slightly upstream of D3. In the PCB spectra for this condition (figure 3.15), substantial growth in the fundamental second-mode range ($175 - 275\,\text{kHz}$) is observed between U1 and U3, with the disturbance peak increasing in N-factor by 0.70 (similar to the other cases) and decreasing in frequency from 247 kHz to 220 kHz. These sensors also reveal a potential harmonic developing at 440 kHz. At the separation point, the instability waves lift off the cone surface and propagate largely within the separated shear layer. This behavior is reflected in the PSD for sensor D1, which shows a marked decrease in second-mode power; note, however, the increase in low-frequency content peaking at 73 kHz. We will later demonstrate that this low-frequency peak corresponds to new, shear-generated disturbances. The waves appear to stretch and flatten out as they propagate downstream, but retain their periodic structure through reattachment, with sensor D3 displaying a recovery in second-mode power. The reduced boundary-layer thickness along the flare results in the amplification of higher-frequency disturbances, as evidenced by sensor D5.

Figure 3.13 depicts the typical transitional behavior of wavepackets which encounter the separated region at condition Re45. The incoming wavepacket can be seen to morph substantially downstream of separation, with some features propa-

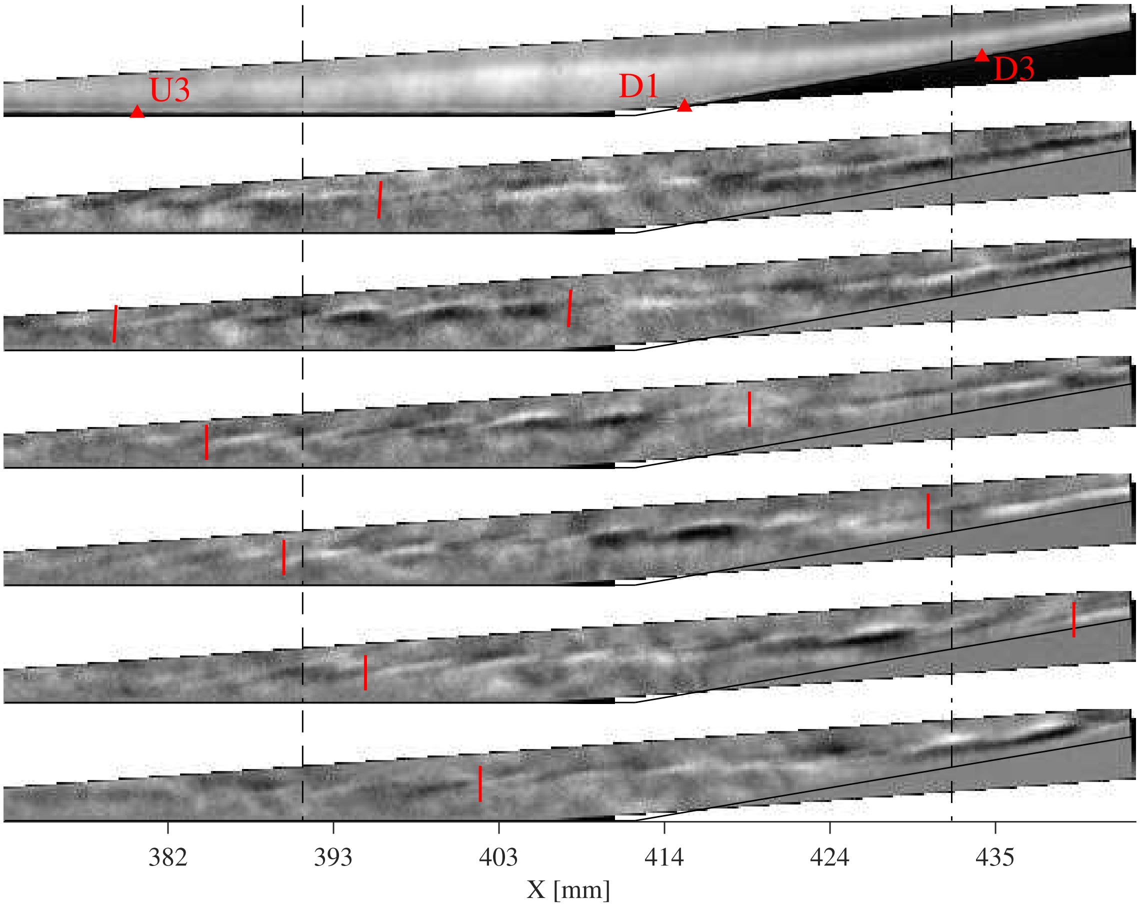

Figure 3.12: Reference-subtracted image sequence captured for the +10° flare at condition Re33 with inter-image spacing of 9.7 μs.

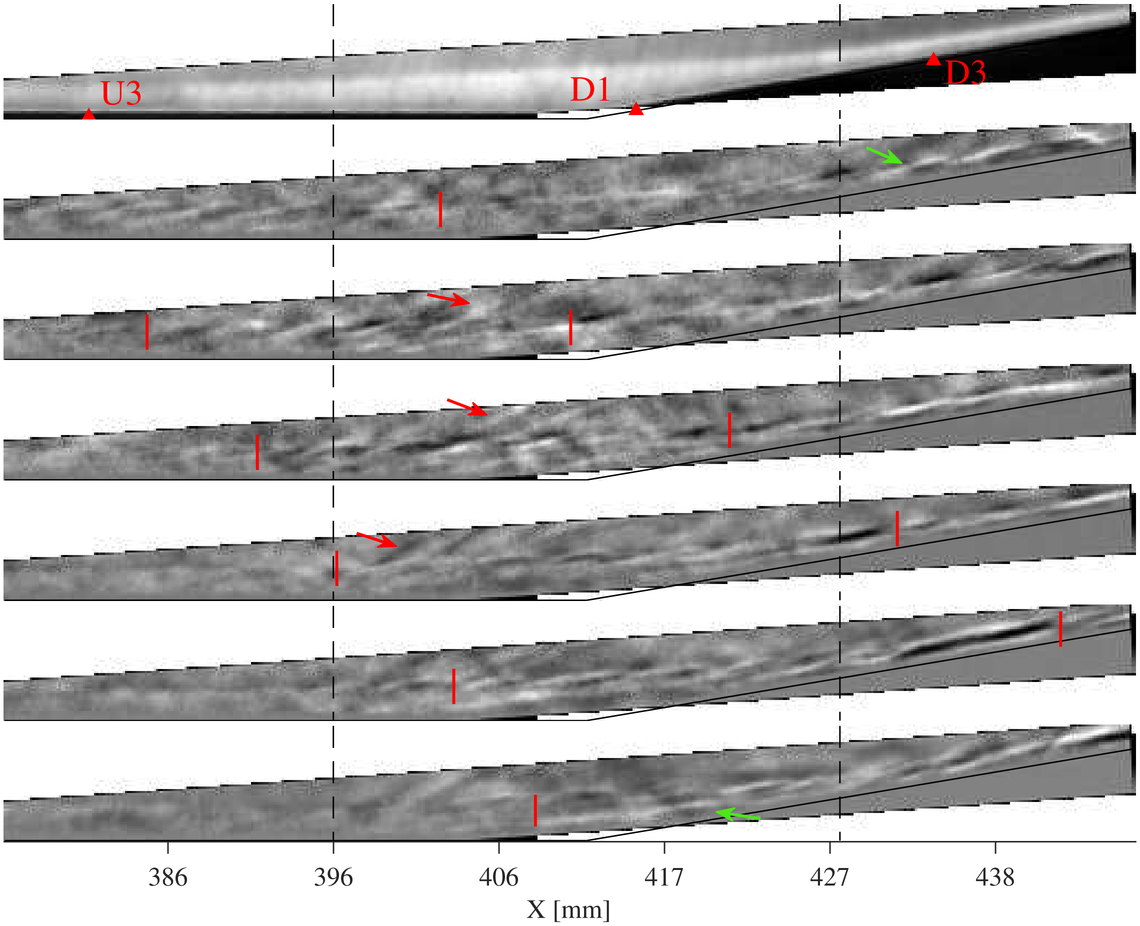

Figure 3.13: Reference-subtracted image sequence captured for the +10° flare at condition Re45 with inter-image spacing of 9.7 μs.

gating near the wall within the recirculation zone. These images show the apparent radiation of disturbance energy along the separation shock, highlighted by red arrows in the second, third and fourth images of the sequence, matching observations seen with the +5° configuration. As at condition Re33, there is evidence of a harmonic developing in the U3 spectra at 500 kHz while sensor D1 reveals substantial growth of low-frequencies within the separated region, now peaking at 85 kHz. Upon reattachment the packet's structure has distorted to include a larger range of scales and lost its "rope-like" appearance, explaining the broadband spectra of sensors D3 and D5. However, such behavior is not fully representative of condition Re45; the state of the incoming wavepacket may substantially alter its development through the SWBLI. In the first image of the sequence in figure 3.13, for example, a wavepacket is visible downstream of D3 that has largely retained its structure.

For condition Re52, the separation region has shrunk significantly and the second-mode wave packets are, on average, close to saturation when incident upon it. Figure 3.14 depicts a wavepacket approaching the SWBLI with persistent turbulence enveloping the flare. Such behavior mimicks that observed with the +5° configuration and is reflected in the PCB spectra, where even sensor D1 displays primarily broadband content. Radiation events still occur at this condition and are indicated by red arrows in the fourth and fifth reference-subtracted images.

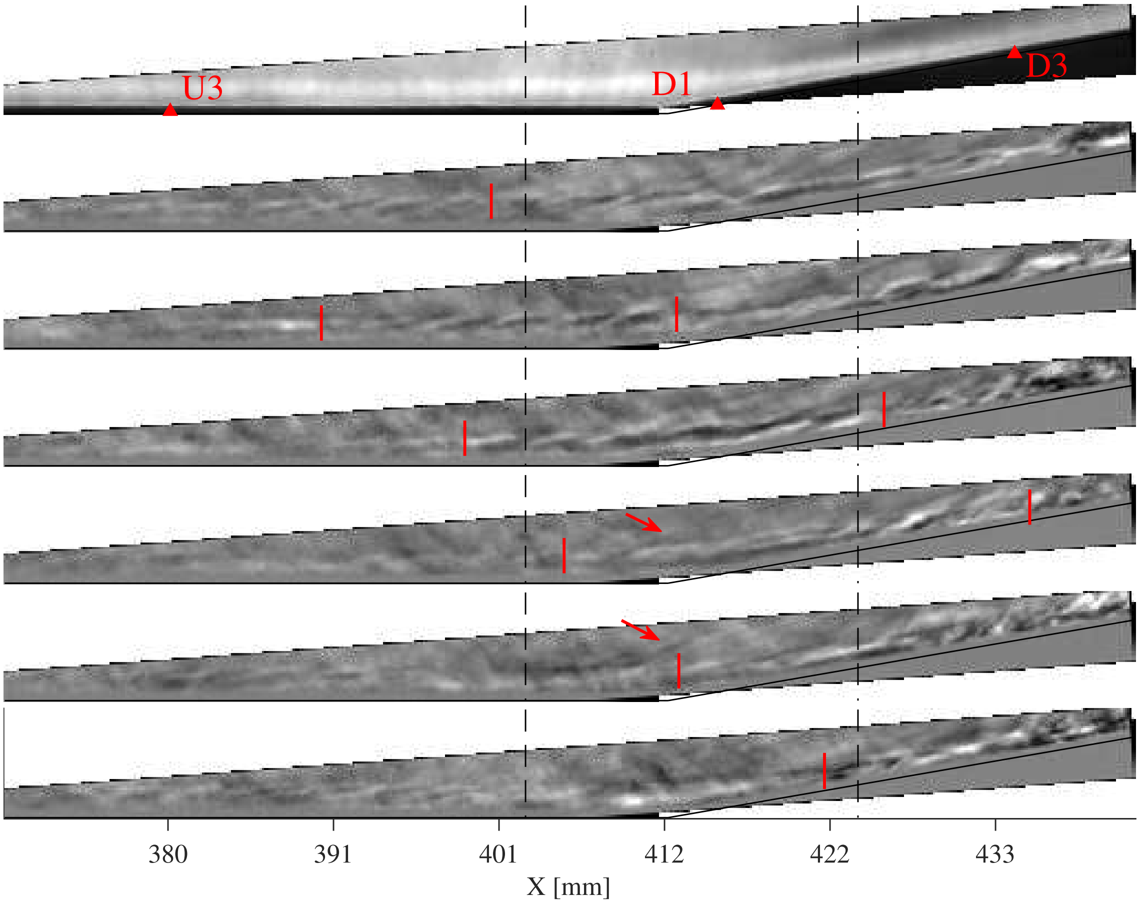

Figure 3.14: Reference-subtracted image sequence captured for the +10° flare at condition Re52 with inter-image spacing of 9.7 μs.

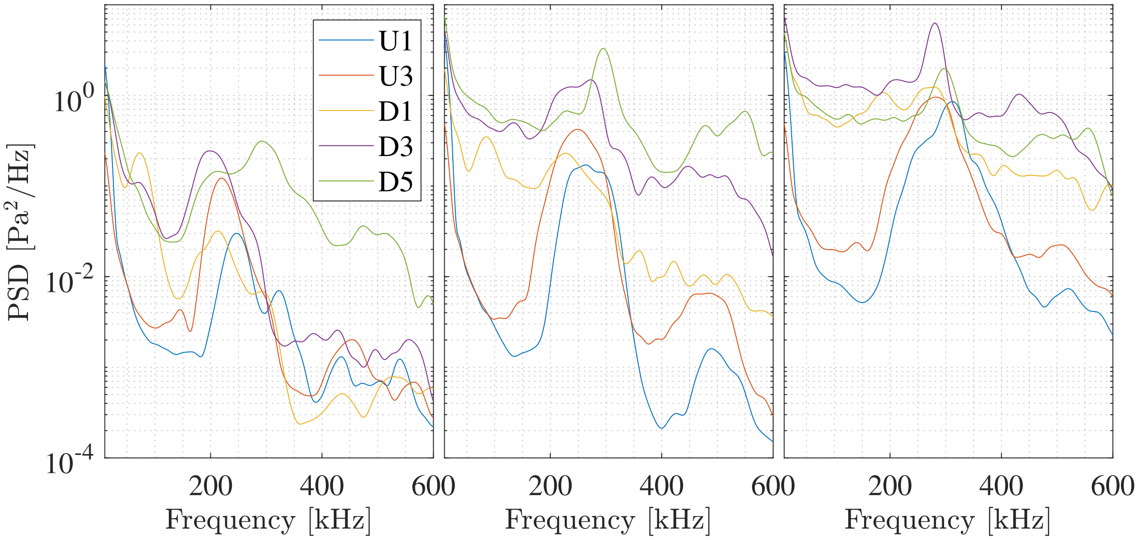

Figure 3.15: Representative power spectral densities at select PCB stations for the +10° configuration at (left) condition Re33, (middle) condition Re45, and (right) condition Re52.

	Re33	Re45	Re52
$X_{separation}$ [mm]	N/A	N/A	394
$X_{reattachment}$ [mm]	440	433	427

Table 3.2: Approximate separation and reattachment locations for the +15° configuration.

3.5 +15° Extension

As evident from the mean flow-on image in figure 3.16, the +15° compression flare produces a separation bubble which (at condition Re33) extends far enough upstream to fully envelop sensor U3. Approximate separation and reattachment locations for this configuration are given in table 3.2. These were determined in the same manner as before, though the separation location could not be determined at conditions Re33 and Re45 as the boundary layer appeared to separate upstream of the field of view in both cases.

Second-mode wavepackets appear only intermittently within the field of view with this configuration (at Re33 and Re45) and the dominant boundary-layer feature instead appears to be a shear-generated instability which forms over the separation bubble. This instability takes the form of long, braided structures aligned with the direction of propagation which may be seen in the instantaneous image sequence of figure 3.16. The disturbances undergo substantial amplification once the shear layer begins to recompress from X=412 mm. As the waves encounter the flare near reattachment, they emanate energy into the shock-layer as annotated by red arrows in the third and fourth images of the sequence. This energy has a wavy, ribbon-like structure. Around reattachment, the features take on a thin, layered structure but the streamwise extent of the field of view is insufficient to fully characterize their downstream behavior. Excessive broadband sensor resonance contaminated the PCB data for most experimental runs with this configuration and thus no spectra are presented. It is also worth noting that the method used for determining the separation and reattachment locations is particularly fraught at these conditions due to the lack of second-mode wavepackets to define the pseudo-streamline.

Though rare at this condition, the propagation of one second-mode wavepacket at condition Re33 is presented in figure 3.17. As the wavepacket traverses the separation bubble, it loses its distinctive structure and appears to merge with the shear-waves. That said, the boundary layer over the flare in the final image of the sequence appears perturbed by the arrival of the remnants of this disturbance relative to its uniform, layered structure in the first three images of the sequence.

At condition Re45 the boundary layer is once again dominated by the shear-generated disturbances. The image sequence of figure 3.18 shows the structure of the disturbances is almost identical to that observed at condition Re33, but the emanation of disturbance energy is more distinct (see the first three images of the sequence). The reduced separation bubble size relative to condition Re33 allows us to observe the behavior of these disturbances further downstream of reattachment (in the final three images) where they retain a thin, periodic structure. The final image of figure 3.18 shows a second ribbon of energy detaching from the separated shear layer as another shear disturbance approaches the flare.

Although second-mode wavepackets remain rare at this condition, those that do appear retain their structure through the separation bubble to a greater extent

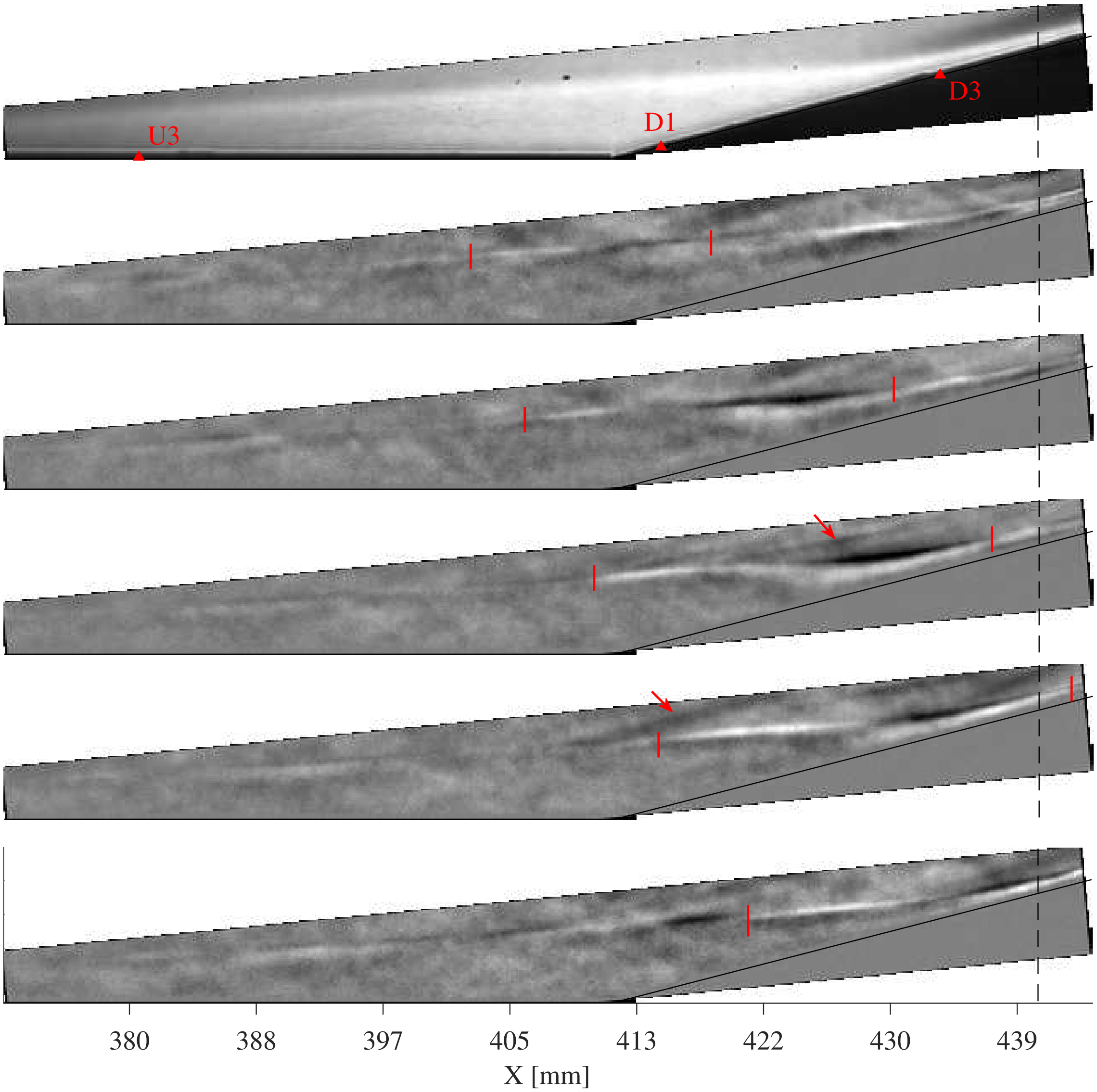

Figure 3.16: Reference-subtracted image sequence captured for the +15° configuration at condition Re33. Successive images are spaced by 6.8 μs.

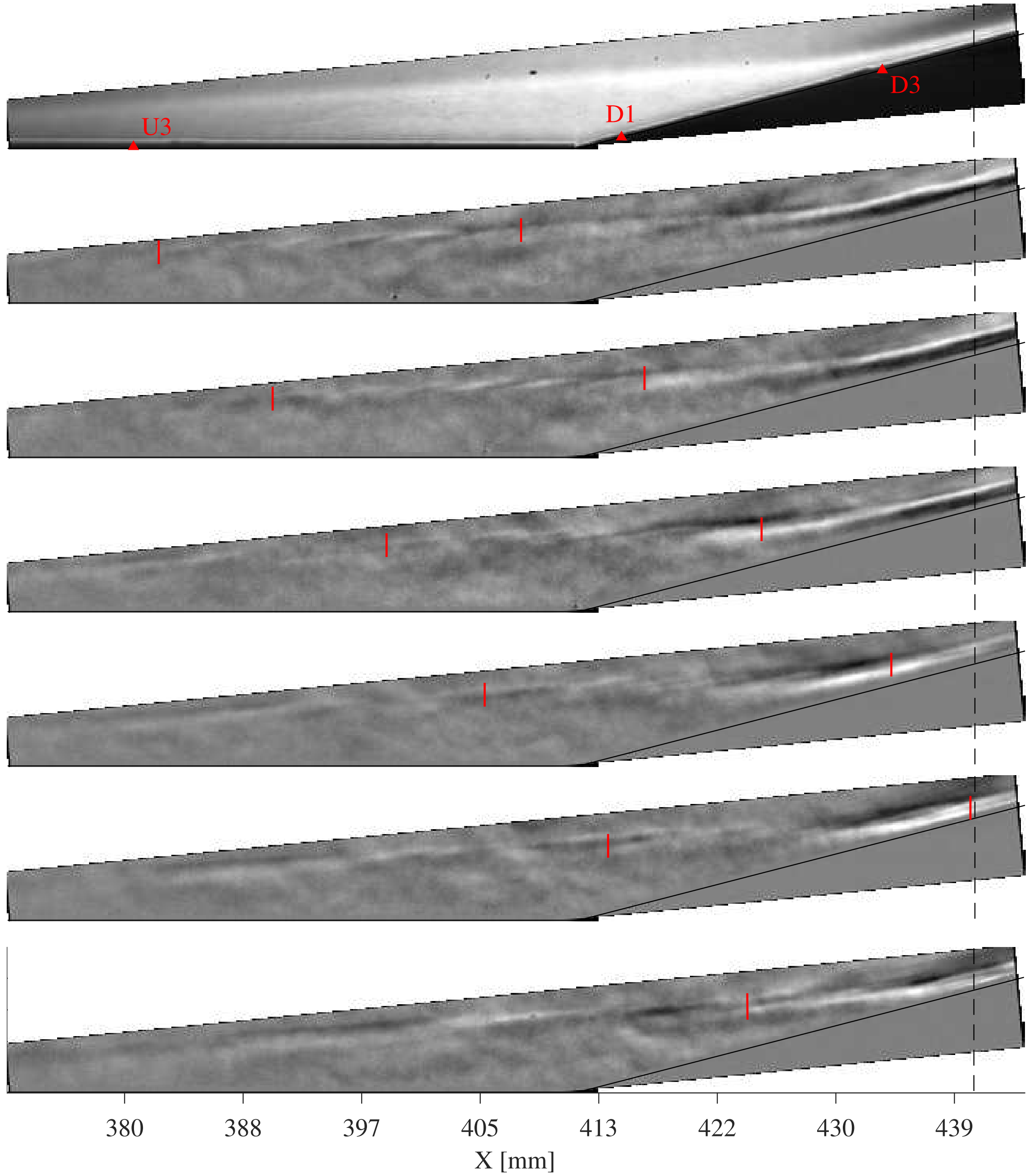

Figure 3.17: Reference-subtracted image sequence captured for the +15° configuration at condition Re33 showing second-mode behavior. Successive images are spaced by 9.1 μs.

than at condition Re33. This is exemplified by figure 3.19 where the incoming wavepacket is seen to flatten out significantly over the separated region but imposes a periodic, wavy structure on the separated shear layer near reattachment at around X=430 mm in the final image of the sequence.

At condition Re52, second-mode waves re-emerge as the primary disturbance with shear waves appearing only intermittently. Several particularly intense bursts of turbulence were observed in this experiment which caused the separation bubble to collapse and reform in a transient process. The image sequence of figure 3.20 shows a wavepacket passing through the SWBLI during one such recovery event. The behavior of the packet in many ways mimics that observed with the +10° configuration. The third image of the sequence shows radiation emanating from the head of the wavepacket as it reaches the flare (annotated with a green arrow). The wavepacket immediately enters a transitional state along the flare, as evidenced by the turbulent structures seen around X=427 mm in the final image. This behavior is not, however, universal: the first image of the sequence shows a wavepacket on the flare (again indicated by a green arrow) which does not appear obviously transitional. The full video shows that the boundary layer over the flare is often fully turbulent.

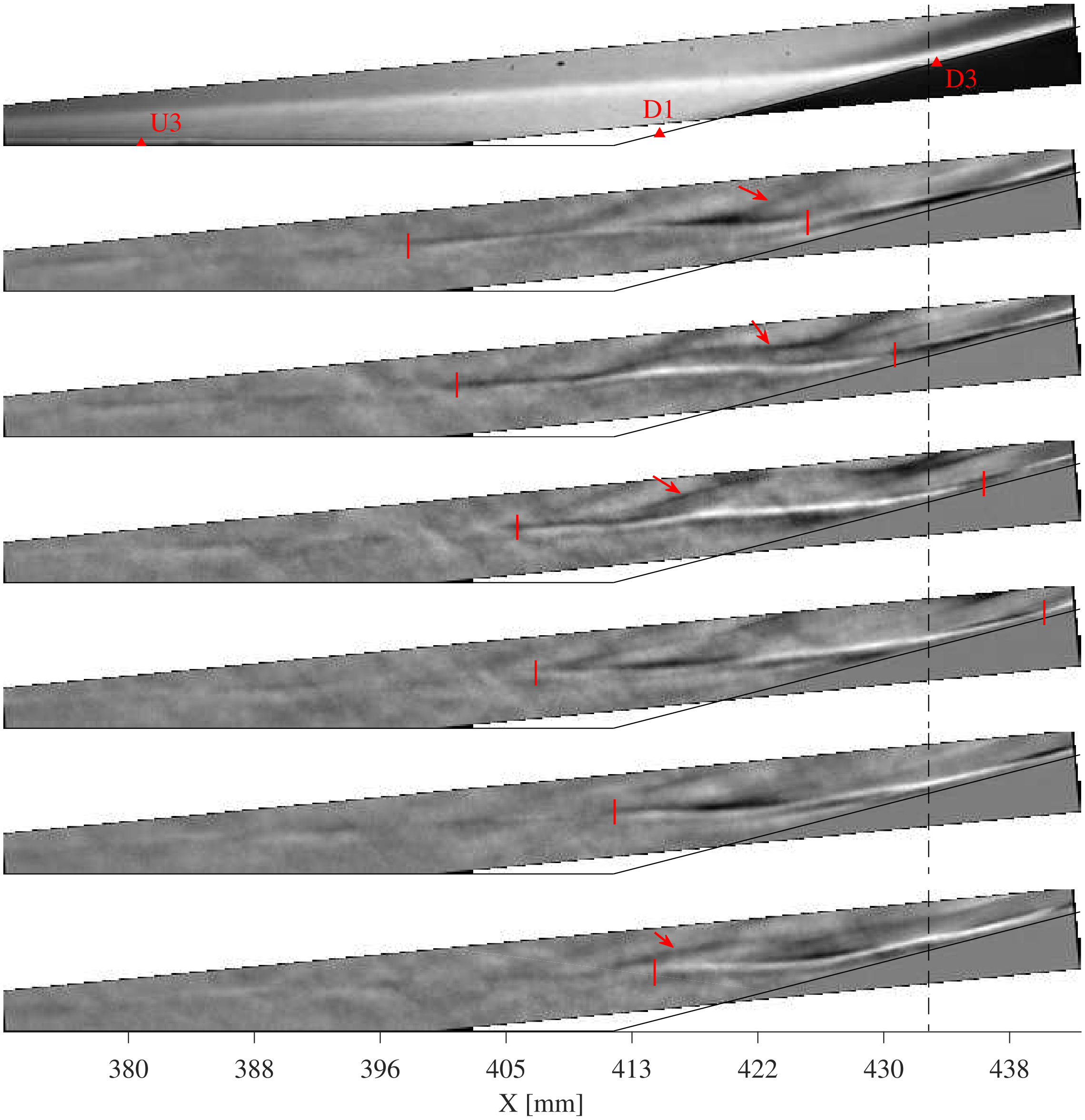

Figure 3.18: Reference-subtracted image sequence captured for the +15° configuration at condition Re45. Successive images are spaced by 5.5 μs.

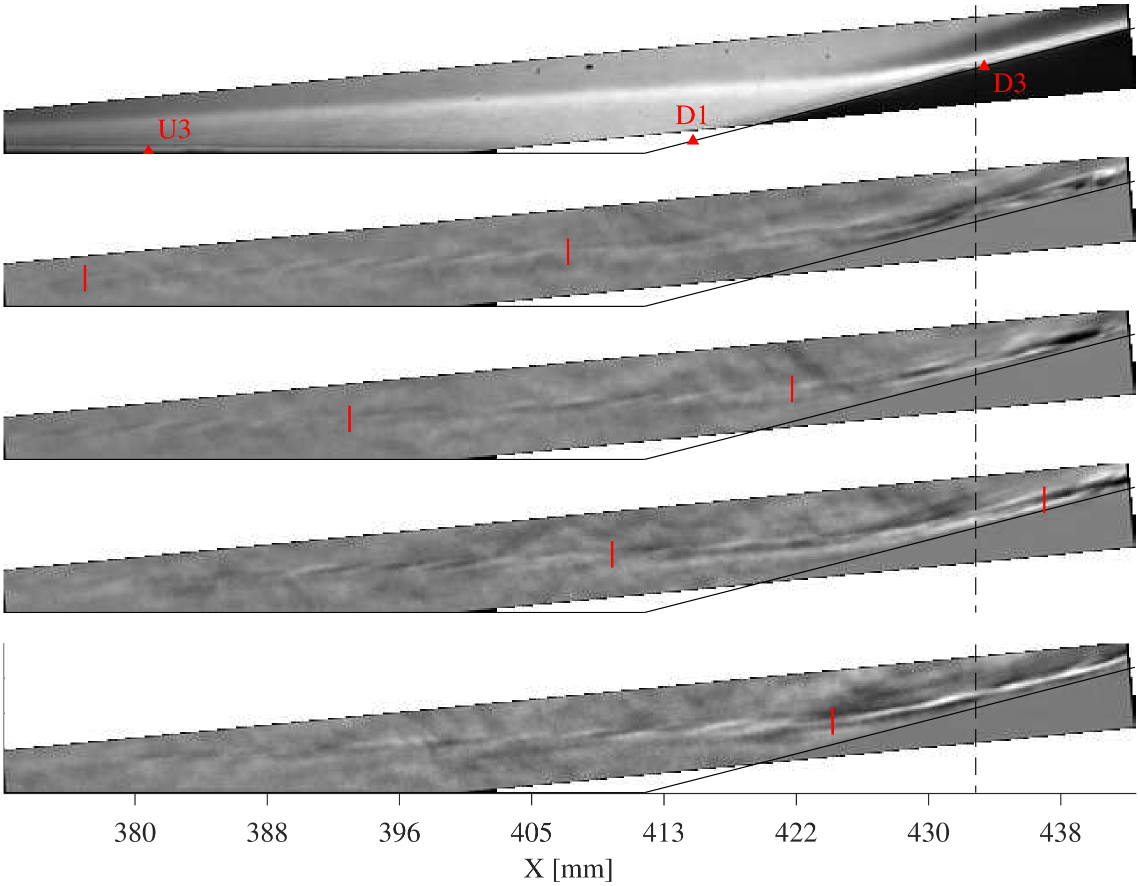

Figure 3.19: Reference-subtracted image sequence captured for the +15° configuration at condition Re45 showing second-mode behavior. Successive images are spaced by 9.1 μs.

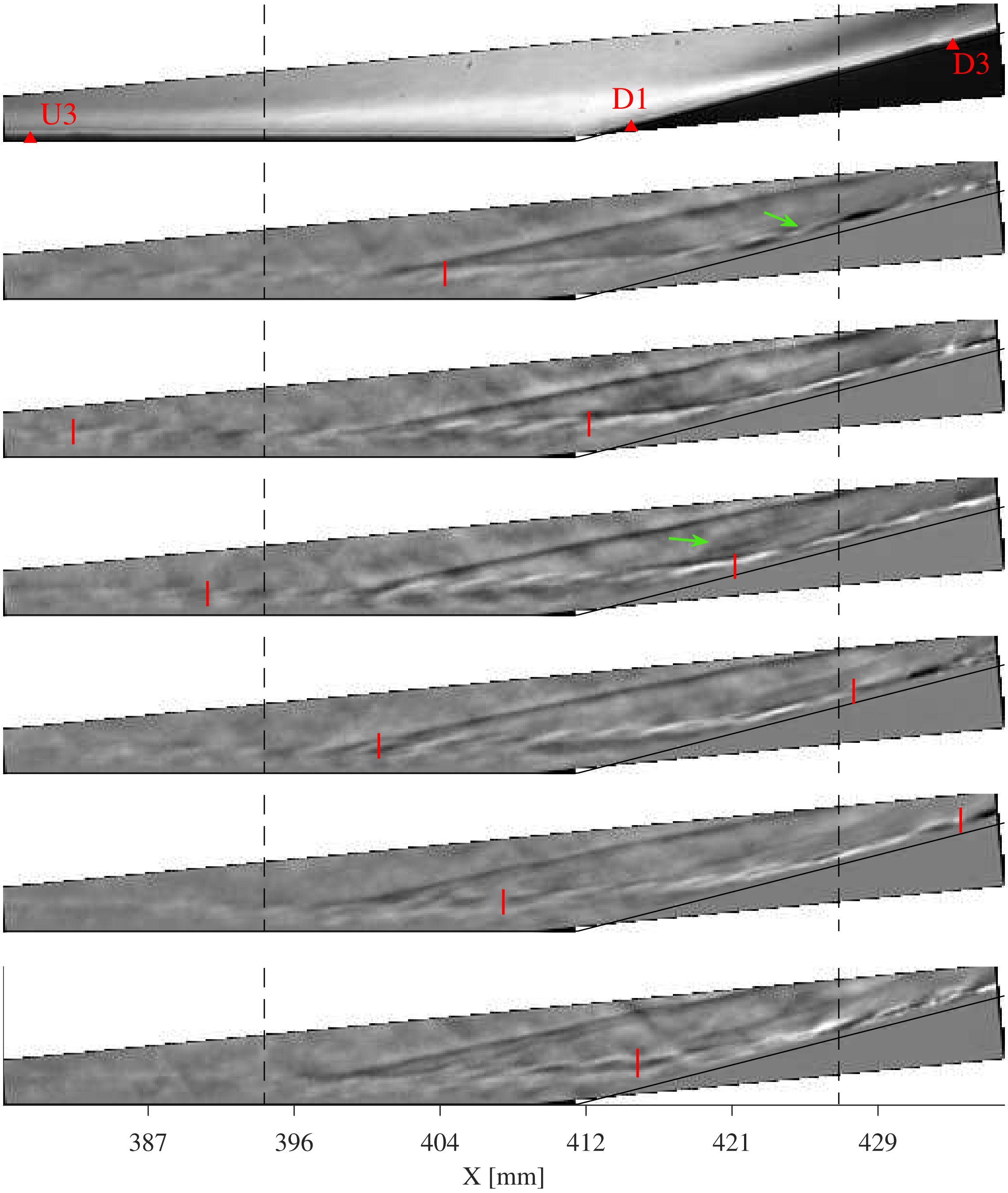

Figure 3.20: Reference-subtracted image sequence captured for the +15° configuration at condition Re52. Successive images are spaced by 8.2 μs.

Chapter 4: Low-order Spectral Analysis

4.1 Second-mode Behavior

The ultra-high frame rate employed throughout this work allows us to perform spectral analysis on the schlieren data without assuming a propagation speed for the disturbances (as in Kennedy et al. [17]). To this end, PSD curves were computed for each pixel in the field of view for each test over the steady test duration using Welch's method with Hann windows of length 64. This process then allows us to visualize the spatial distribution of frequency content anywhere within the field of view. The number of frames included in these calculation varied from 2400-5000 depending on the framerate of the test. The one exception to this is the condition Re45 test of the +15° configuration. The latter half of this test was contaminated by anomalous turbulence and thus only 1300 images were kept. The exact number of frames used for each test was the same as that used for the SPOD analysis, as reported in table 5.1.

In figure 4.1 we present spatial distributions of the integrated disturbance power for each configuration at condition Re33 over the frequency band $170-270$ kHz (corresponding the dominant second-mode frequencies determined from the PCB measurements). Note that the data for the +15° case was obtained at only 440 kHz,

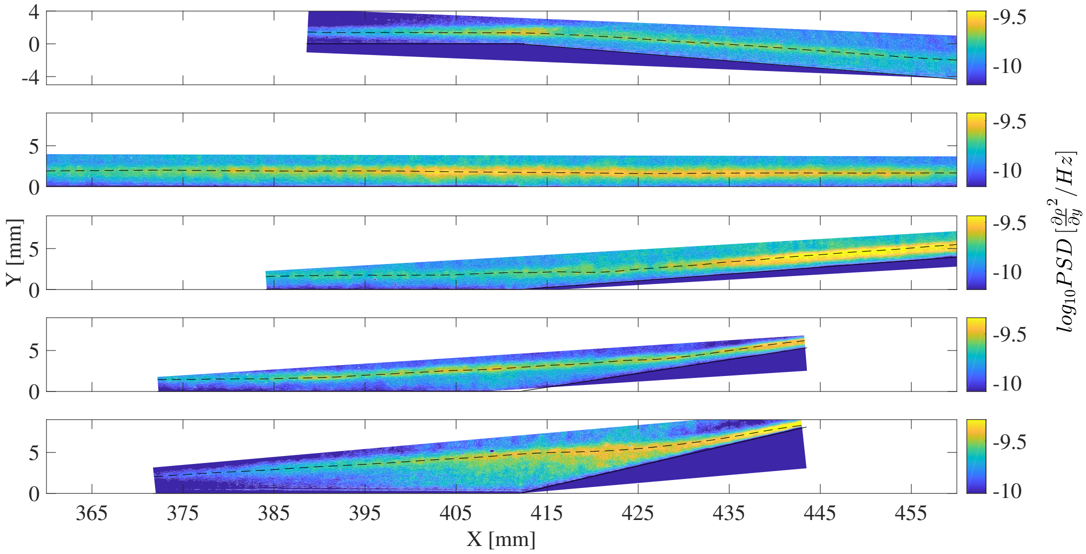

Figure 4.1: Spatial contours for each flare configuration of average PSD from 170 − 270 kHz at condition Re33.

meaning that frequency content between 220 − 270 kHz would be aliased down to 170 − 220 kHz. The dashed line in each image traces the location of maximum PSD strength within this second-mode frequency range and can be interpreted as a pseudo-streamline along which the disturbances tend to propagate. The full-range spectra corresponding to each pixel along these pseudo-streamlines are presented in figure 4.2.

The second contour in figure 4.1 illustrates the behavior of the undisturbed second-mode content, which gradually diminishes downstream of X=435 mm, likely due to saturation. The streamline spectra support this interpretation, as spectral broadening is observed even upstream of the corner. This behavior contrasts sharply with the -5° configuration (top contour), in which the second-mode power rapidly decays downstream of the expansion corner; this matches the qualitative behavior observed in the schlieren image sequences. This decay is experienced across all

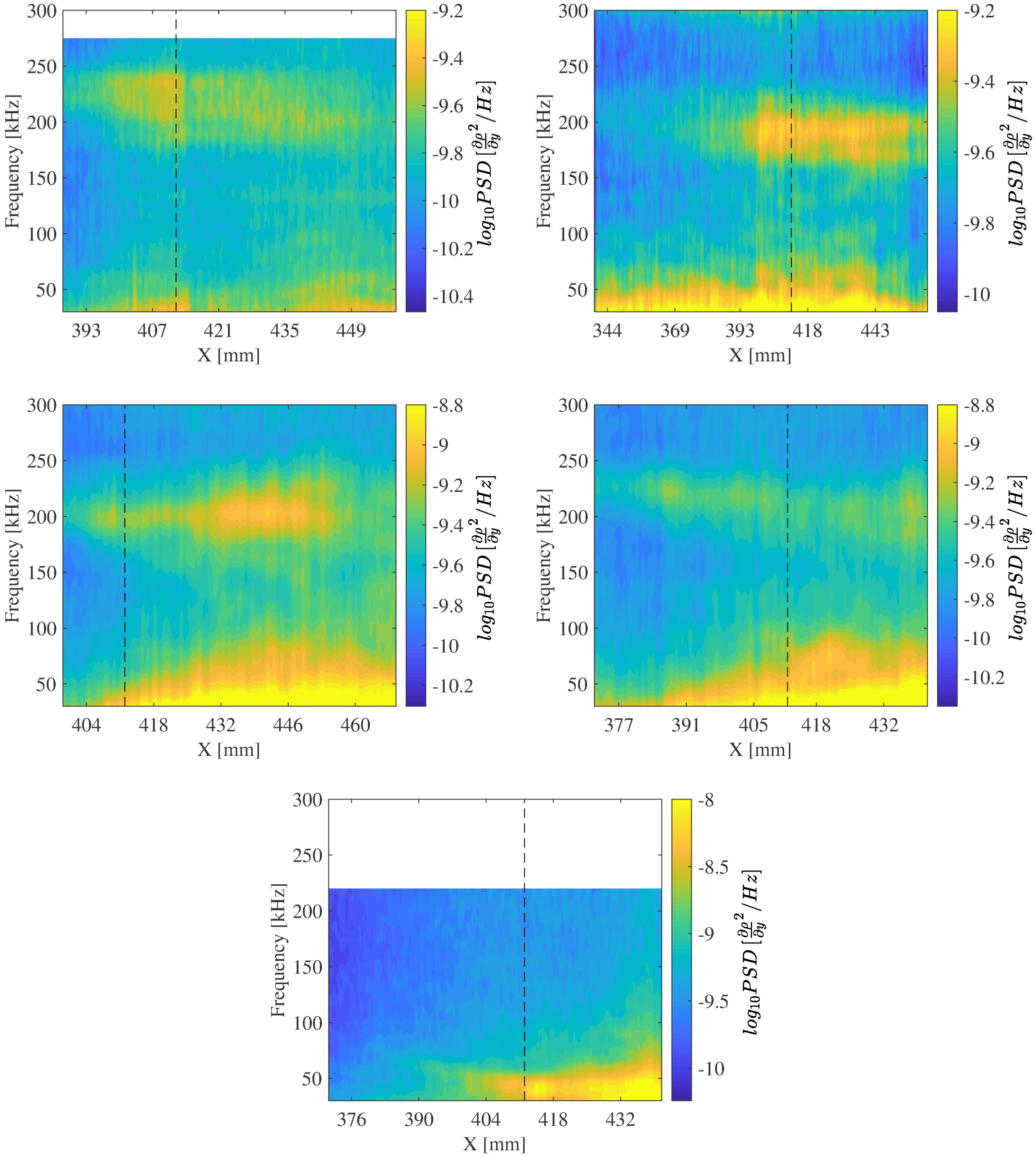

Figure 4.2: Power spectra computed along pseudo-streamlines at condition Re33 for the (top-left) -5°, (top-right) +0°, (middle-left) +5°, (middle-right) +10°, and (bottom) +15° configurations.

frequencies along the pseudo-streamline, though there appears to be some growth downstream of $X = 435\,\text{mm}$ for content at frequencies below 200 kHz.

The growth/decay characteristics of the second mode become more interesting when the boundary-layer interacts with a compression corner. In the case of a +5° compression (middle contour of figure 4.1) the wavepackets amplify substantially on the flare, peaking around X=450 mm. The pseudo-streamline spectrum downstream of this point broadens significantly, correlating well with the transitional features observed in the instantaneous flow images and the spectrum of PCB D5.

In the +10° case, the fundamental second-mode energy is seen to amplify along the frustum until the separation point at approximately X=391 mm, where it undergoes a rapid decay; this is perhaps linked to the radiation phenomenon noted earlier, though other effects may be at play. The amplitude of the second-mode fluctuations appears to freeze within the seperated shear-layer before growing substantially downstream of reattachment alongside low-frequency content near 50 kHz (seen in figure 4.2). The pronounced growth in frequencies below 100 kHz which occurs from $X = 415 - 429\,\text{mm}$ is completely absent on the straight cone, suggesting a new instability generated by the separated shear layer.

The bottom contour of figure 4.1 (+15° flare) shows consistent growth of high-frequency content within the separation bubble, in contrast to the +10° results. It is worth noting, however, that the streamline spectra in the bottom plot of figure 4.2 show no distinct peak in the second-mode range, meaning that the behavior of the second-mode is likely not captured by this spatial contour and the apparent growth

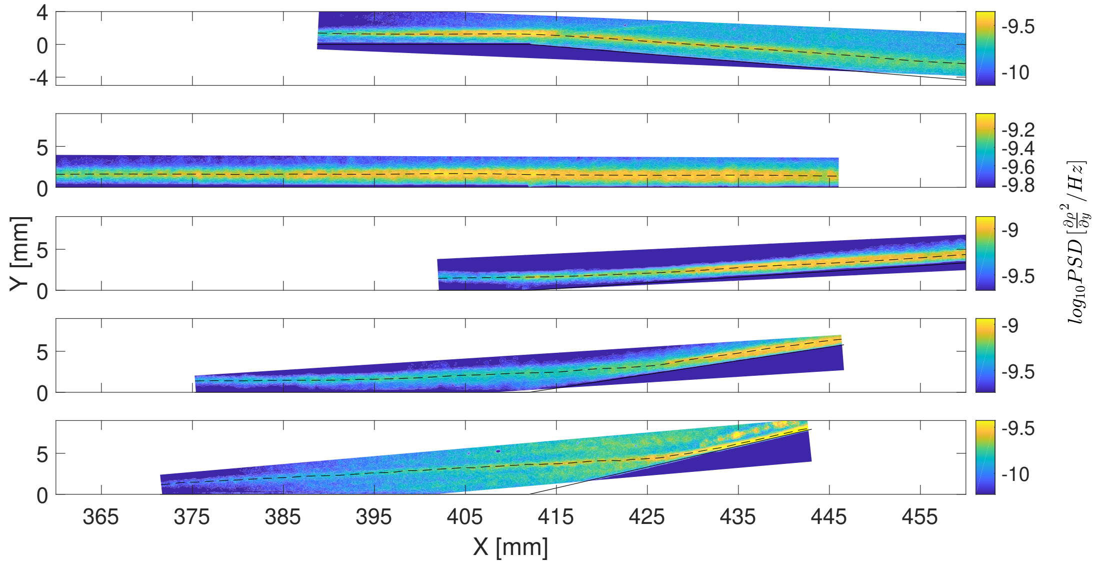

Figure 4.3: Spatial contours for each flare configuration of average PSD from $200-300\,\text{kHz}$ at condition Re45.

is instead caused by broadband amplification. This makes sense given the relative lack of distinct wavepackets observed instantaneously. Instead, low-frequency disturbances can be seen developing as far upstream as X=390 mm in the streamlie spectra, dropping from 65 kHz at onset to 40 kHz at the corner. Amplification of higher frequencies does not begin until downstream of X=432 mm.

Many of the previous observations regarding the second-mode hold at condition Re45, where the second-mode range depicted by figure 4.3 is now $200-300\,\text{kHz}$. Pseudo-streamline spectra are given in figure 4.4. The undisturbed boundary layer again shows consistent amplification of second-mode content leading up to saturation, though the magnitude of the fluctuations appears to have increased. The only notable difference from condition Re33 for the -5° case is that the radiation highlighted in figure 3.5 is visible as a line of elevated PSD emanating from the corner.

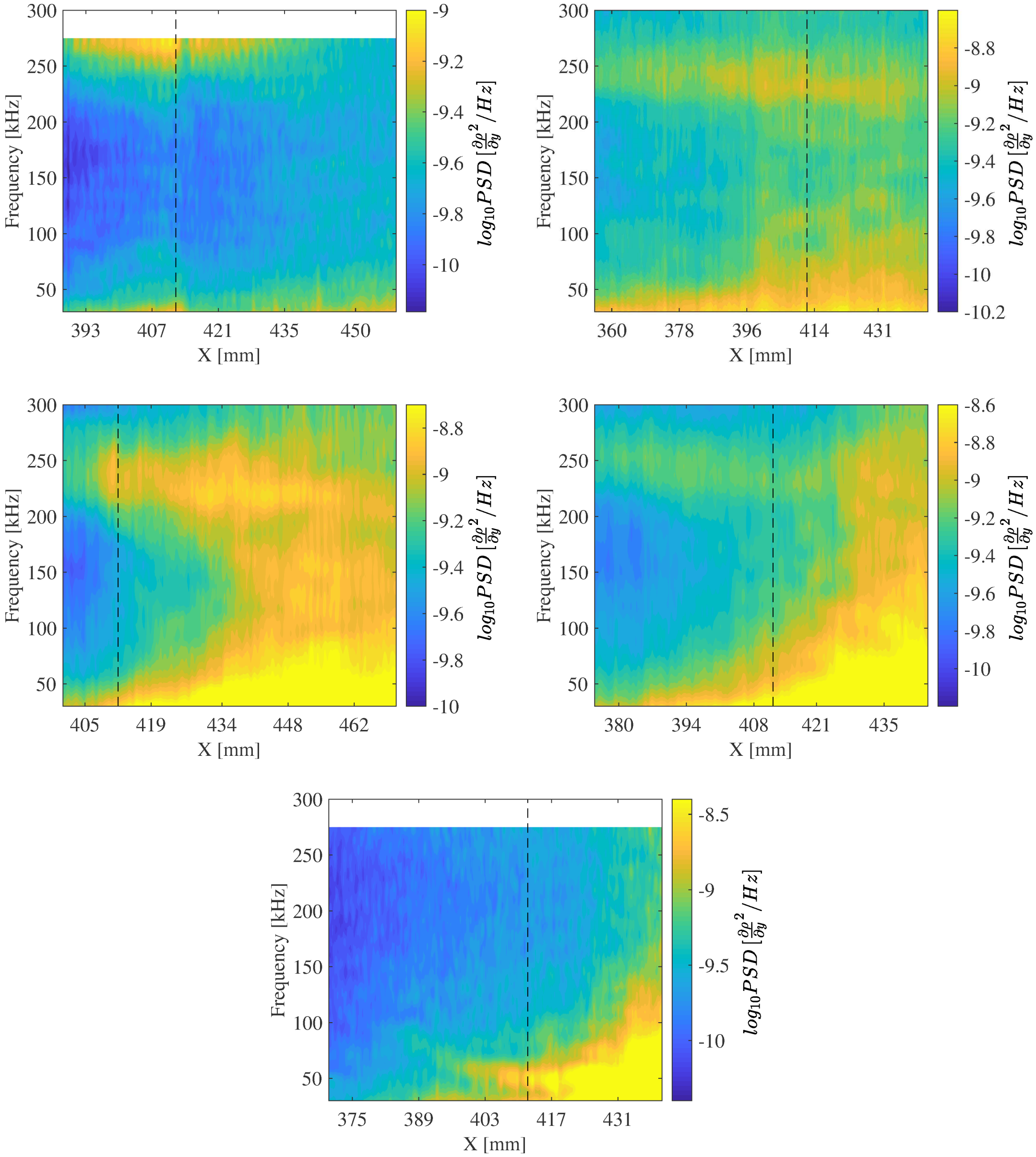

Figure 4.4: Power spectra computed along pseudo-streamlines at condition Re45 for the (top-left) -5°, (top-right) +0°, (middle-left) +5°, (middle-right) +10°, and (bottom) +15° configurations.

The +5° Re45 configuration shows second-mode content reaching off-wall distances greater than the upstream boundary-layer thickness downstream of X=440 mm; this may be attributed to intermittent turbulent behavior of the flare boundary layer. This behavior is tied to dramatic broadband excitation which is seen along the pseudo-streamline in figure 4.4 and suggests that the SWBLI promotes transition at this condition. All this is consistent with the transitional wavepacket development discussed previously in section 3.3.

As at condition Re33, the second-mode disturbances freeze in amplitude within the upstream portion of the separation bubble in the +10° case, but begin to amplify within the downstream portion of the bubble on the approach to reattachment, as in the computations of Novikov et al. [27]. Dramatic spectral broadening is observed in the vicinity of reattachment near X=430 mm. The pseudo-streamline spectra do not demonstrate a distinct shear-generated instability at this condition, though we will see that it is indeed present.

This second-mode-dominated behavior is once again contrasted slightly by the +15° results: these show amplification through the entire separation bubble in the spatial contour, though the most significant growth again occurs near reattachment. There also appears to be elevated content along the reattachment shock, similar to previously discussed radiation phenomena. However, as in the Re33 case, the pseudo-streamline spectrum pictured in figure 4.4 indicates no second-mode peak. The lack of mature second-mode waves for the +15° configuration is perhaps unsurprising given the upstream extent of the separation bubble and the freezing effect this is seen to have in the +10° configuration. Instead, the doinant feature of the

+15° pseudo-streamline spectrum is the shear-generated instability which is seen from $X = 387\,\mathrm{mm}$ and reduces in frequency from approximately 85 kHz to 50 kHz at the corner.

Spatial PSD contours (now corresponding to $230 - 330\,\mathrm{kHz}$) for the condition Re52 tests are shown in figure 4.5, where the intermittently turbulent nature of the boundary layer now has a significant effect in all configurations. For the +0° case, this manifests itself as high-frequency content further lying from the wall downstream of X=403 mm, where the disturbance strength now peaks. This also corresponds to a point beyond which significant spectral broadening is seen in the streamline spectra of figure 4.6. As with lower Re_m, the high-frequency content drops appreciably just downstream of the -5° corner but then appears to re-amplify along the flare until X=445 mm. There is also now substantial spectral broadening along the flare, likely due to wavepackets which reach the corner in a transitional state.

Just downstream of the +5° compression, the high frequency content amplifies rapidly and apparently saturates. This is accompanied by nearly instantaneous spectral broadening, with the power of lower frequencies rising to meet or exceed the second-mode power. The high-frequency content in the +10° case grows steadily along the frustum and decays slightly downstream of separation from X=$403 - 413\,\mathrm{mm}$. As the flow reattaches, this content amplifies and spreads out rapidly to cover an off-wall distance significantly greater than the upstream boundary-layer thickness, again implying transition. This behavior is mirrored by the +15° configuration, where the turbulent state of the flare boundary layer is

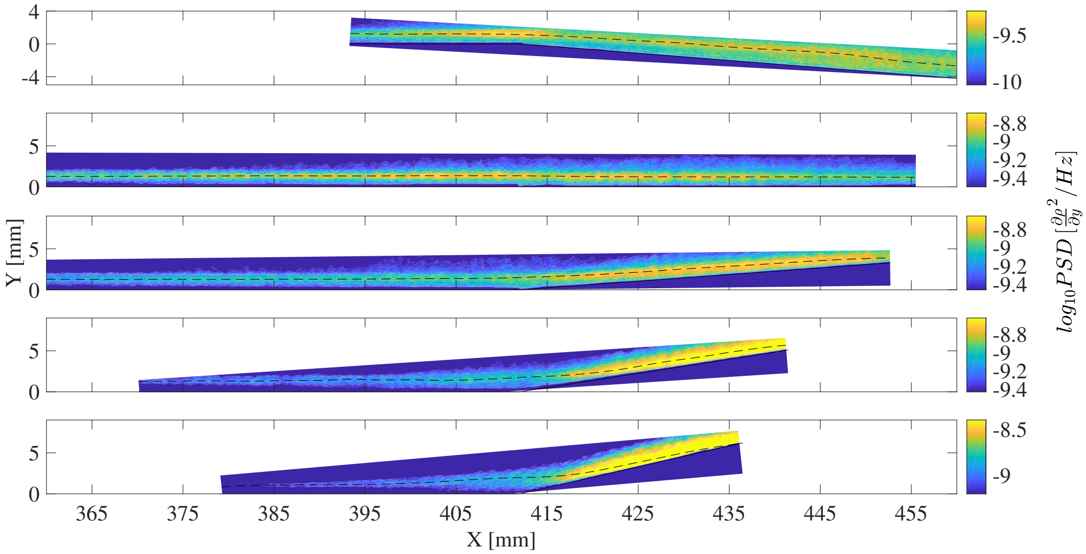

Figure 4.5: Spatial contours for each flare configuration of average PSD from 230 − 330 kHz at condition Re52.

even more obvious. Both separated configurations display the same instantaneous spectral broadening immediately at the corner in figure 4.6. The low-frequency signature of the shear-mode has largely vanished from the streamline spectra for the +15° extension even upstream of this point.

4.2 N Factors

A common metric for quantifying disturbance growth is the N factor, which is a spatial integration of the amplification rate. The spectra along the pseudo-streamlines may also be used to compute changes in N factors for each frequency according to

$$\Delta N(f, x_i) = \frac{1}{2} \ln \left(\frac{PSD(f, x_i)}{PSD(f, x_0)} \right), \tag{4.1}$$

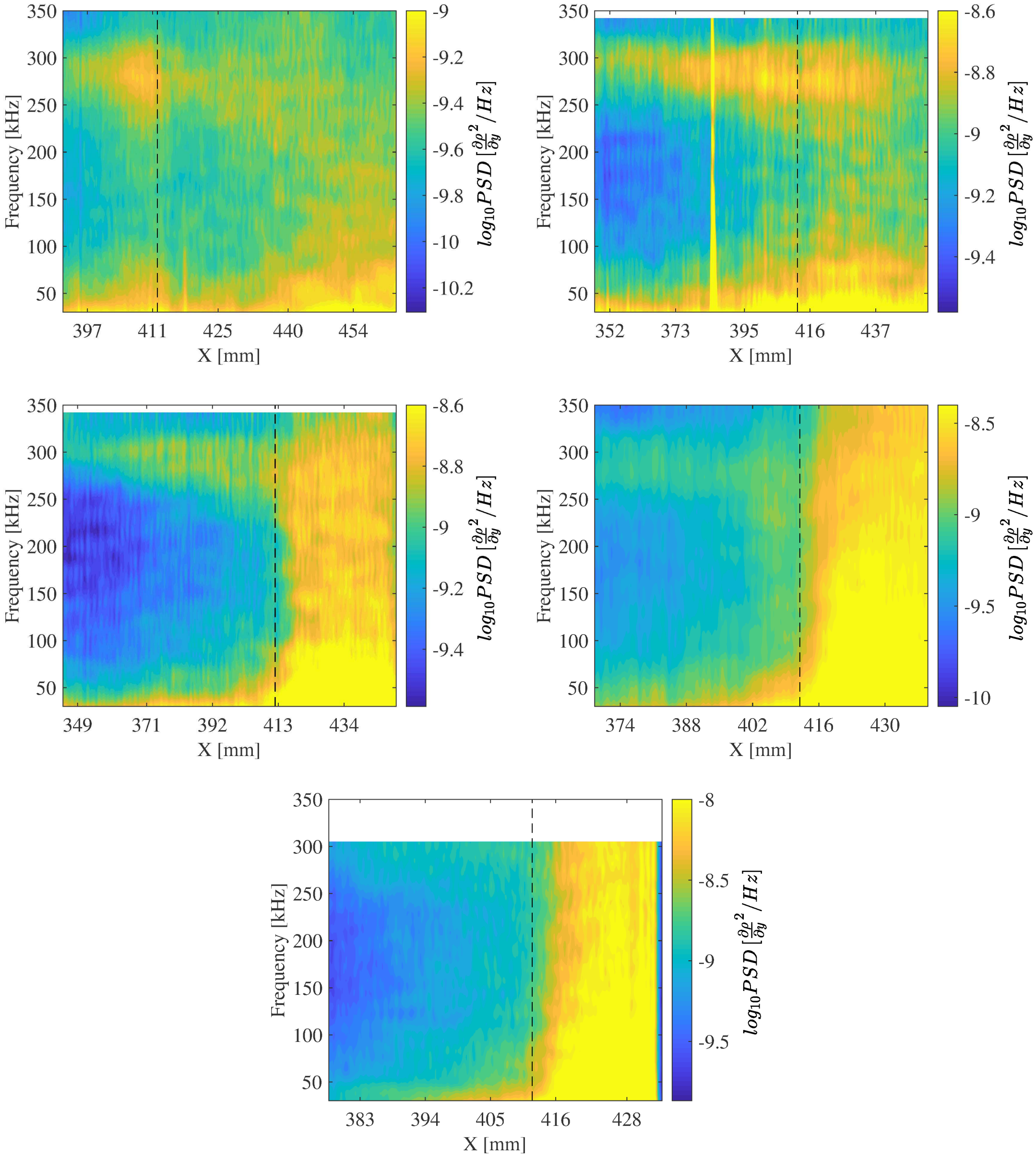

Figure 4.6: Power spectra computed along pseudo-streamlines at condition Re52 for the (top-left) -5°, (top-right) +0°, (middle-left) +5°, (middle-right) +10°, and (bottom) +15° configurations.

where $PSD(f, x_i)$ refers to the power of frequency f at streamwise location x_i, and x_0 refers to the upstream edge of the field of view. The change in N factor calculated in this manner applies to the density-gradient fluctuations recorded by the schlieren apparatus; if we are to extend these results to the density fluctuations that would typically be of more interest, we must invoke the parallel flow assumption [17]. This assumption will become questionable across and immediately downstream of the corner and within regions of flow separation, so caution should be exercised in interpreting these results (quantitatively).

The N factors for each configuration at condition Re33 are given in figure 4.7 plotted against the stability Reynolds number ($\mathrm{R} = \sqrt{Re_s}$) which is based on freestream conditions and the surface coordinate. Nondimensional frequencies are included based on the theoretical boundary-layer thickness at the corner, δ_c, and the theoretical edge velocity along the frustum, U_e. These contours demonstrate relative amplification of disturbances and thus may reveal key spectral development at frequencies that are not apparent in the raw PSD.

The undisturbed boundary layer only demonstrates strong amplification within the second-mode band. The expansion causes a rapid drop in N factor for the dominant second-mode frequency of approximately 0.4; the magnitude of this drop is consistent across all conditions. Disturbances from 175 − 200 kHz then amplify downstream of the corner, likely corresponding to lower-frequency second-mode waves, and bands of growth appear at 60, 90, and 140 kHz. Flow structures which may account for these and other peaks throughout this section are discussed in chapter 5.

The amplification of content below 50 kHz caused by the $+5^\circ$ compression,

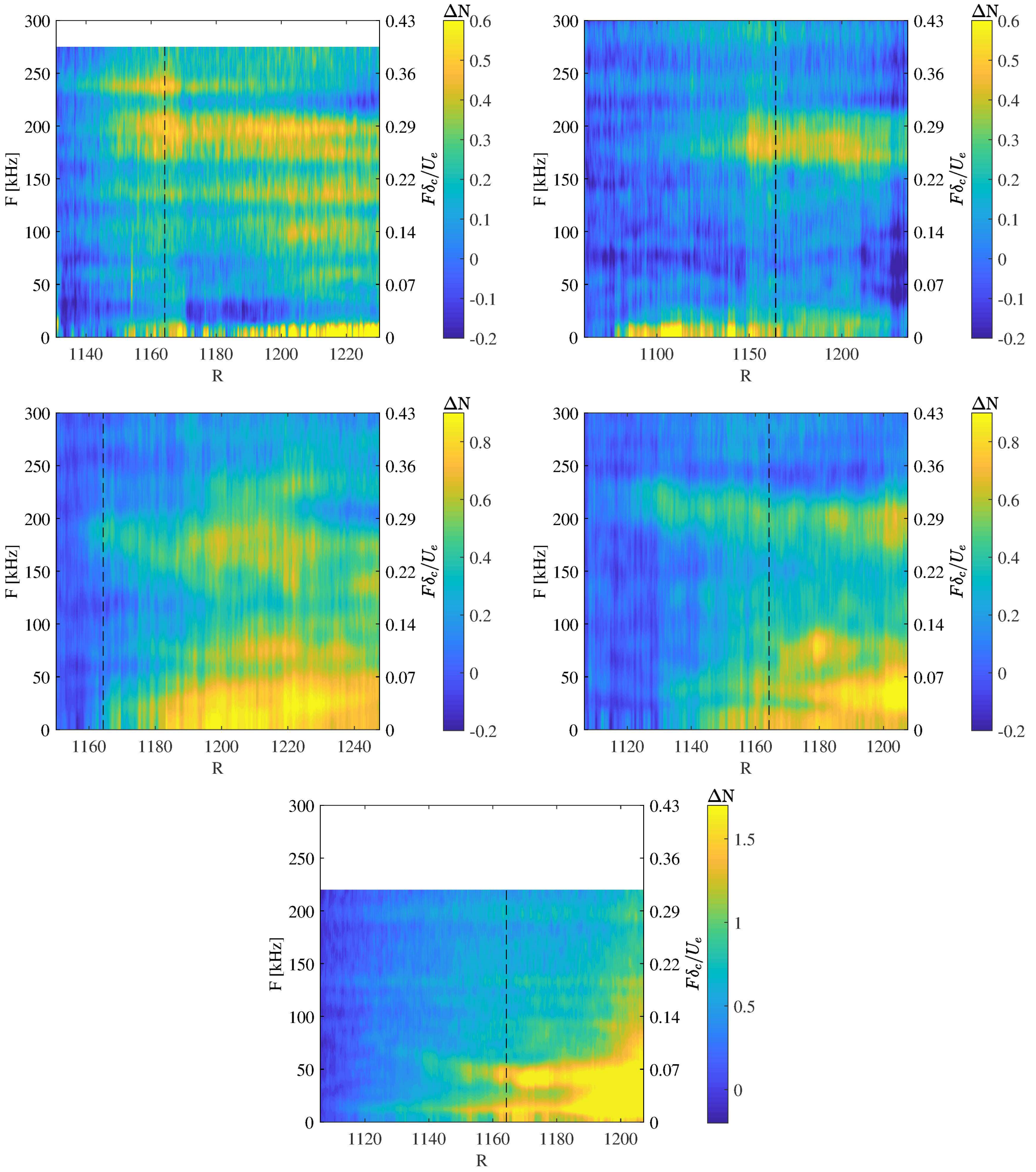

Figure 4.7: N-factor increase computed along pseudo-streamlines at condition Re33 for the (top-left) -5° , (top-right) +0° , (middle-left) +5° , (middle-right) +10° , and (bottom) +15° configurations.

which was noted in figure 4.2, is more distinct here, and there is evidence of an additional disturbance developing at 75 kHz. Figure 4.7 also shows that the second-mode amplification extends to higher frequencies along the flare, matching the PCB observations. The N-factor spectra also help us better identify key low-frequency content for the separated cases. Within the +10° separation bubble, two bands of growth are observed: one at $70-80$ kHz which peaks within the separation region and decays slightly as the boundary layer reattaches, and another at $30 - 40$ kHz which continues to amplify downstream. We will demonstrate that the upper-band corrresponds to a shear-generated instability similar to that observed instantaneously with the +15° extension. The N-factor contour for the +15° compression is similarly dominated by two bands of growth, now at approximately 15 kHz and 45 kHz. It is worth noting that the N factors for the +15° case reach much greater levels than any other configuration, which would indicate that the amplification rates for the shear-layer instabilities are higher than for any second-mode.

At condition Re45 (figure 4.8), second-mode disturbances in the +0° configuration do not attain the same levels of amplification as at condition Re33 due to the earlier onset of saturation. Strong bands of relative growth are observed around 155 kHz and 190 kHz in the expansion case, though it should be noted that these frequencies are particularly weak at the upstream edge of the field of view (where the reference power is considered). The +5° configuration causes the growth of content at approximately 150 kHz and 80 kHz, both of which appear as distinct bands and may correspond to new flow structures. Amplification for the +10° configuration is largely concentrated downstream of reattachment, though there is evidence of weakly

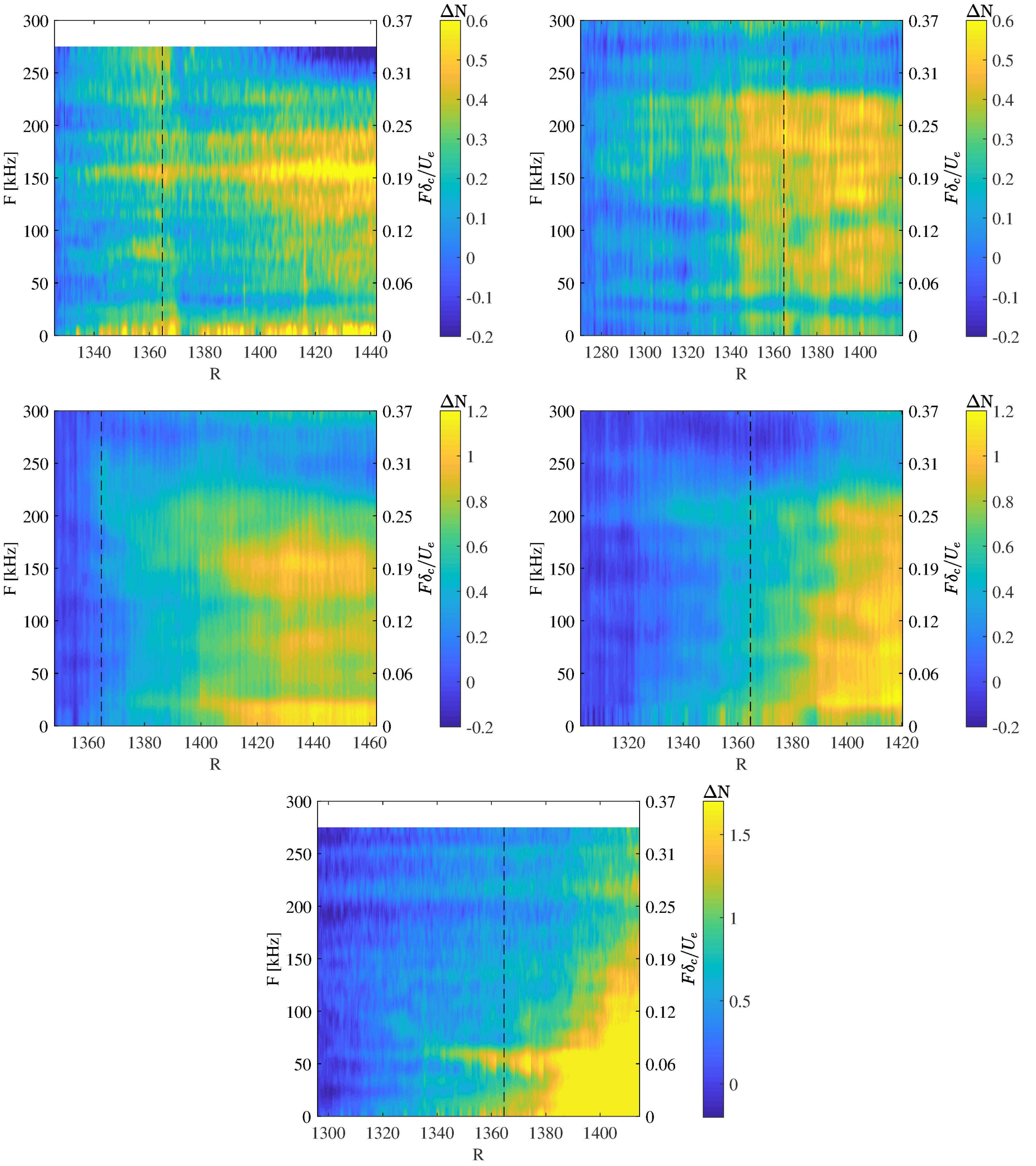

Figure 4.8: N-factor increase computed along pseudo-streamlines at condition Re45 for the (top-left) -5° , (top-right) +0° , (middle-left) +5° , (middle-right) +10° , and (bottom) +15° configurations.

amplifying disturbances at 80 kHz from $R = 1300 - 1330$ which may correspond to intermittent shear waves. Strong growth concentrated around 50 kHz is observed for the +15° configuration, again corresponding to a distinct, shear-generated instability. Substantial low-frequency amplification occurs downstream of the corner near the reattachment zone.

Switching focus to condition Re52 in figure 4.9, the N factors for the -5° configuration demonstrate significant amplification of frequencies both higher and lower than the upstream second-mode fundamental. The low-frequency growth is considerably less concentrated than at lower Re_m, though it appears to peak around 120 kHz. All three compression cases are characterized by rapid, broadband amplification downstream of the corner, with no clearly dominant frequencies. Note that the contour limits are increased for higher flare angles as the amplification becomes much stronger.

4.3 Low-frequency Behavior

The consistent generation of low-frequency content, particularly in the separated cases, justifies a spatial analysis with the frequency range of interest instead chosen to bracket the potential shear-generated instability. Figure 4.10 shows energy generated from $40 - 80$ kHz for each configuration at condition Re33. Downstream of the expansion corner in the first contour, content at these frequencies undergoes an initial decay similar to that observed for the second-mode disturbances. This is then followed by another period of amplification near X=435 mm, which is also captured

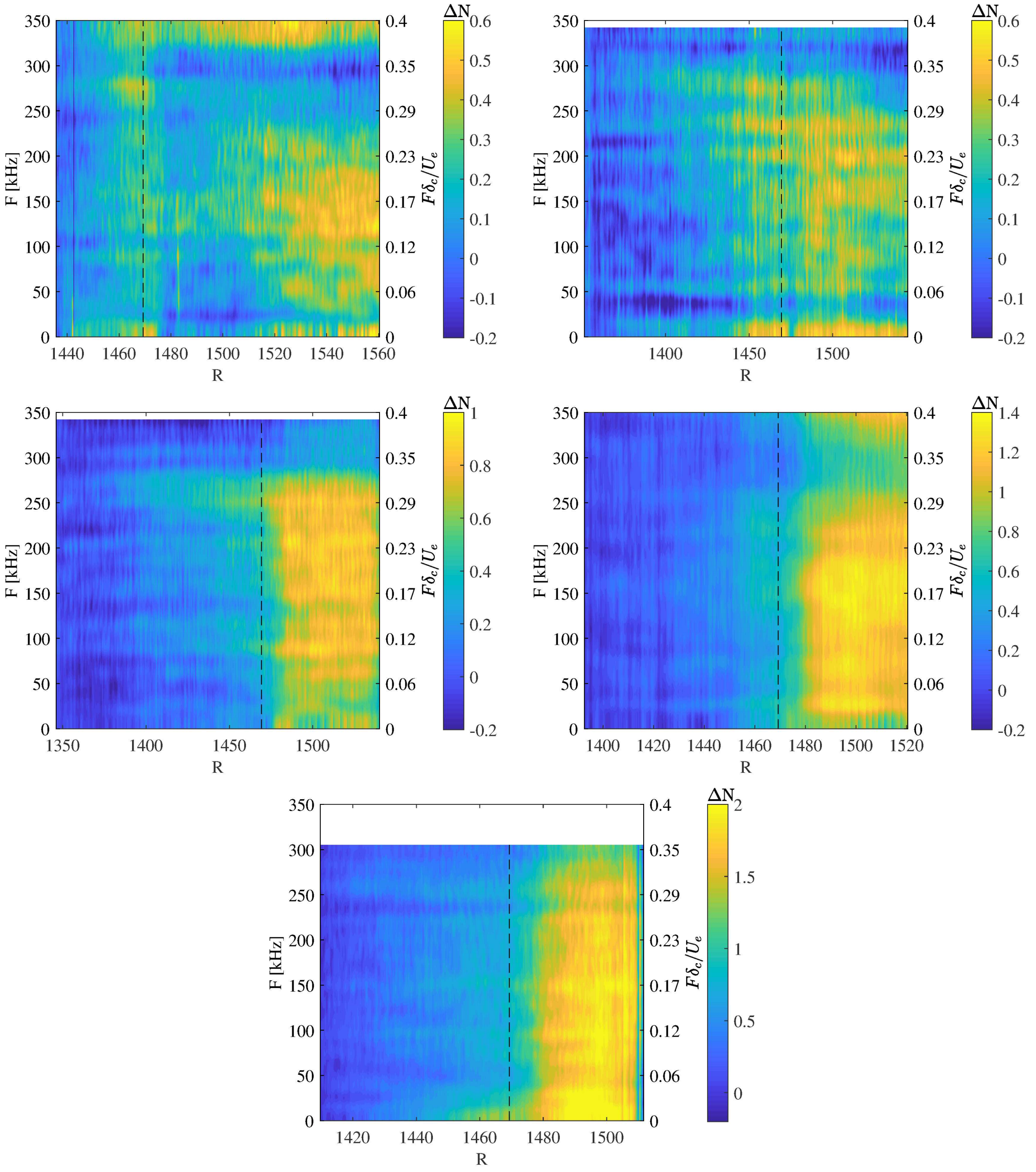

Figure 4.9: N-factor increase computed along pseudo-streamlines at condition Re52 for the (top-left) -5°, (top-right) +0°, (middle-left) +5°, (middle-right) +10°, and (bottom) +15° configurations.

by the N factors in figure 4.7. Growth also occurs downstream of the +5° corner in the vicinity of the pseudo-streamline.

This is dwarfed by the content generation observed in the separated regions of the +10° and +15° configurations. For the +10° extension, much of the amplification occurs from X=410 − 430 mm as the separation bubble is compressing towards reattachment. As mentioned previously, both pseudo-streamline contours (figures 4.2 and 4.7) show growth of a distinct 75 kHz band within this region, whereas the amplification seen along the flare is likely due to the 40 kHz peak seen in the N-factor plot. These observations largely hold for the +15° case, but the disturbance amplification can be discerned as far upstream as X=390 mm and reaches a much greater magnitude. There is also evidence of energy emanating away from the separation bubble at approximately X=415 mm, which correlates well with the behavior noted in the reference-subtracted sequences. The low-frequency content along the flare for this configuration is more likely due to the persistence of the shear waves given the lack of multiple N-factor peaks within this frequency range.

Figure 4.11 shows little change regarding low-frequency content generation at condition Re45 (now 50 − 90 kHz) for the -5° and +0° cases. As noted in the streamline discussion, however, the +5° compression causes greater low-frequency amplification than at condition Re33. The spatial amplification seen along the flare for this configuration is likely most attributable to the N-factor peak around 80 kHz, as both peaks begin to dissipate at approximately $X = 455$ mm.

The +10° compression shows evidence of the shear-generated instability developing within the separation bubble; this was obscured in the pseudo-streamline

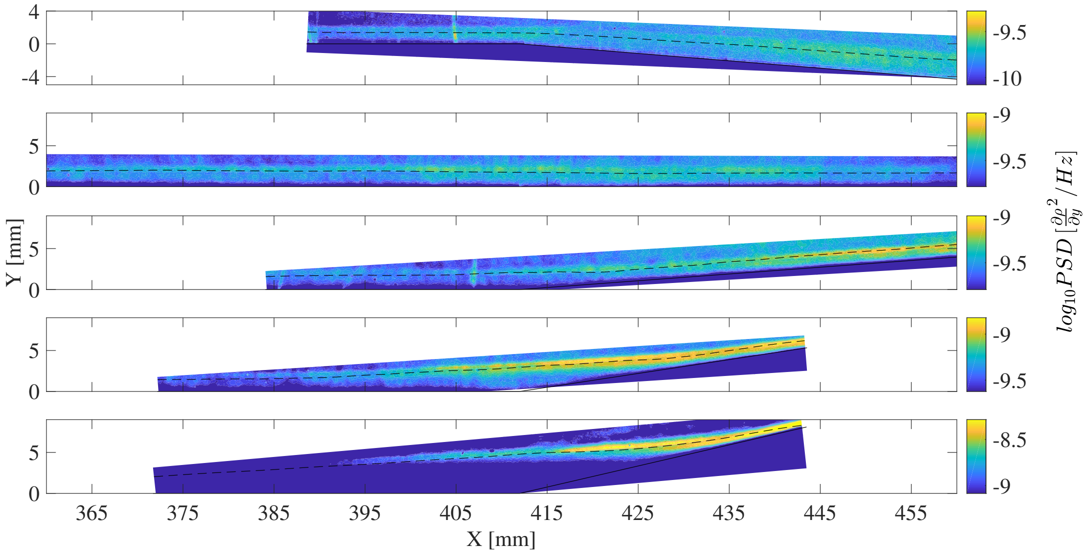

Figure 4.10: Spatial contours for each flare configuration of average PSD from $40 - 80\,\text{kHz}$ at condition Re33.

spectra, though the growth is concentrated more within the downstream portion from X=415 − 425 mm. This content amplifies further downstream of reattachment, but the pseudo-streamline spectra of figures 4.4 and 4.8 suggest this is due more to spectral broadening and transition.

The shear-generated instability for the +15° configuration again develops far upstream of the corner. There is a brief but notable drop in PSD directly above the corner at X=412 mm where significant energy is seen emanating from the shear layer. This drop is not captured in figure 4.4 because the maximum low-frequency fluctuations occur further from the wall than the high-frequency fluctuations and therefore do not lie along the pseudo-streamline. The growth and slight decay of the shear disturbances illustrated here correlate well with the production terms for the baroclinic instability identified by Dwivedi et al. [2] for a 2D compression ramp, depicted in figure 4.12, suggesting a similar mechanism may be at work. Another

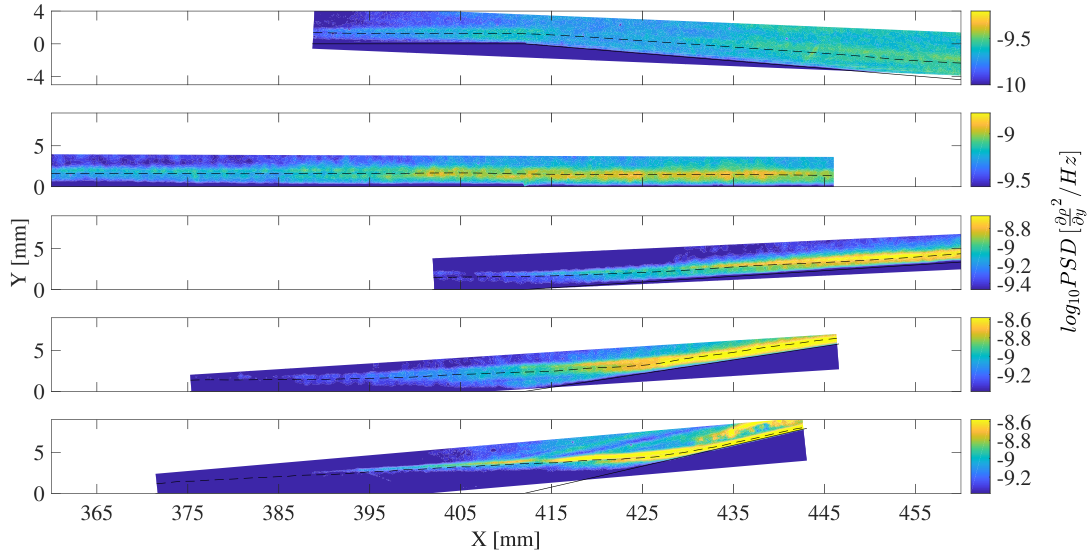

Figure 4.11: Spatial contours for each flare configuration of average PSD from 50 − 90 kHz at condition Re45.

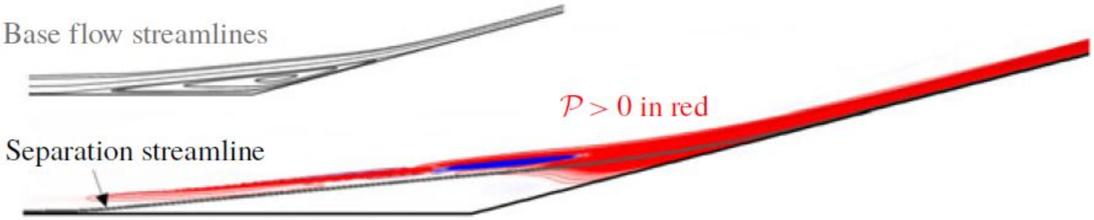

Figure 4.12: Distribution of the production term P for steady perturbations. Taken from Dwivedi et al. [2].

particularly strong ray of energy is observed originating from the reattachment zone in the spatial contour. The pseudo-streamline spectrum shows significant spectral broadening around this same point at approximately X=430 mm.

At condition Re52, the low-frequency content experiences transition-related amplification in all configurations (figure 4.13). Note that the large artifact for the straight case at around X=387 mm is due to debris which passes through the field of view, contaminating the spectra. This also appears as a broadband spike in figure 4.6. Contrasting with the results at lower Re_m, the -5° case now shows the

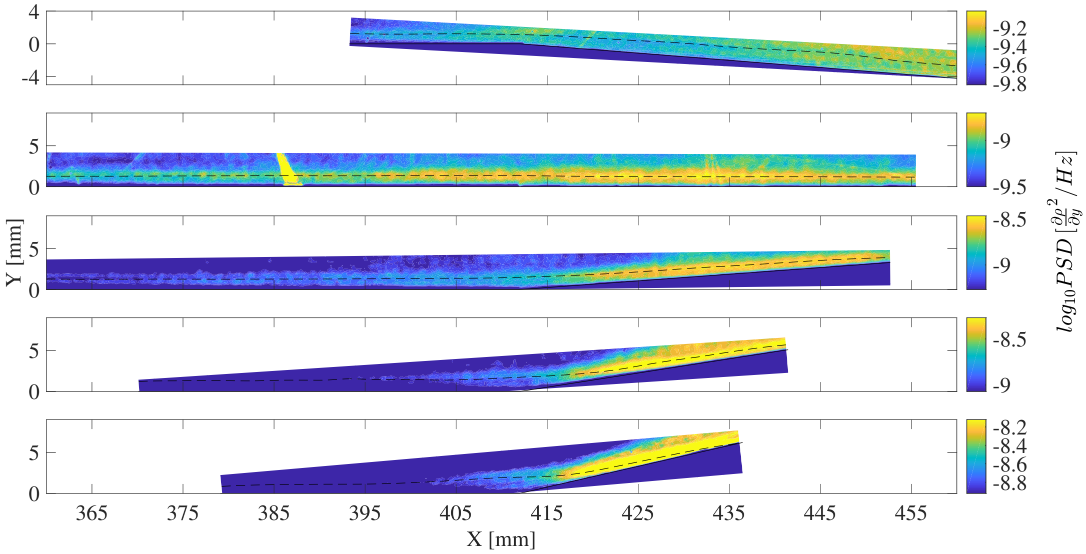

Figure 4.13: Spatial contours for each flare configuration of average PSD from $60 - 100\,\mathrm{kHz}$ at condition Re52.

low-frequency band reaches levels towards the end of the flare which exceed those seen upstream of the corner and are not confined to the pseudo-streamline. This is unsurprising given the previously discussed spectral broadening along the extension which was attributed to turbulent structures. The +0° and +5° configurations show the same qualitative trends as at condition Re45 but with greater amplification. The separated cases no longer show significant evidence of the shear-generated instability, though low-frequency content does amplify within the separation bubbles. Both configurations then show abrupt amplification upon reattachment, as was seen in the streamline spectra. This is to be expected given the turbulent nature of the flare boundary layer observed in the schlieren images.

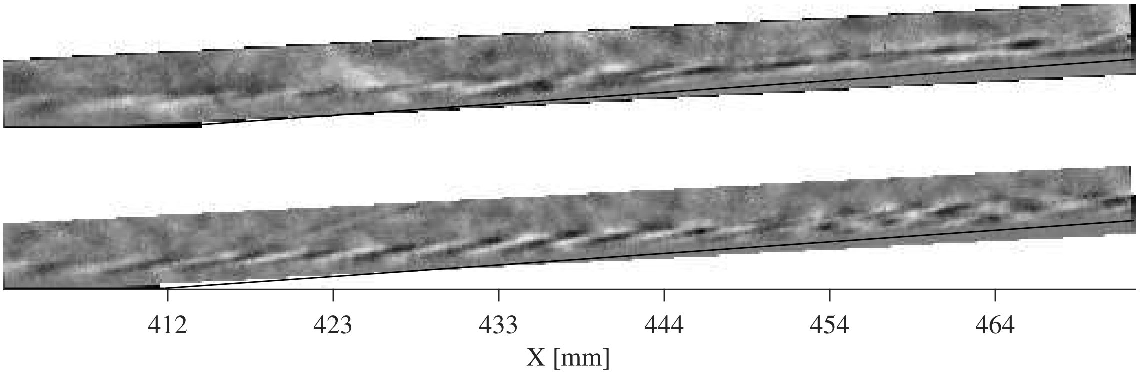

Figure 4.14: (Top) Reference-subtracted image and (bottom) bandpass-filtered ($200 - 300\,\mathrm{kHz}$) image obtained at condition Re45 with the $+5°$ extension.

4.4 Bandpass-filtered Images

The evolution of modal content identified through the preceding analysis can be observed in a time-resolved sense by applying a temporal bandpass filter to each pixel time series, then stitching these filtered series back into image sequences. An example is given in figure 4.18 where a reference-subtracted image obtained with the $+5°$ configuration at condition Re45 is displayed above the corresponding image after applying a $200 - 300\,\mathrm{kHz}$ bandpass filter to the raw time series. Both images clearly depict a second-mode wavepacket traversing the corner, but the filter enhances the visibility of the second-mode flow structures as well as the radiation phenomenon observed at the corner (though this is still more obvious when viewing the videos).

In similar fashion, this technique may be employed to highlight the low-frequency, shear-generated disturbances present in the $+15°$ configuration. An image sequence created with a passband of $30 - 80\,\mathrm{kHz}$ is depicted in figure 4.15 for condition Re45. We can now distinguish the disturbance development even at the

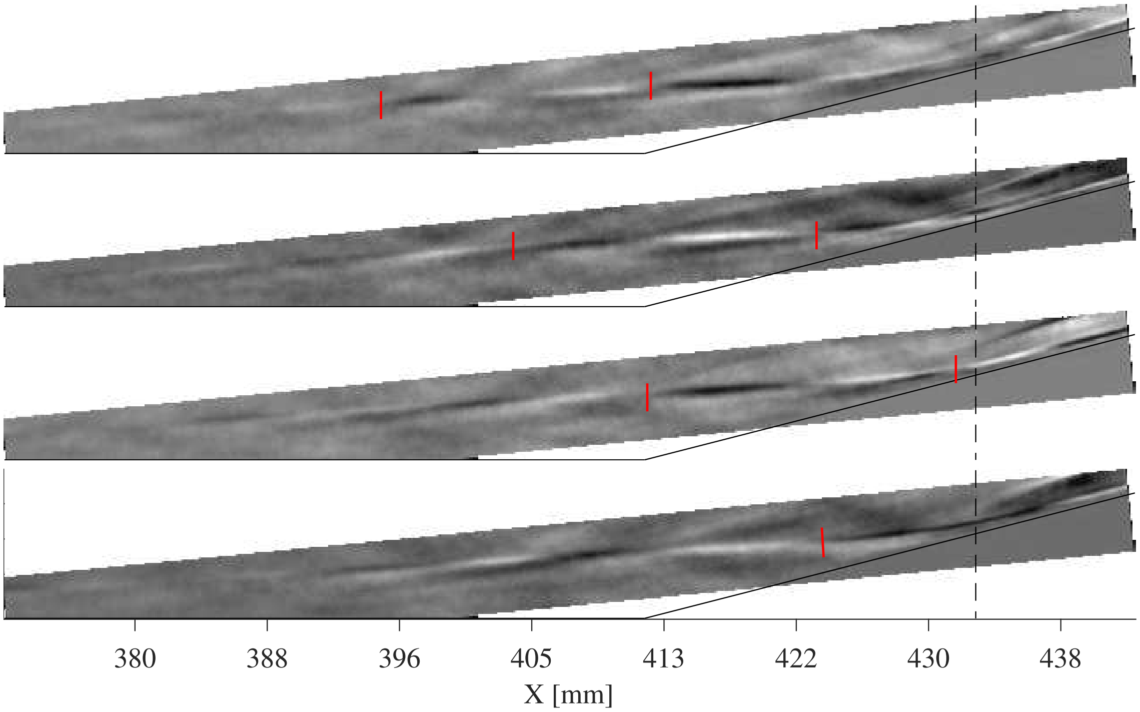

Figure 4.15: Bandpass-filtered ($30 - 80\,\mathrm{kHz}$) sequence for the $+15°$ configuration at condition Re45; images are spaced by $10.9\,\mu\mathrm{s}$.

upstream edge of the field of view. This image sequence emphasizes the ray of energy emanating away from the shear layer at $X = 412\,\mathrm{mm}$, just above the corner. It is beyond this point at which the disturbances develop their distinctly braided appearance.

One particularly useful application of this technique is to probe for disturbances that are less easily identified in the reference-subtracted images. Figure 4.16 depicts a sequence obtained by filtering $+10°$ configuration, condition Re33 images with a passband of $70-86\,\mathrm{kHz}$, intended to isolate the shear-generated disturbances which should clearly exist based on the N-factor peak in figure 4.8. A braided structure is clearly visible developing within the separation region that correlates spatially with the amplitude peak in figure 4.10, and has a similar structure to the distur-

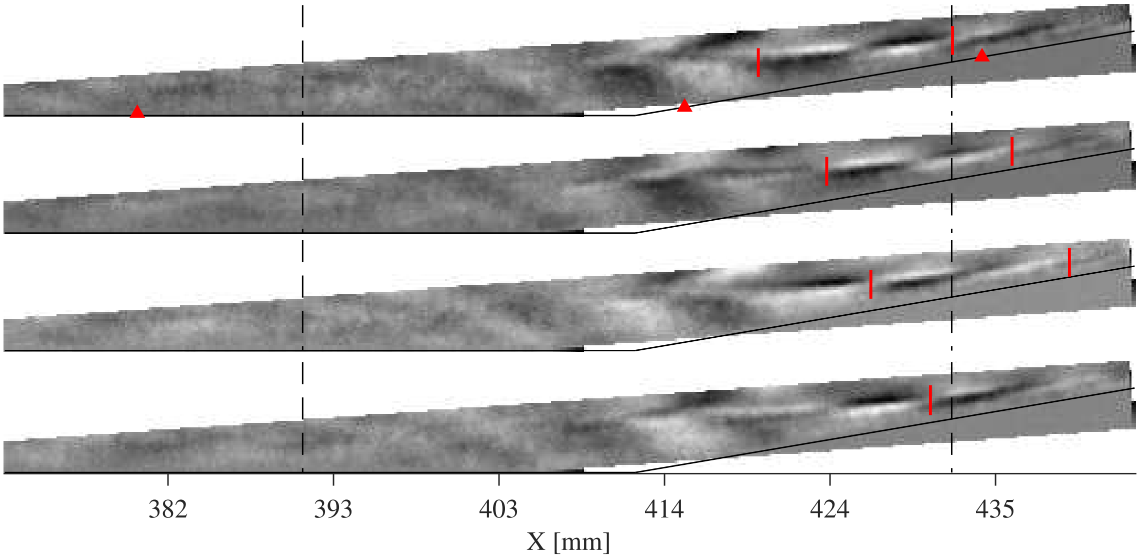

Figure 4.16: Bandpass-filtered ($70 - 86\,\mathrm{kHz}$) sequence for the $+10°$ configuration at condition Re33; images are spaced by $3.65\,\mu$s.

bances observed within the separation bubble of the $+15°$ configuration. A distinct ray of energy is once again seen coming from the shear layer just above the corner. These low-frequency braided structures are found propagating when there is no evidence of second-mode content, indicating that they correspond to independent instability mechanisms.

The $+5°$ configuration image sequence from condition Re33 was bandpass filtered from $10 - 50\,\mathrm{kHz}$ to probe the low-frequency amplification observed along the pseudo-streamline in the N-factor plot of figure 4.7. A sample sequence is shown in figure 4.17 with an inter-image spacing of $14.6\,\mu$s. Periodic features are seen propagating along the flare with a braided structure very similar to that of the shear-generated disturbances which appear in the separated cases. These disturbances are found coexisting with second-mode wavepackets, but also appear when there is no evidence of high-frequency content. Thus, it appears that the streamline

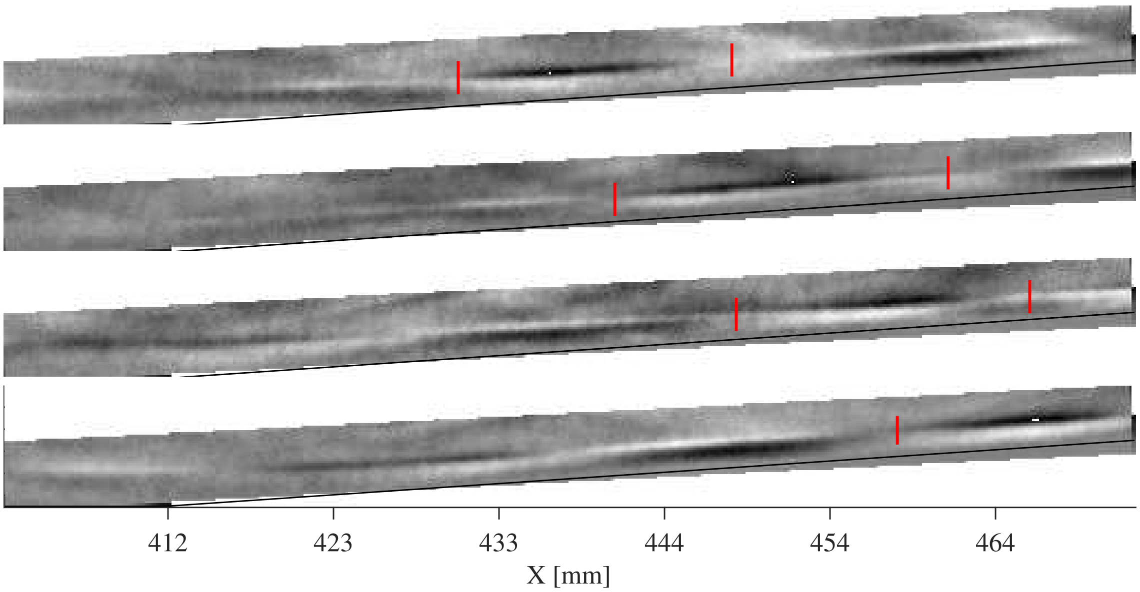

Figure 4.17: Bandpass-filtered ($10 - 50\,\mathrm{kHz}$) sequence for the +5° configuration at condition Re33; images are spaced by $14.6\,\mu\mathrm{s}$.

curvature at the corner may provoke the development of new disturbances even in the absence of a separation bubble.

This strategy of bandpass-filtering the images also allows us to observe harmonic second-mode content despite the insufficient framerate by taking advantage of aliasing. We will demonstrate this for a test at condition Re45 on the -5° configuration. The dominant second-mode frequency for this test was approximately $250 - 260\,\mathrm{kHz}$ (based on the PCB spectra), which would imply a harmonic frequency of $500-520\,\mathrm{kHz}$. Based on the camera framerate of $550\,\mathrm{kHz}$, this harmonic would be aliased down to $30 - 50\,\mathrm{kHz}$. Shown in figure 4.18 is a single reference-subtracted image (top) and the corresponding image after applying a $30 - 80\,\mathrm{kHz}$ bandpass filter (bottom). A second-mode wavepacket is clearly seen in the reference-subtracted image upstream of the corner. The filtered image displays a rope-like structure propagating alongside this wavepacket, but with a much shorter wave-

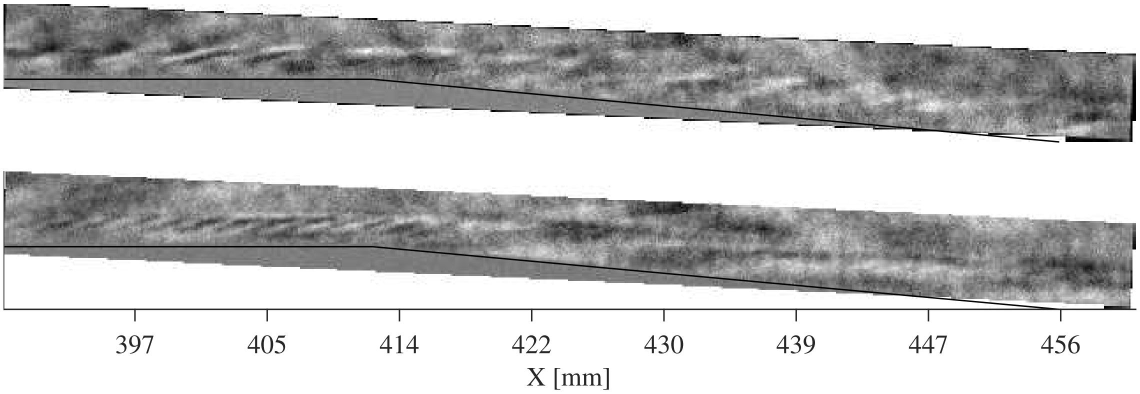

Figure 4.18: (Top) Reference-subtracted image and (bottom) bandpass-filtered (30−80 kHz) image for the -5° configuration at condition Re45.

length. We can confirm this to be the second-mode harmonic by extracting the pixel signal along the pseudo-streamline for these images and computing the spatial PSD to determine the dominant wavelength in each. Figure 4.19 shows a comparison of the PSD for the two images computed with pixels only up to $X = 422\,\mathrm{mm}$ (beyond which the wavepacket becomes indistinct). The reference-subtracted image peak wavelength corresponds to the second-mode disturbance and lies between 4.1 mm and 4.4 mm. The peak wavelength of the bandpass-filtered image is 2.2 mm, approximately half that of the fundamental.

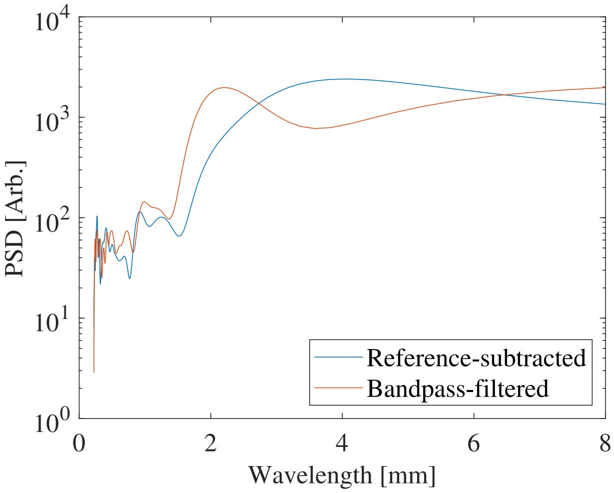

Figure 4.19: Comparison of dominant wavelengths within the reference-subtracted and bandpass-filtered images.

Chapter 5: Spectral Proper Orthogonal Decomposition

The structure and evolution of disturbances may also be analyzed through the Spectral Proper Orthogonal Decomposition (SPOD) methodology of Towne et al. [42]. This technique provides a set of orthogonal modes which oscillate at distinct frequencies and describe the coherent evolution of flow structures in both time and space. By resolving these modes, we may be able to identify the flow structures responsible for the amplification peaks observed in chapter 4. Also, as will be shown in chapter 6, this technique is particularly useful when coupled with bispectral analysis, as it provides a method to probe the physical structure of frequencies which dominate nonlinear growth mechanisms. In the present implementation, Hann windows of length 64, 128, or 256 were used (depending on the framerate of the test) with 50% overlap to group the images of each sequence, resulting in a minimum of 34 flow realizations for an individual test. The specific parameters for each computation are given in table 5.1.

5.1 $+0^\circ$ Extension

As has been established, the boundary layer on the straight-cone configuration is largely dominated by the second-mode instability; this is confirmed by the SPOD

Extension	Condition	N_f [frames]	L_{hann} [frames]	Realizations
-5°	Re33	3350	128	51
	Re45	3305	128	50
	Re52	4490	128	69
+0°	Re33	3720	128	56
	Re45	3800	128	58
	Re52	3690	128	56
+5°	Re33	4900	256	37
	Re45	6000	256	45
	Re52	4500	256	34
+10°	Re33	5000	256	38
	Re45	5920	256	45
	Re52	5000	256	38
+15°	Re33	2400	128	36
	Re45	1300	64	39
	Re52	3000	128	45

Table 5.1: Parameters for SPOD computations.

analysis. The energy of the SPOD modes computed for each condition are given in figure 5.1, where we see a distinct peak in the highest-ranked mode around the fundamental second-mode frequency of each test. Throughout this chapter, only the highest-ranked mode will be considered for analysis, as it respresents the greatest energy content and appears to capture the dominant instability mechanisms. Note that the second-mode peak appears reduced at Re52; this is due to turbulent content which posseses significant flow energy but is less structurally coherent.

Eigenvalue contours for select SPOD modes for condition Re33 on the straight cone are given in figure 5.2. The 160, 184, and 228 kHz contours show the typical rope-like structure of the second-mode disturbances at three different frequencies. The 160 kHz mode does not develop a coherent structure until X=400 mm, which is also the point at which the streamline spectrum of figure 4.2 demonstrated significant spectral broadening. At 184 and 228 kHz, the disturbances amplify from the up-

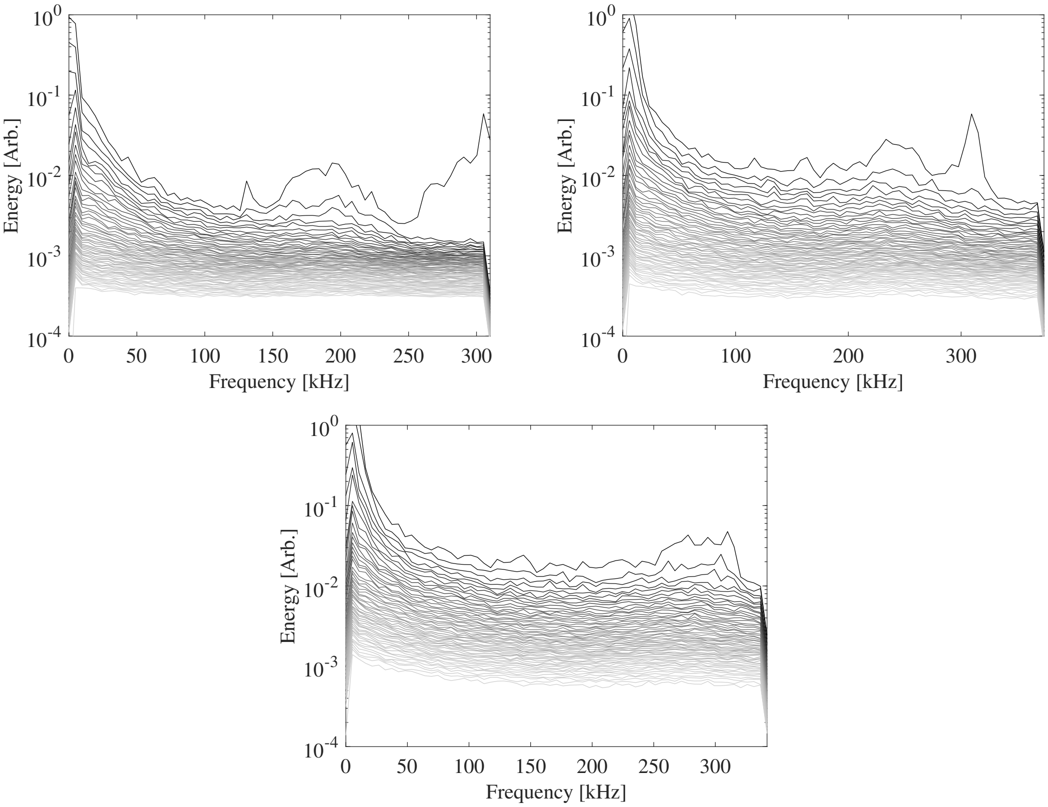

Figure 5.1: SPOD mode energy for the +0° extension at (top-left) condition Re33, (top-right) condition Re45 and (bottom) condition Re52.

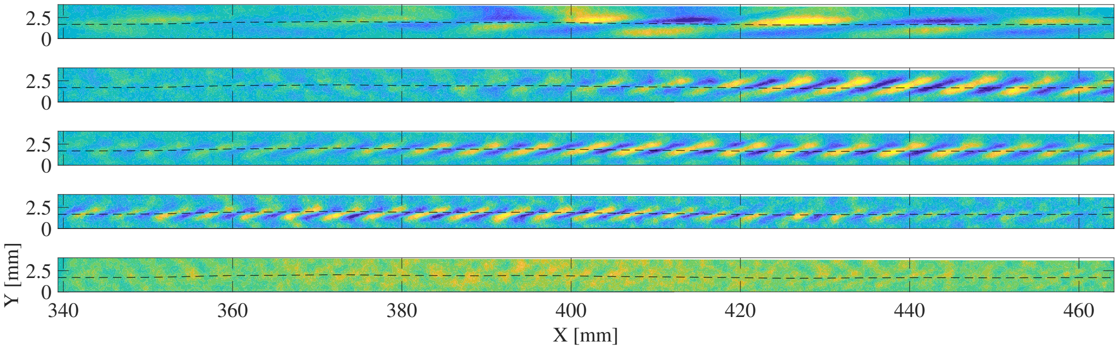

Figure 5.2: SPOD mode shapes for the +0° configuration at condition Re33 for frequencies of (top to bottom) 34 kHz, 160 kHz, 184 kHz, 228 kHz, and 280 kHz.

stream end of the FOV until approximately X=440 mm where both modes begin to dissipate; this behavior also matches observations made along the pseudo-streamline. While these second-mode disturbances are dominant, the aforementioned spectral broadening extends to low-frequency content. The top contour of figure 5.2 shows coherent structures at 34 kHz amplifying as far upstream as X=380 mm. These structures appear similar to the braided structures observed along the +5° flare in the $10 - 50$ kHz bandpass-filtered sequence of figure 4.17. The presence of these structures in the undisturbed case is somewhat surprising; however, the significance of SPOD modes must be determined within the context of other results and the lack of an amplification peak for this frequency reduces its relevance. Furthermore, the freestream noise environment of HyperTERP is likely to excite low-frequency disturbances which may not be present in the flight environment. The large spike in SPOD energy from $250 - 300$ kHz is exemplified by the 280 kHz mode, which corresponds to uniform flickering; this is thus a noise mode from the schlieren apparatus and can be safely ignored.

The enhanced growth of low-frequency content at condition Re45 is demon-

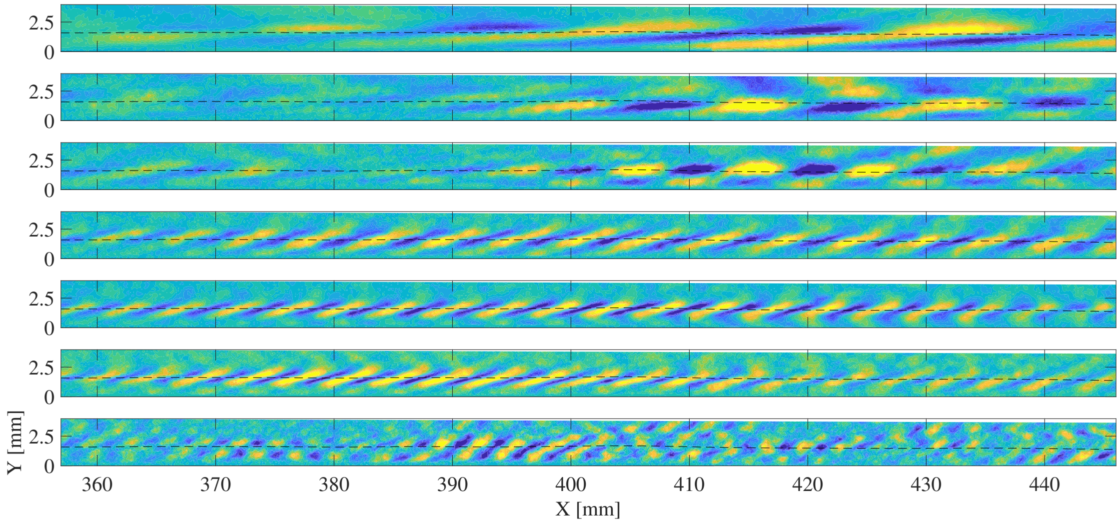

Figure 5.3: SPOD mode shapes for the +0° configuration at condition Re45 for frequencies of (top to bottom) 35 kHz, 70 kHz, 111 kHz, 204 kHz, 257 kHz, 274 kHz, and 350 kHz.

strated by the first three contours of figure 5.3, with the 35 kHz mode now visible at X=360 mm. The 70 and 111 kHz modes develop alongside the spectral broadening observed in figure 4.4 and may thus correspond to transitional structures. The second-mode SPOD contours show the expected behavior in that the dominant (257 kHz) and lower-sideband (204 kHz) frequencies amplify over much of the field of view while the upper-sideband (274 kHz) decays. A high-frequency (350 kHz) mode is illustrated in the final contour of figure 5.3. While much of the content at this frequency is likely caused by intermittent turbulence, particularly towards the edge of the field of view, a rope-like structure can be seen from X=390 − 400 mm. It is possible that this corresponds to harmonic content at 400 kHz which would be aliased by the 747 kHz framerate of this test.

Low-frequency disturbances generated at condition Re52 (figure 5.4) largely resemble those observed at condition Re45. Second-mode structures are now ob-

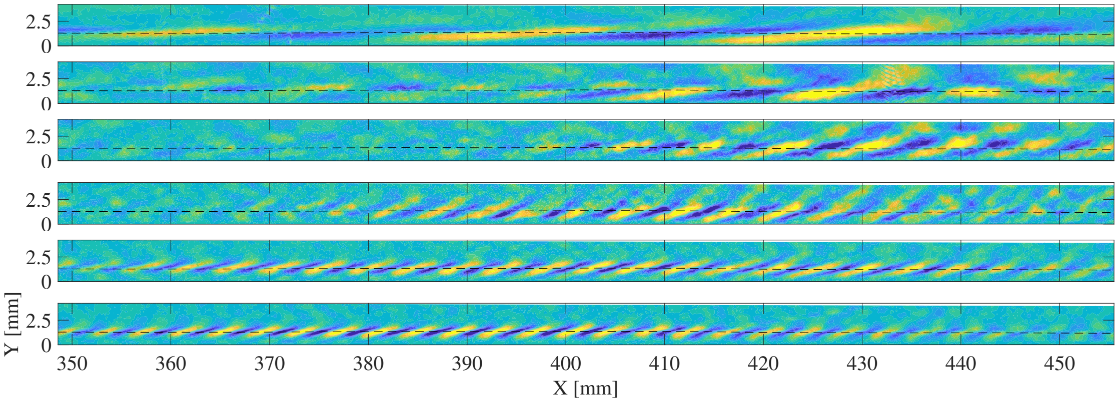

Figure 5.4: SPOD mode shapes for the +0° configuration at condition Re52 for frequencies of (top to bottom) 32 kHz, 75 kHz, 144 kHz, 235 kHz, 257 kHz, and 294 kHz.

served at higher frequencies and overpower the flickering noise. The 294 kHz mode demonstrates strong disturbances even at the upstream edge of the field of view. It is worth noting that all modal structures begin to dissipate or lose coherence downstream of X=430 mm. This is attributed to the transitional/turbulent nature of the boundary layer at such high Re_m, which degrades the coherent flow structures.

5.2 -5 ° Extension

The SPOD energy curves (see figure 5.5) again demonstrate the dominance of the second mode for this configuration. Flickering noise now manifests itself as spikes around 130 kHz which may be ignored. An interesting phenomenon is observed at condition Re45, where the second-ranked SPOD mode shows elevated energy at the upper end of the frequency range. This is likely an effect of aliasing, as second-mode structures will exist beyond the Nyquist limit of 275 kHz for this test.

Select mode shapes computed for condition Re33 are given in figure 5.6. As should be expected based on the preceding discussion, at 241 kHz a distinctly rope-

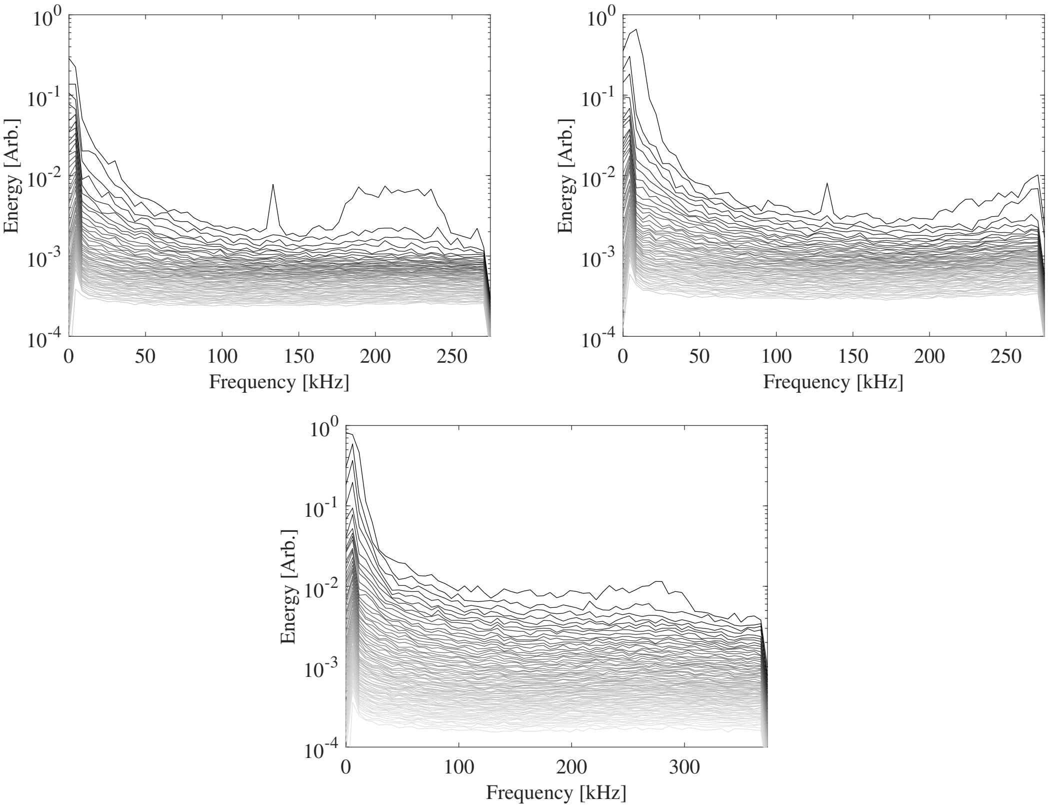

Figure 5.5: SPOD mode energy for the -5° extension at (top-left) condition Re33, (top-right) condition Re45 and (bottom) condition Re52.

like, second-mode structure is observed concentrated about the pseudo-streamline which decays downstream of the corner. The mode shape for 176 kHz possesses this same second-mode structure but instead amplifies along the cylindrical afterbody, demonstrating that the band of growth observed in figure 4.7 indeed corresponds to second-mode structures which develop at lower frequencies downstream of the corner. This is also consistent with the low-frequency shift seen at sensor D5 in figure 3.7. The 60 kHz and 90 kHz contours also correspond to bands of growth identified in the N-factor plot and seemingly are associated with coherent flow structures in the downstream part of the field of view; the origin of these features is uncertain. There also appear to be very low-frequency structures even upstream of the corner at 13 kHz.

At condition Re45, SPOD again resolves the decaying second mode, now at 258 kHz, shown in the lowermost contour of figure 5.7. This mode shape also captures the radiation of high-frequency content along the expansion wave. In contrast, the lower side-band of the second mode at 236 kHz maintains its amplitude through the expansion, decaying only weakly towards the end of the field of view. Frequency-shifted second-mode waves are seen amplifying in the 193 kHz contour, and similar behavior is noted for the 155 kHz mode shape, representing the dramatic N-factor peak in figure 4.8. In this latter case, however, the structures remain relatively indistinct, consistent with growth beginning from a weak initial state. Amplification of braided, 34 kHz structures is again observed with this configuration in the top contour of figure 5.7.

Figure 5.8 shows similar SPOD mode shapes for condition Re52. Along the

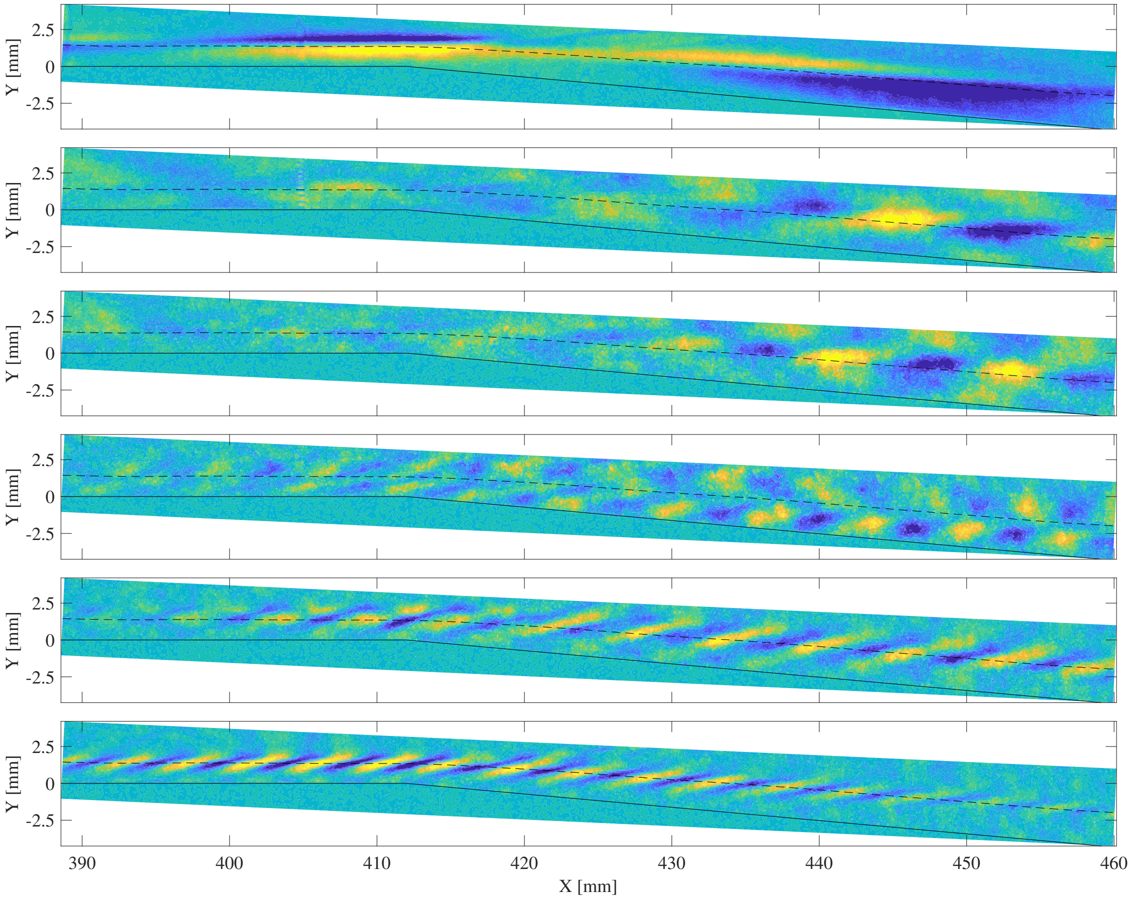

Figure 5.6: SPOD mode shapes at condition Re33 for frequencies of (top to bottom) 13 kHz, 60 kHz, 95 kHz, 163 kHz, 176 kHz, and 241 kHz.

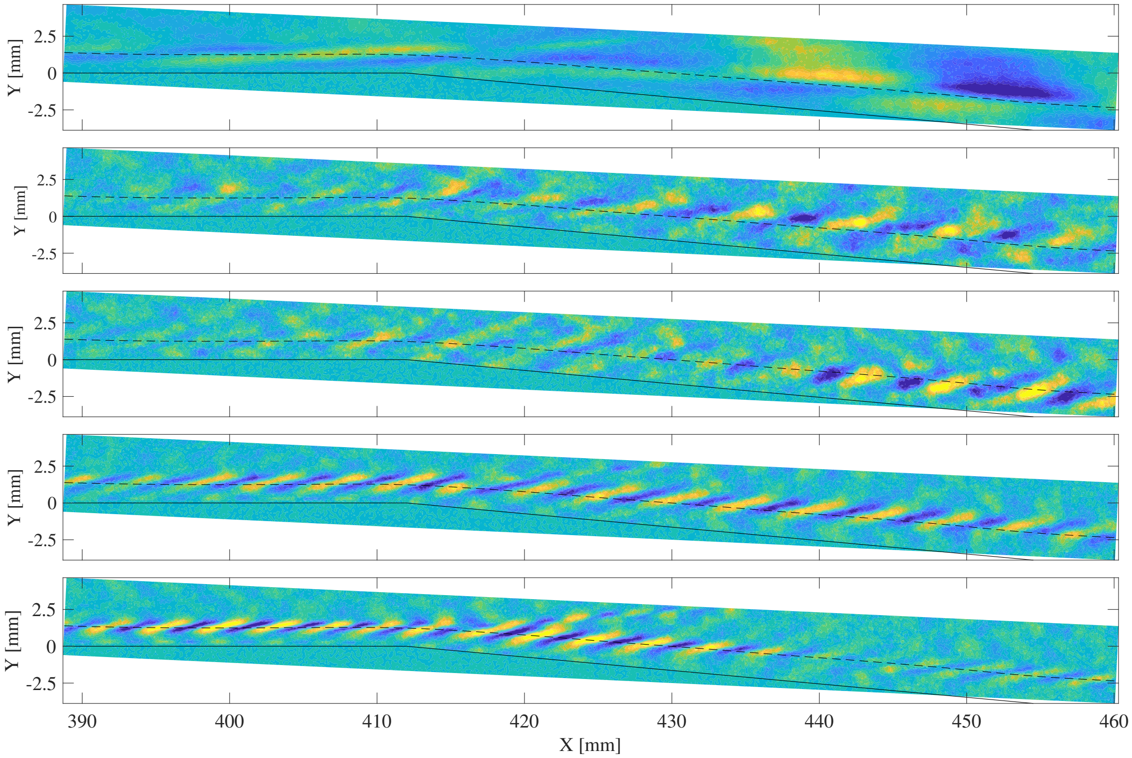

Figure 5.7: SPOD mode shapes at condition Re45 for frequencies of (top to bottom) 34 kHz, 155 kHz, 193 kHz, 236 kHz, and 258 kHz.

afterbody, decaying and amplifying rope-like structures are observed at 274 kHz and 204 kHz, respectively. Additional structures with a shallower inclination angle are observed extending out from near the wall at 117 kHz, corresponding to the N-factor peak along the afterbody, though it is unclear if these are truly new modal disturbances or merely turbulent artifacts. The high-frequency content at 344 kHz is almost certainly due to intermittent turbulence. As with condition Re45, significant content was seen to develop at very low frequencies along the pseudo-streamline (see figure 4.6). The structure of this content is exemplified by the 47 kHz mode shape in figure 5.8, though turbulence appears to be contaminating and blurring these features.

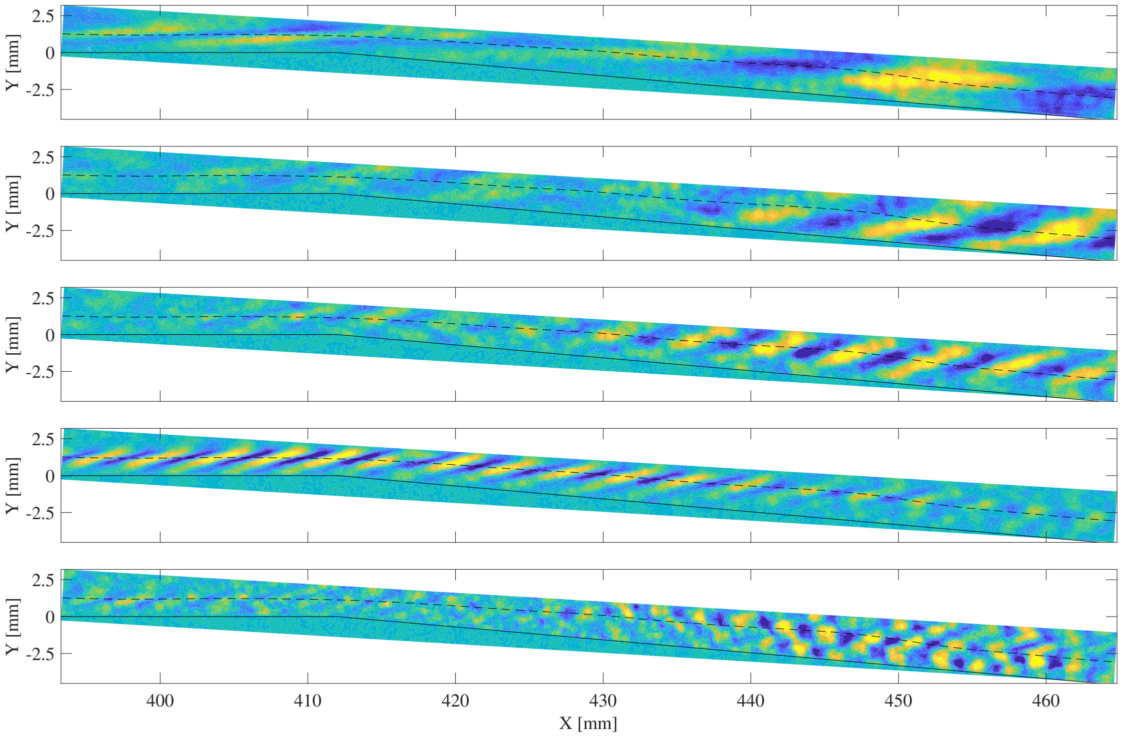

Figure 5.8: SPOD mode shapes at condition Re52 for frequencies of (top to bottom) 47 kHz, 117 kHz, 204 kHz, 274 kHz, and 344 kHz.

5.3 +5 ° Extension

The SPOD energy spectra for the +5° compression (5.9) still demonstrate distinct peaks surrounding the second-mode fundamental, but with additional regions of elevation. At condition Re33, for instance, the highest-ranked mode contains substantially more energy than the second-highest around $70 - 80$ kHz; this is also seen near 150 kHz at condition Re45. The 300 kHz peaks in these spectra again correspond to flickering noise in the schlieren system.

SPOD mode shapes computed for the +5° case at condition Re33 reveal complex growth of disturbances along the flare, as seen in the contours of figure 5.10. Second-mode content at 199 kHz can be seen in figure 5.10(g) passing through the

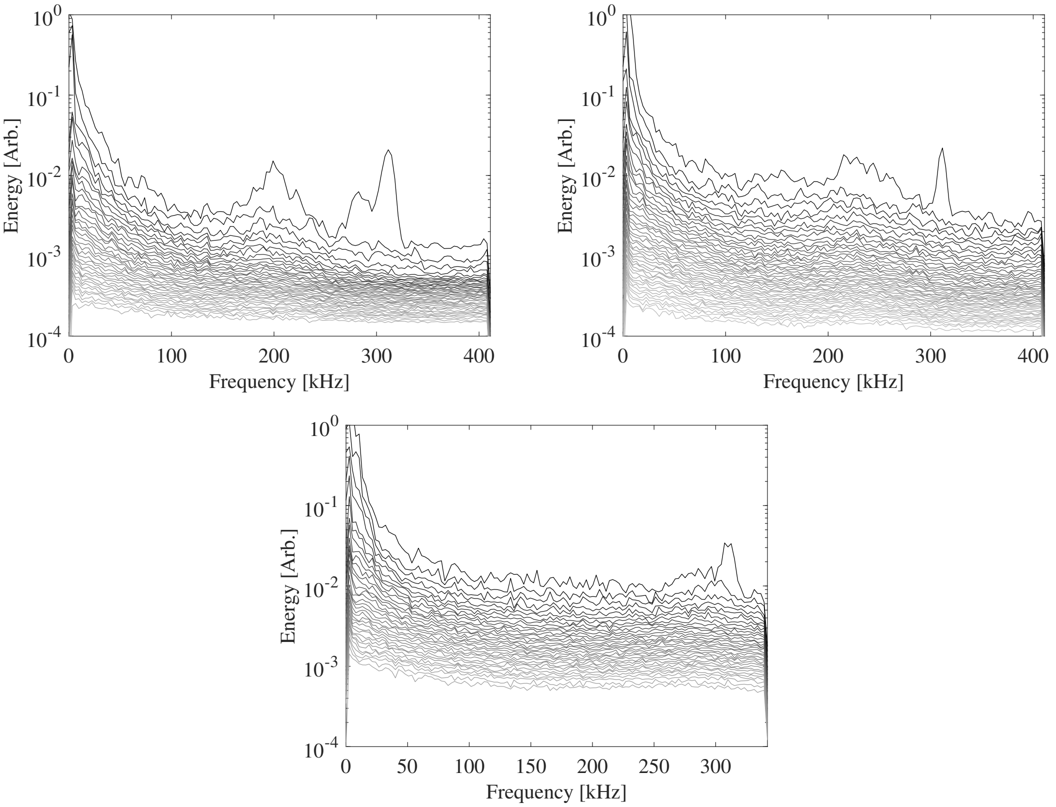

Figure 5.9: SPOD mode energy for the +5° extension at (top-left) condition Re33, (top-right) condition Re45 and (bottom) condition Re52.

corner and amplifying until approximately X=450 mm, matching the saturation point seen in the pseudo-streamline spectrum of figure 4.2. Rope-like structures can also be seen developing just downstream of the corner at 180 kHz and closer to X=440 mm at 238 kHz. The growth of low-frequency second-mode disturbances is somewhat surprising given the reduced boundary-layer thickness on the flare. The low-frequency growth identified downstream of the compression corner in chapter 4 is exemplified by the coherent structures appearing at 32 and 77 kHz around X=420 mm, both of which seemingly correspond to significant N-factor peaks along the pseudo-streamline. The 32 kHz mode has the same appearance as the braided structures observed in the bandpass-filtered sequence of figure 4.17. An additional structure appears in this region at 125 kHz (figure 5.10d), though it possesses an irregular structure. As will be discussed in chapter 6, this growth region correlates well with the appearance of nonlinear interactions, particularly for the 77 and 125 kHz structures. Additional SPOD mode shapes with nonlinear relevance are show for frequencies of 141 and 161 kHz which amplify downstream of the corner but then lose coherence towards the end of the flare. High-frequency content at 343 kHz is illustrated in the final contour of figure 5.10 with some coherent structure amplifying around X=440 mm, but may again be attributed to turbulence.

Low-frequency content is again seen to develop downstream of the corner at condition Re45 in figure 5.11. Braided structures are observed in the 35 and 61 kHz mode shapes. At 100, 151, and 177 kHz, flow features are seen developing halfway along the flare which are structurally similar to those observed in the transitional region of the undisturbed case (the second and third contours of figure 5.3). Par-

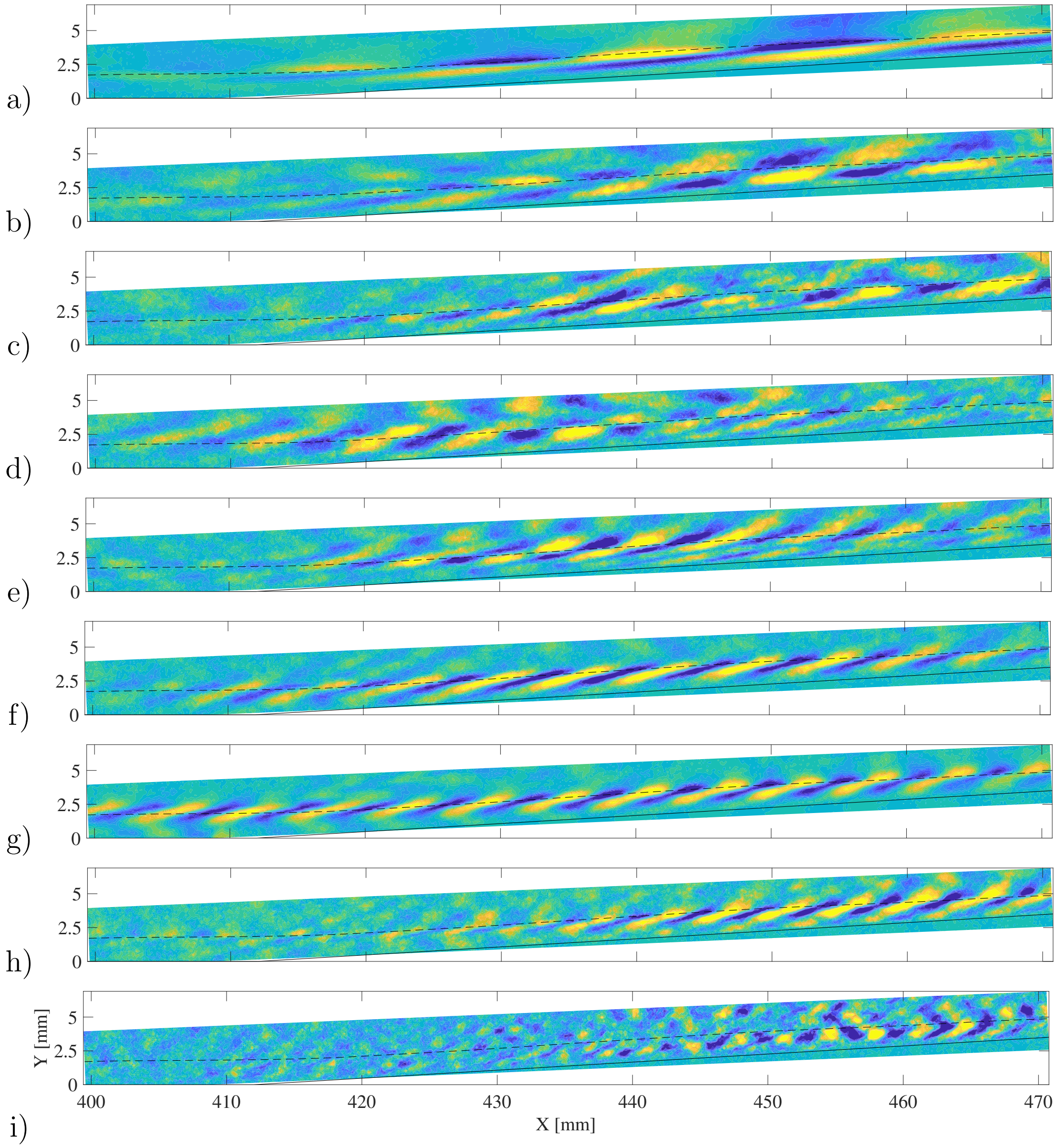

Figure 5.10: SPOD mode shapes for the +5° configuration at condition Re33 for frequencies of (a) 32 kHz, (b) 77 kHz, (c) 125 kHz, (d) 141 kHz, (e) 161 kHz, (f) 180 kHz, (g) 199 kHz, (h) 238 kHz, and (i) 343 kHz.

ticular note should be taken of the 151 kHz structure, as this corresponds to a significant N-factor peak for the test, but this appears to be largely due to a complete lack of structure upstream. The SPOD mode shapes within the second-mode band at 225 and 244 kHz show evidence of dissipation due to transition downstream of $X = 450$ mm, and energy can be seen radiating away from the boundary layer along the corner shock. At this condition, coherent structures are observed at higher frequencies of 292 and 382 kHz from around X=420 mm, which appear related to turbulent content.

The rapid transition induced by the compression corner at condition Re52 is evident in the structure of the SPOD modes shown in figure 5.12. Low frequency content appears almost out of nowhere at the corner in the 27, 61, and 136 kHz modes. These structures have the "fuzzy" appearance indicative of turbulent contamination. The lack of coherent structures along the frustum at 136 kHz is somewhat surprising given the spectral peak exhibited by the U3 PCB sensor in figure 3.11. The higher-frequency mode shapes associated with the second mode show an immediate breakdown in structure at the flare due to the turbulent nature of the boundary layer. All this is to be expected based on the immediate spectral broadening and dissapearance of the second-mode peak observed along the pseudo-streamline. The 270 kHz mode, which corresponds closely to the U3 peak second-mode frequency at this condition, does persist for a short distance downstream of the corner thanks to several wavepackets which manage to traverse the SWBLI without immediately breaking down.

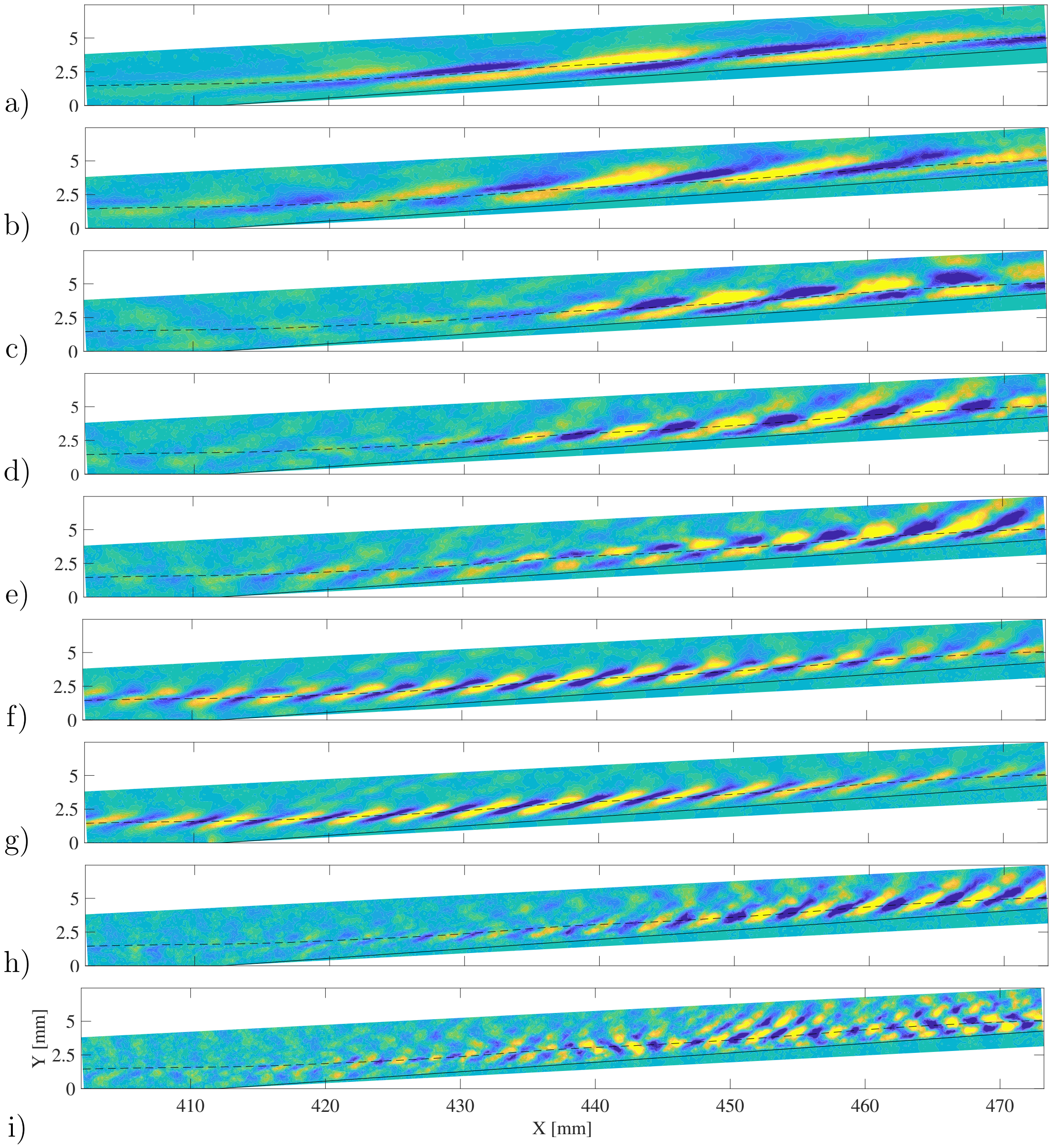

Figure 5.11: SPOD mode shapes for the +5° configuration at condition Re45 for frequencies of (a) 35 kHz, (b) 61 kHz, (c) 100 kHz, (d) 151 kHz, (e) 177 kHz, (f) 225 kHz, (g) 244 kHz, (h) 292 kHz, and (i) 382 kHz.

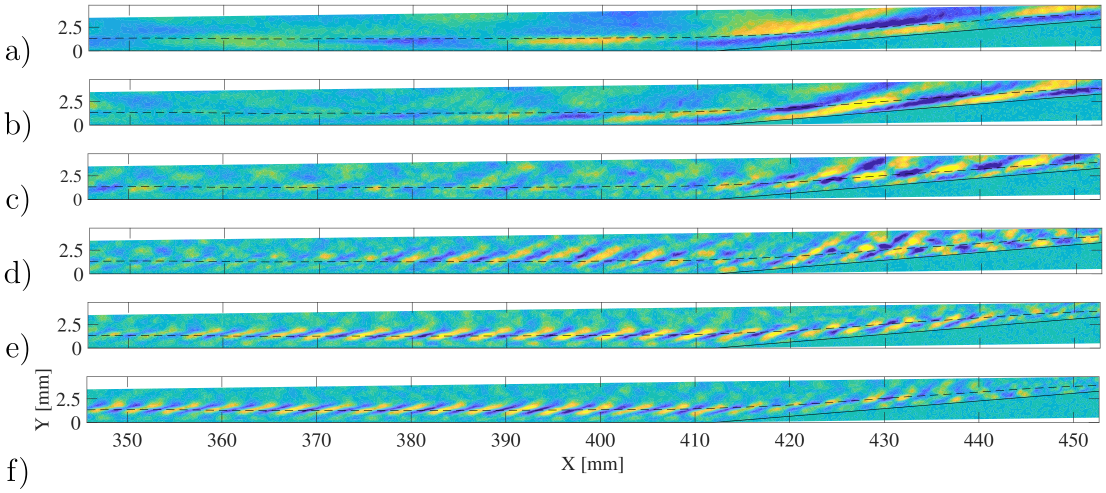

Figure 5.12: SPOD mode shapes for the +5° configuration at condition Re52 for frequencies of (a) 27 kHz, (b) 61 kHz, (c) 136 kHz, (d) 238 kHz, (e) 270 kHz, and (f) 294 kHz.

5.4 +10 ° Extension

Aside from the expected second-mode peak, the SPOD energy spectrum for condition Re33 (figure 5.13) demonstrates a distinct peak at 71 kHz, matching the expected frequency of the previously identified shear-generated instability. Note that the turbulence on the flare has swamped the energy spectrum for condition Re52 (and to a lesser extent condition Re45), causing the second-mode peak to vanish. This is a good example of why the significance of SPOD modes should not be determined entirely from the energy content, which is averaged over the entire field of view, as the presence of second-mode waves was shown in the time-resolved images and the pseudo-streamline spectra to characterize the boundary layer upstream of the corner.

Eigenvalue contours computed for 42, 71, and 215 kHz at condition Re33 are presented in figure 5.14. The second-mode waves at 215 kHz exhibit the expected

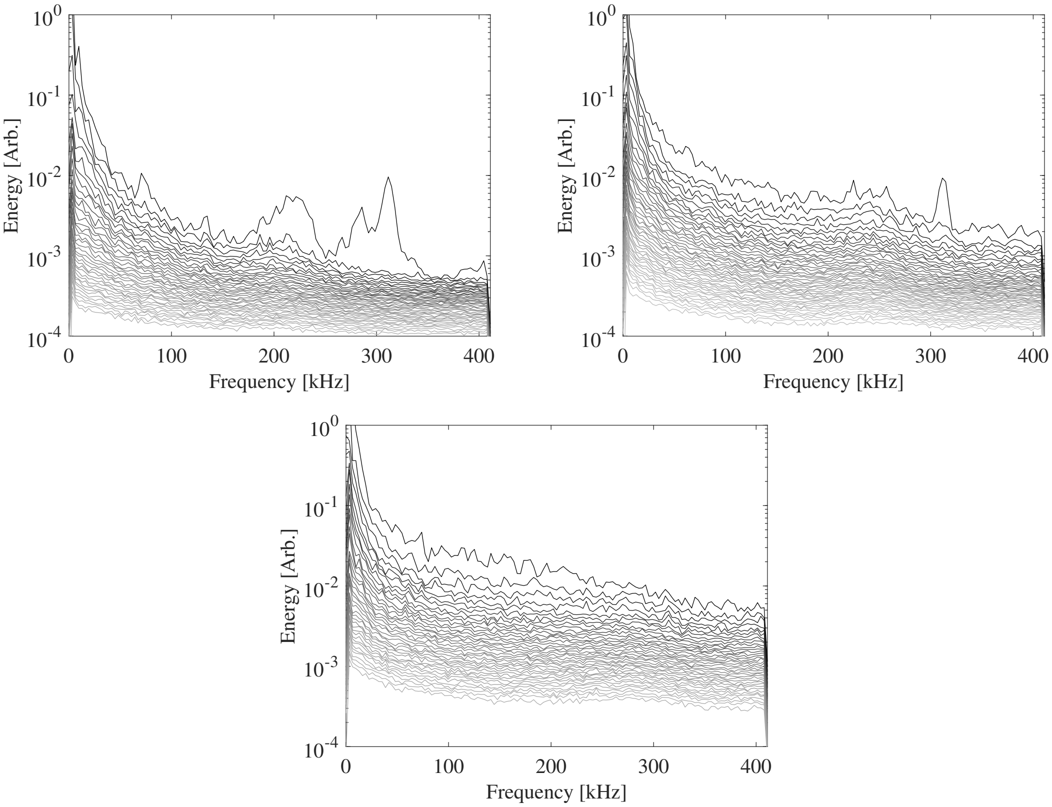

Figure 5.13: SPOD mode energy for the +10° extension at (top-left) condition Re33, (top-right) condition Re45 and (bottom) condition Re52.

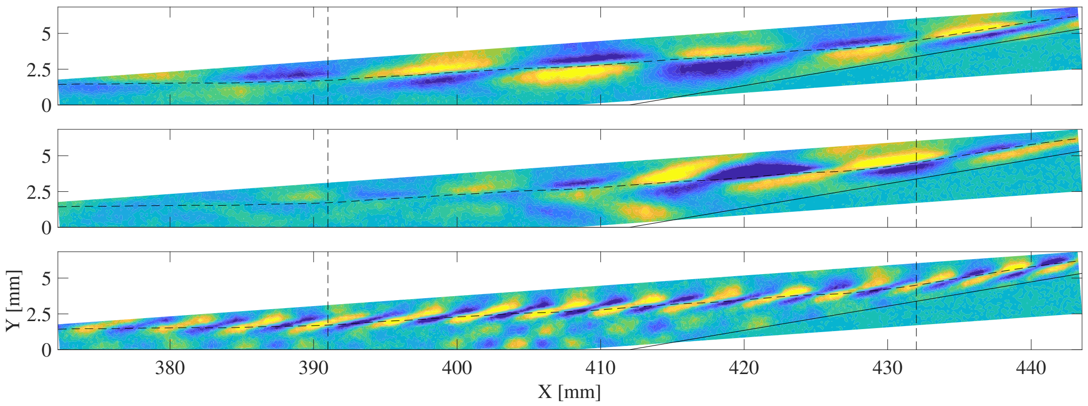

Figure 5.14: SPOD mode shapes for the +10° configuration at condition Re33 at (top to bottom) 42 kHz, 71 kHz, and 218 kHz.

rope-like structure, weakening only slightly as they traverse the corner separation with some evidence of second-mode energy passing into the separation bubble. The 71 kHz contour reveals the same braided structure forming in the separated shear layer as in the bandpass-filtered series of figure 4.16. These flow features appear to weaken slightly downstream of reattachment, as was seen along the pseudo-streamline spectra. The 42 kHz mode shape consists of similar, braided features, but they amplify significantly immediately downstream of separation and maintain amplitude through reattachment. This behavior is consistent with that of the 40 kHz N-factor peak which develops along the pseudo-streamline in figure 4.7. Although it is unclear if the separation bubble is responsible for producing these 42 kHz disturbances (which seems unlikely given the presence of similar features in the +0° configuration), it clearly serves to amplify them.

Figure 5.15 displays mode shapes for various frequencies at condition Re45, with the second-mode sidebands presented at 257 kHz and 225 kHz. Although these frequencies both lie within the second-mode range, the waves at 257 kHz begin to

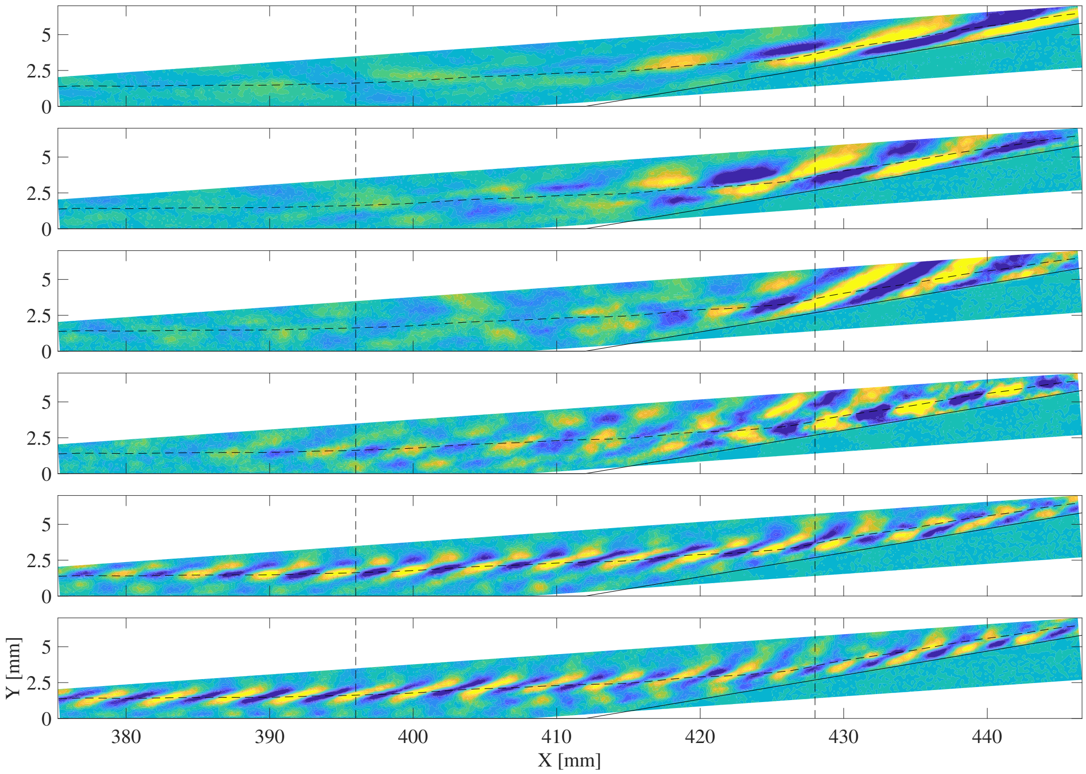

Figure 5.15: SPOD mode shapes for the +10° configuration at condition Re45 at (a) 61 kHz, (b) 83 kHz, (c) 119 kHz, (d) 164 kHz, (e) 225 kHz, and (f) 257 kHz.

decay downstream of separation while the 225 kHz content maintains its amplitude over the same region. Both frequencies then take on a modified structure downstream of reattachment. A shear-generated disturbance is visualized in the 83 kHz contour and is seen to lose its braided structure upon reattachment. This loss of structure is likely due more to transition than the natural evolution of the disturbance. Additional modes are presented at 61, 119, and 164 kHz which amplify alongside the shear-generated disturbance within the downstream portion of the separation bubble. The eigenvalue contours at 119 kHz and 164 kHz appear significantly augmented by turbulence downstream of reattachment and are included here primarily to facilitate the discussion of nonlinear interactions in the next chapter.

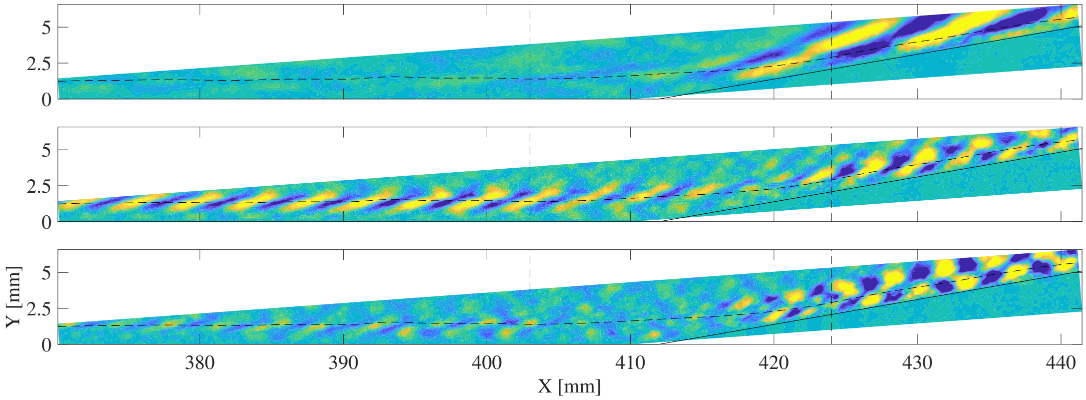

Figure 5.16: SPOD mode shapes for the +10° configuration at condition Re52 at (top to bottom) 90 kHz, 289 kHz and 318 kHz.

The middle mode shape in figure 5.16 (289 kHz) demonstrates the second-mode content is still well-resolved upstream of the corner at condition Re52, despite the lack of second-mode peak in the energy spectrum. The waves disperse upon separation before amplifying significantly at reattachment, with energy extending well away from the wall. The top contour (90 kHz) reveals no evidence of shear-generated disturbances, showing instead the dramatic growth of low-frequency content just upstream of reattachment (at $X = 420\,\mathrm{mm}$). Comparable growth is observed at this same location for frequencies above the second mode in the 318 kHz mode shape. Each one of these eigenvalue contours is consistent with the immediate transition of the boundary layer on the flare.

5.5 +15 ° Extension

As evidenced by the streamline spectra of figures 4.2 and 4.4, the large separation bubble created by the +15° configuration results in significant content under 70 kHz but little-to-no high frequency content for conditions Re33 and Re45. This is

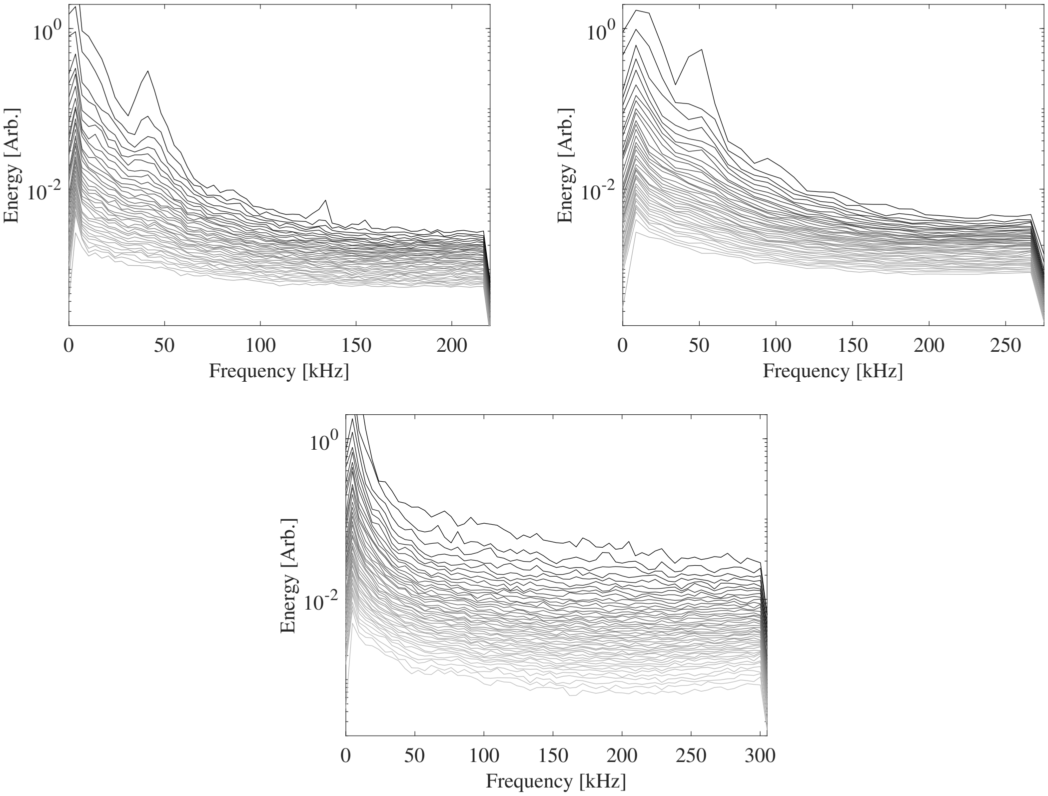

Figure 5.17: SPOD mode energy for the +15° extension at (top-left) condition Re33, (top-right) condition Re45 and (bottom) condition Re52.

reflected in the SPOD energy spectra, where the dominant peak at these conditions now corresponds to the shear-generated disturbances around $40-50\,$kHz and there is no hint of a second-mode peak at any condition. The highest-rank modes are also elevated slightly around $80-90\,$kHz. The condition Re33 peak at 130 kHz is a flickering mode.

The SPOD mode shapes presented in figure 5.18 showcase the structure of the shear-generated disturbances at condition Re33. The 41 kHz mode closely resembles the shear-generated disturbance identified for the +10° configuration and appears strongest just upstream of reattachment from X=$420-430\,$mm. The 48 and 58 kHz modes both develop further upstream within the separation region and

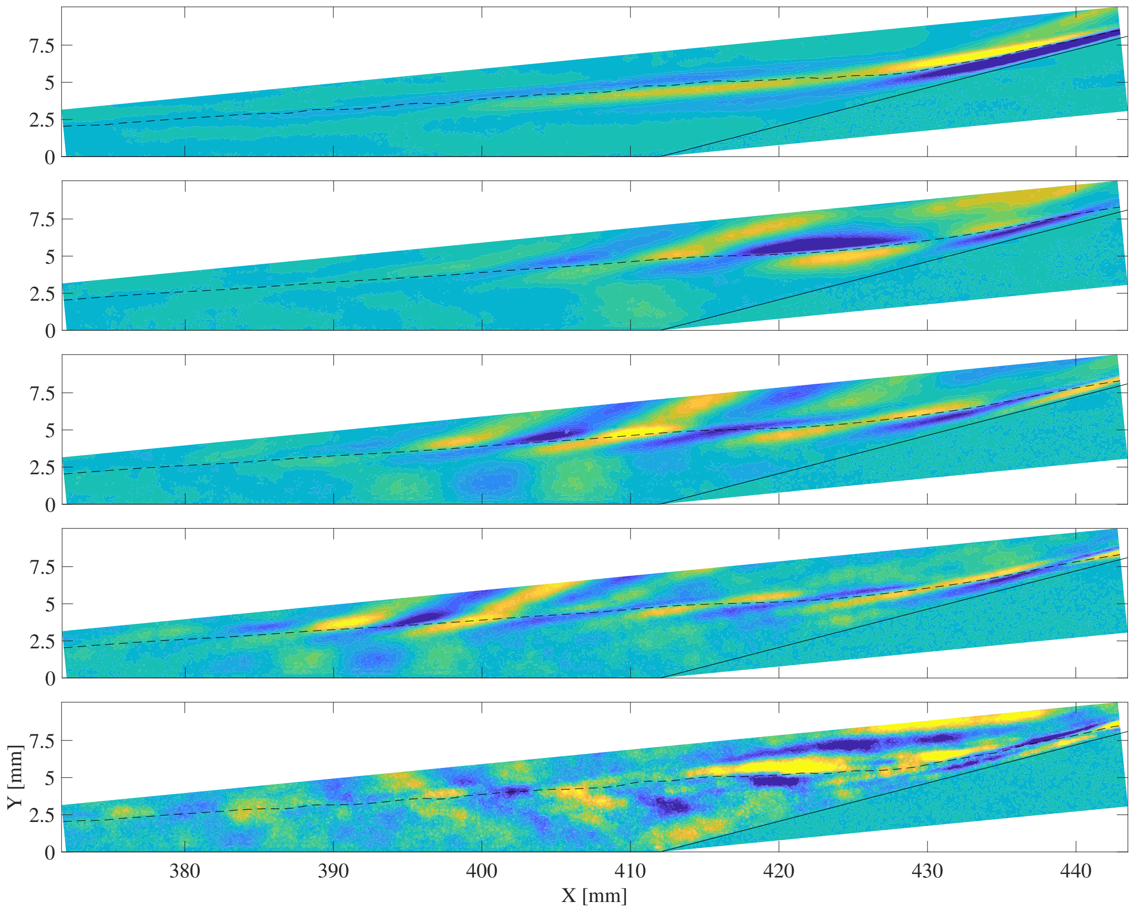

Figure 5.18: SPOD mode shapes for the +15° configuration at condition Re33 for frequencies of (top to bottom) 14 kHz, 41 kHz, 48 kHz, 58 kHz, 83 kHz.

radiate energy away from the shear layer. Significant energy is also seen in the 83 kHz mode as the separation region compresses, appearing as longitudinal streaks emanating from the boundary layer at X=420 mm. It is notable that this corresponds approximately to the harmonic frequency of the shear-generated disturbances. Very low-frequency (14 kHz), braided structures are observed amplifying rapidly in the immediate vicinity of reattachment in the uppermost contour of figure 5.18. These features likely correspond to the lower band of the N-factor peak in figure 4.7.

The +15° configuration is still largely characterized by low-frequency modal structures at condition Re45, which are illustrated by figure 5.19. The first SPOD contour, computed at 26 kHz, is concentrated around the downstream end of the separation bubble with a different structure than the 14 kHz mode from condition Re33. Notably, this is approximately the subharmonic of the shear-mode, which will be discussed further in chapter 6. The modal structure at 47 kHz matches the expected braided structure of the shear-generated disturbance and again amplifies starting directly above the cone/flare junction, while the 60 kHz mode shows content developing further upstream with significant radiation away from the shear layer. Modal content at 99 and 146 kHz is comprised almost entirely of radiation along the compression waves ahead of reattachment and it is notable that these frequencies correspond closely to the first and second harmonics of the shear-generated disturbances. The potential nonlinear development of these structures will be studied further in the next chapter. High-frequency (223 kHz) features are observed downstream of reattachment within the severely thinned boundary layer in the lowermost contour of figure 5.19.

Figure 5.20 shows only two mode shapes computed at condition Re52. As with the +10° configuration, there is little evidence of shear-generated disturbances as this condition, demonstrated by the 62 kHz contour. This contour does, however, show substantial amplification of turbulent structures along the flare. Second-mode structures are captured upstream of separation by the 286 kHz mode, but these quickly break down within the separation region and appear as turbulent structures along the flare.

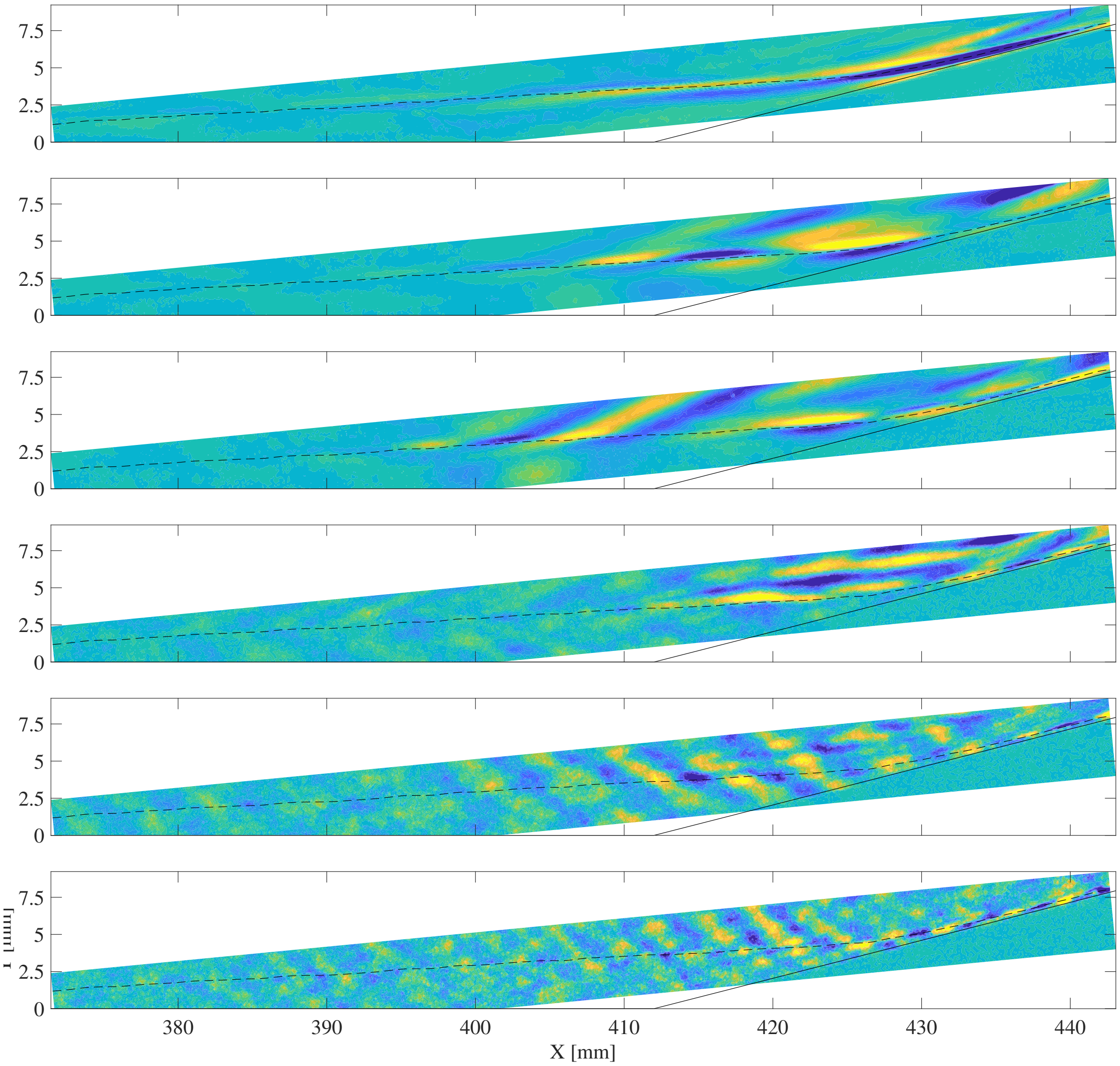

Figure 5.19: SPOD mode shapes for the +15° configuration at condition Re45 for frequencies of (top to bottom) 26 kHz, 47 kHz, 60 kHz, 99 kHz, 146 kHz, and 223 kHz.

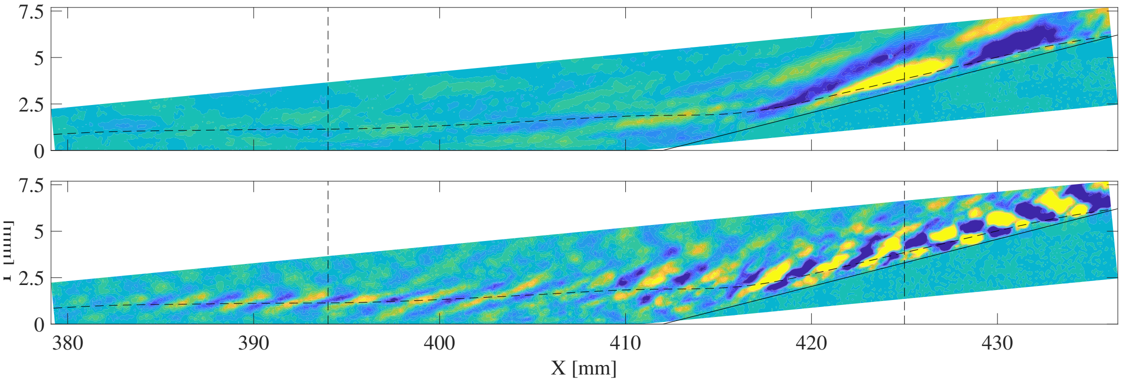

Figure 5.20: SPOD mode shapes for the +15° configuration at condition Re52 for frequencies of (top) 62 kHz and (bottom) 286 kHz.

5.6 Propagation Speeds

Although the disturbance propagation speed is not required for spectral analysis in the present work, it is still an important disturbance property and is of interest for comparing to computations. In this section we present two methods for determining the propagation speeds, U_p, of the bounday-layer disturbances: one based on the SPOD analysis and another, more conventional technique for comparison. The conventional formulation, referred to as the correlation method, is related to the technique employed in refs. [13], [14], and [15], but relies upon the pixel-intensity time series rather than spatially distributed data, and thus allows for improved spatial resolution. First, for a given test, the time series are bandpass-filtered around the second-mode frequency. For each streamwise station, we compute the cross-correlation coefficient between the station of interest and each downstream pixel assuming time lags of 1, 2 and 3 frames. The streamwise shift which produces the maximum cross-correlation is identified and a second-order polynomial is fit to the correlation coefficients of the "optimal" streamwise shift and the two neighboring pixels in order to determine the location of the peak shift with sub-pixel accuracy. This process is repeated backwards in time (by computing the cross-correlation with upstream pixels) and the results are averaged at each station, yielding propagation speeds which are central-differenced in space. On average, the structures traverse approximately 18 pixels between frames, which could result in substantial structural modulation and poor correlation, particularly in the vicinity of the corner.

The second method is based upon the SPOD modes and provides propagation speeds that vary with both streamwise location and frequency. For each frequency in the highest-ranked SPOD mode, the real component of the mode shape is extracted along the pseudo-streamline. Spatial power spectra are then computed along the streamline using a sliding window of 128 pixels, allowing the dominant wavelength, λ, to be identified at each station. For frequency f_i, the propagation speed can then be computed according to

$$U_{p,i} = f_i \times \lambda(f_i). \tag{5.1}$$

Sample results obtained using the SPOD method are given for each configuration at condition Re33 in figure 5.21. This method demonstrates poor performance outside of the second-mode range, giving unrealistically high or low propagation speeds. This is attributed largely to the lack of coherent flow structures at these frequencies, but is exacerbated by the fact that the pseudo-streamlines were tailored to the propagation trajectories of high-frequency, second-mode disturbances which may not be appropriate for other disturbances. It is likely for the latter reason that the shear-generated disturbances do not appear for the separated configurations. This could potentially be addressed by averaging the spatial spectrum in the pseudo-streamline-normal direction. Note that unphysical results are obtained even within the second-mode range for the +15° configuration because of the lack of wavepackets.

A comparison of the two methodologies is provided for each condition in figure 5.22 with the expansion configuration in the left column and the +0° extension in the right column. The second-mode propagation speed for the SPOD method

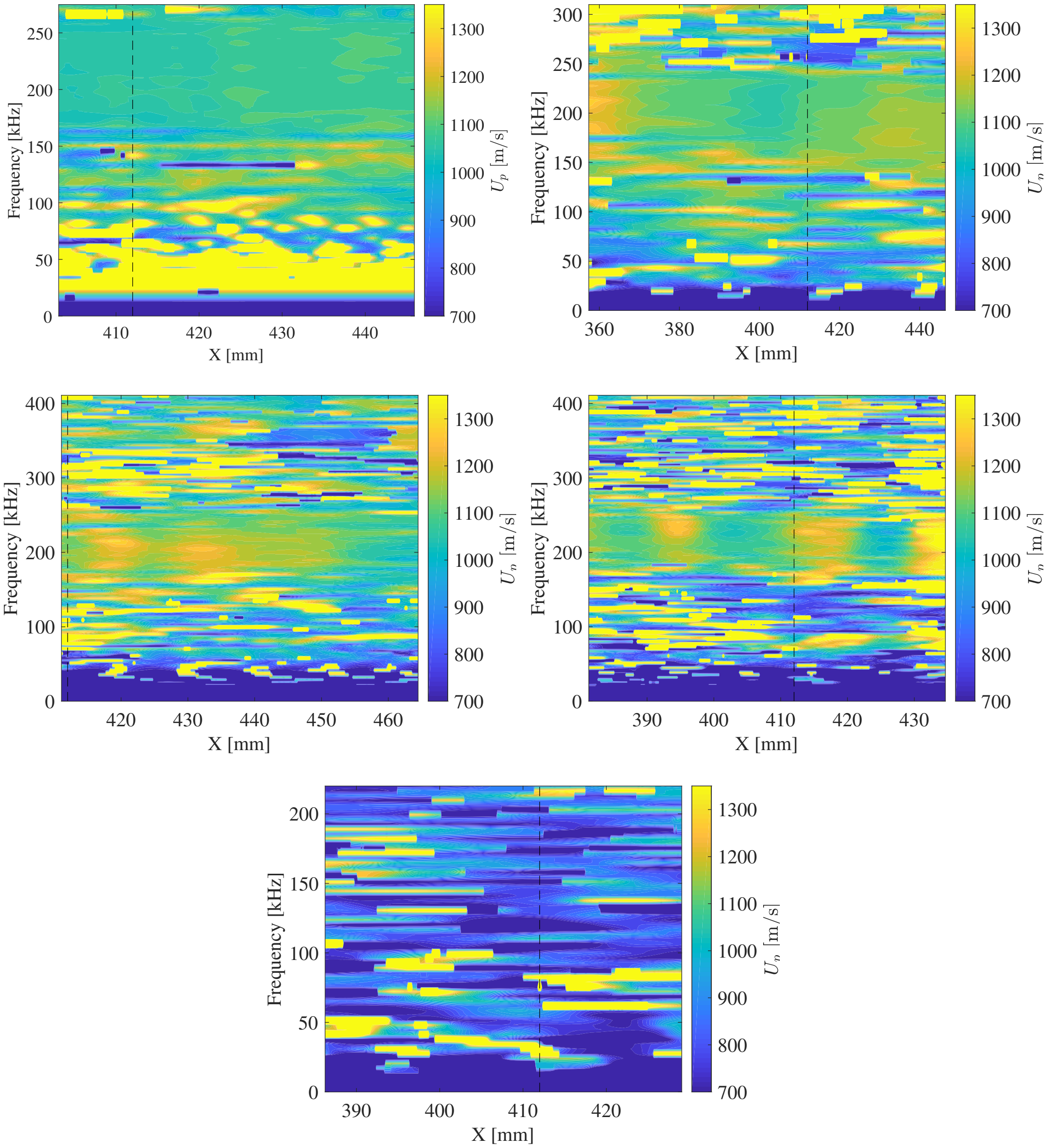

Figure 5.21: Propagation speeds computed at condition Re33 using the SPOD-based methodology; (top-left) -5° configuration, (top-right) +0° configuration, (middle-left) +5° configuration, (middle-right) +10° configuration, and (bottom) +15° configuration.

is calculated here by averaging over the second-mode frequency range. The average speeds computed upstream and downstream of the corner using the correlation method are included as dashed lines and are also provided in table 5.2 together with theoretically determined edge velocities. The latter were determined from the Taylor-Maccoll solution, which, for the downstream region on the expansion configuration, was passed through a Prandtl-Meyer expansion fan (the resulting value will be appropriate immediately downstream of the corner and will subsequently relax towards the freestream velocity). Note that the downstream average for condition Re52 (for the -5° extension) was terminated at $X = 440\,\mathrm{mm}$ due to the anomalous drop in propagation speed caused by a loss of coherence.

As expected, the propagation speeds remain approximately constant over the cone surface for the undisturbed boundary layer, with good agreement between the two methodologies. The correlation method demonstrates several anomalous drops and spikes, but the SPOD method behaves poorly far upstream at condition Re33, producing unphysically high values. This is likely caused by poor resolution of the second-mode disturbances within this region of the field of view, which can be seen in figure 5.2. Both methods show the propagation speed of the second-mode disturbances increases modestly through the expansion, though the normalized value, U_p/U_e, remains approximately constant due to the acceleration of the mean flow. The two methodologies demonstrate good agreement for conditions Re33 and Re45, but deviate significantly at Re52. This is likely caused by turbulent contamination, which may obscure the correlation between pixel stations but seems to have less impact on the well-resolved flow structures computed by SPOD. Thus, the SPOD

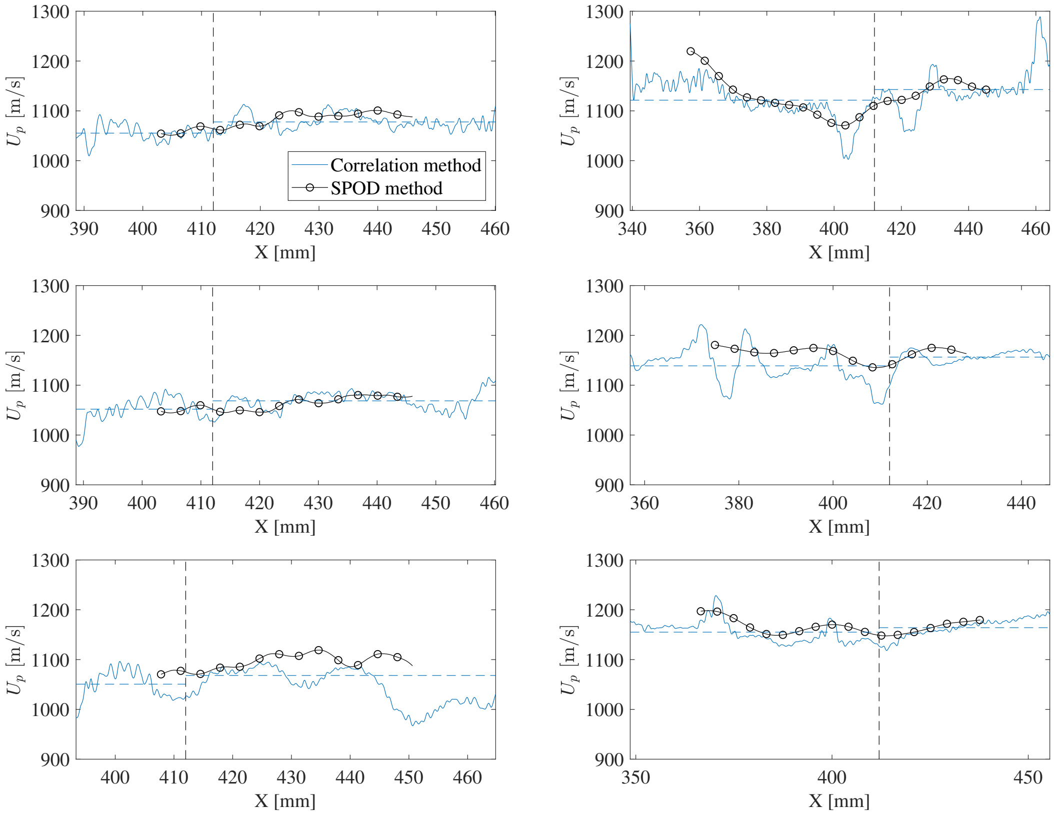

Figure 5.22: Propagation speeds computed along pseudo-streamline for the (left) -5° and (right) +0° configurations: (top) condition Re33, (middle) condition Re45, and (bottom) condition Re52.

methodology appears more robust in determining propagation speeds for weakly disturbed boundary layers, but at the expense of reduced spatial resolution. It is worth noting that the upstream propagation speeds differ between the two configurations by approximately 10%, though they lie within the range of speeds observed previously within HyperTERP by Hameed et al. [43] using FLDI.

Results for the +5° (left) and +10° (right) compression-corners are shown in figure 5.23. The +5° configuration causes a clear deceleration of the disturbances downstream of the corner, with the mean propagation speed dropping by 3% at condition Re52. Unfortunately, there is insufficient upstream information for condi-

	-5° Extension			+0° Extension		
	Re33	Re45	Re52	Re33	Re45	Re52
Upstream U_p [m/s]	1055	1052	1051	1121	1139	1155
Upstream U_e [m/s]	1255	1255	1255	1255	1255	1255
Upstream U_p/U_e	0.84	0.84	0.84	0.90	0.91	0.92
Downstream U_p [m/s]	1078	1069	1068	1143	1157	1165
Downtream U_e [m/s]	1274	1274	1274	1255	1255	1255
Downstream U_p/U_e	0.85	0.84	0.84	0.91	0.93	0.93

Table 5.2: Upstream and downstream propagation speeds computed with the correlation method.

tons Re33 and Re45 to quantify the deceleration for these tests with any confidence. Oddly, the SPOD method computes propagation speeds at condition Re33 which trace along the top of the localized jumps which occur with correlation method. Overall, the separated case creates results that are more difficult to interpret, with the propagation speeds varying substantially using both methods. The SPOD method performs particularly poorly in the vicinity of separation and reattachment, displaying large spikes in the propagation speeds. That said, the results consistently demonstrate substantial deceleration just upstream of reattachment.

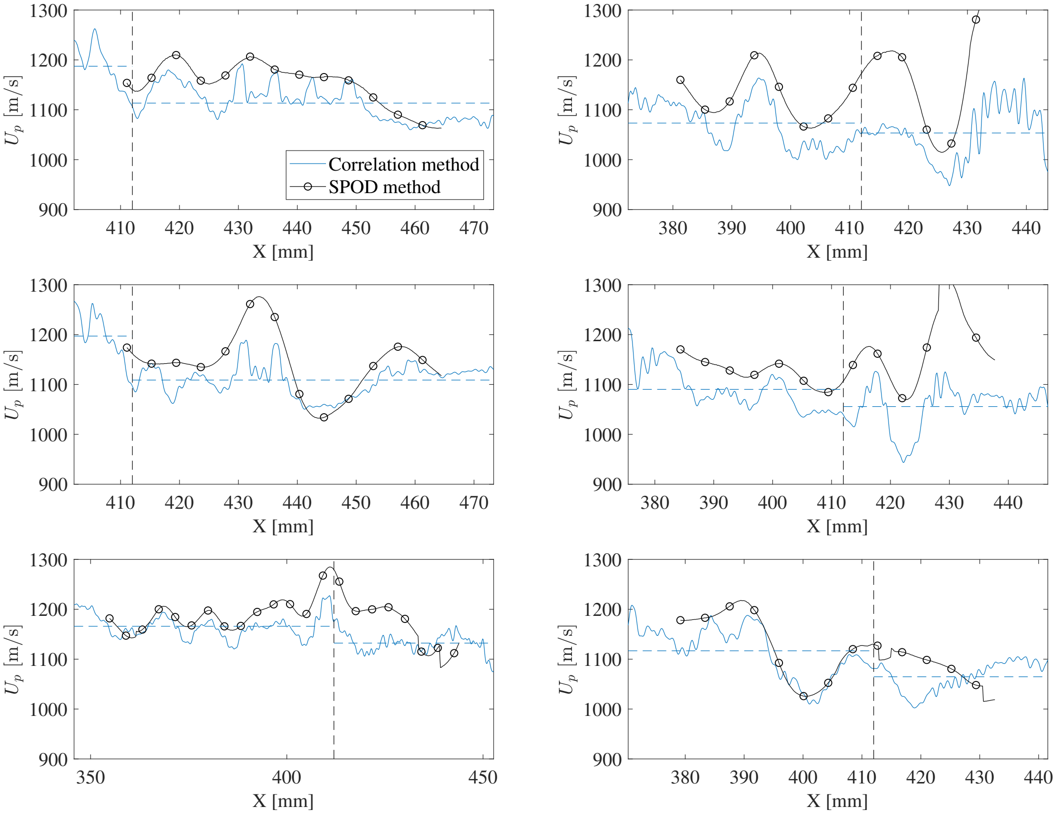

Figure 5.23: Propagation speeds computed along pseudo-streamline for the (left) +5° and (right) +10° configurations: (top) condition Re33, (middle) condition Re45, and (bottom) condition Re52.

Chapter 6: Bispectral Analysis

The high framerate employed throughout this work also facilitates the use of higher-order spectral techniques such as bispectral analysis. Computation of the normalized bispectrum, or bicoherence, allows one to identify the primary nonlinear growth mechanisms at work. More accurately, the bicoherence provides a measure of the degree of Quadratic Phase Coupling (QPC) present between three frequencies f_1, f_2 and $f_1 + f_2$. The bispectrum for a frequency triplet is defined by

$$B(f_1, f_2) = E[X(f_1)X(f_2)X(f_1 + f_2)^*], \tag{6.1}$$

where E is the expectation operator, and $X(f)$ refers to the Fourier transform component at frequency f for the time series of interest. The squared bicoherence is computed as

$$|b(f_1, f_2)|^2 = \frac{|B(f_1, f_2)|^2}{S(f_1)S(f_2)S(f_1 + f_2)}, \tag{6.2}$$

which utilizes the normalization method of Brillinger [44] where $S(f)$ is the PSD at frequency f. There is some disagreement in the literature as to the proper normalization method for bispectral analysis, with some researchers (e.g., refs. [45] and [3]) opting for the definition given by Kim and Powers [46]. The Kim and Powers method of normalization, however, has received scrutiny from ref. [47] for "artificially" bounding the result between 0 and 1 and in some cases destroys evidence of nonlinearity within experimental datasets. In the context of the present work, the Kim and Powers normalization has been found to ruin the symmetries inherent to the bispectrum and reduce the prominence of expected resonant interactions. There also exists precedent for the use of the Brillinger normalization for boundary-layer transition studies, its having been applied previously by Chokani [4] and Chokani et al. [48]. Welch's method was employed for these computations using windows of width 64.

Before exploring results from the present data set, additional background on bispectral analysis and its application to boundary-layer transition is presented. The bicoherence spectra is defined by two triangular regions, illustrated in figure 6.1, which will be referred to as the inner-triangle (IT) and the outer-triangle (OT). The inner-triangle is defined by the vertices [0,0], $[\frac{F_s}{4},\frac{F_s}{4}]$, $[\frac{F_s}{2},0]$ while the outer-triangle is defined by $[\frac{F_s}{4},\frac{F_s}{4}]$, $[\frac{F_s}{2},0]$, $[\frac{F_s}{3},\frac{F_s}{3}]$. Any information outside of this region is a redundant reflection. The outer-triangle is distinct in that it is non-redundant but relies upon aliased information, i.e., for any frequency pair $[f_1,f_2]$ within OT, $f_1 + f_2$ will lie above the Nyquist sampling frequency of the signal. Information within this region thus requires special scrutiny. A particularly useful observation is that any signal which lies upon the right edge of OT at some frequency f_1 may also correspond to a reflection of the resonant interact at $[f_1,f_1]$. To demonstrate this, let us consider the point $[\frac{5F_s}{12},\frac{F_s}{6}]$ which is located on this edge. The resonant frequency in this case would be $5F_s/6$, which aliases down to $F_s/6$. It is also worth emphasizing

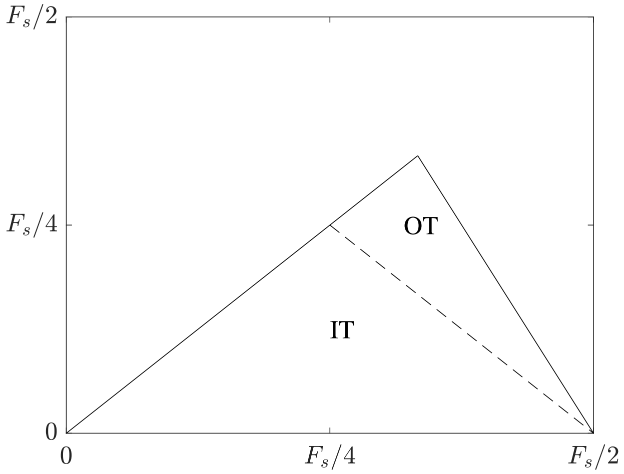

Figure 6.1: Illustration of frequency domain for bicoherence spectra.

that bispectral analysis is incapable of distinguishing between sum and difference interactions and thus some physical intuition is required for proper interpretation of the results. As will be shown, SPOD modes are particularly useful in developing this intuition.

Bispectral analysis was first applied to the study of high-speed boundary-layer transition by Kimmel and Kendall [3] to study nonlinear interactions involving second-mode disturbances. The data was obtained using hot-wire anemometry for the Mach 7.95 tests described by Stetson et al. [10] on a 7° half-angle cone. The bicoherence spectrum observed at a single streamwise station for these experiments is shown in the left plot of figure 6.2. They observed strong phase-coupling between the fundamental second-mode frequency (approximately 88 kHz) and the first harmonic, indicated by region (a). This led to their conclusion that the harmonic was developed through self-resonance of the fundamental. A weak peak is also observed in region (b), attributed to an interaction between the fundamental and the

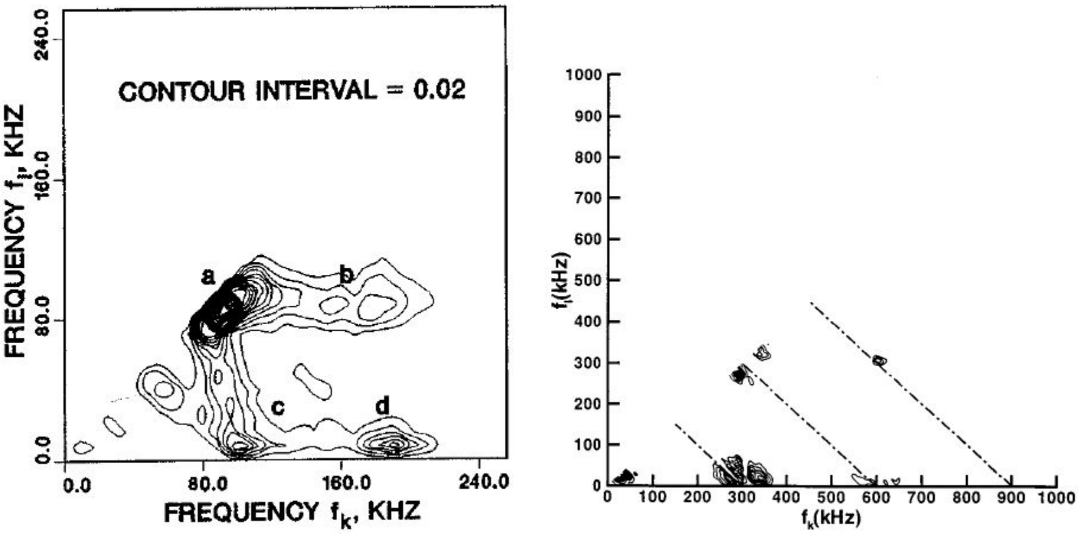

Figure 6.2: Bicoherence spectrum for a single streamwise station taken from (left) Kimmel and Kendall [3] and (right) Chokani [4].

first harmonic to produce a second harmonic. Regions (c) and (d) correspond to coupling between low-frequency content and the fundamental and first harmonic, respectively. Kimmel and Kendall conclude that low-frequency structures modulate the second-mode content and transfer energy to the sidebands.

Similar interactions were observed by Chokani [4] for hot-wire measurements obtained on a flared cone model in the NASA LaRC Mach 6 quiet facility. First and second harmonics were observed at upstream stations as a result of fundamental resonance (now at 300 kHz) and sum interactions between the fundamental and the first harmonic, illustrated by figure 6.2. Coupling was again seen between low frequencies and the fundamental sidebands, and was characterized as low-frequency modulation of the high-frequency fundamental and harmonics. These low-frequency interactions became dominant immediately preceding breakdown of the laminar boundary layer. In addition to these fundamental resonance interactions, Shiplyuk et al. [49] first observed potential subharmonic resonance within the boundary layer over a 7° cone at Mach 5.95, again using hot-wire anemometry.

6.1 $+0^\circ$ Extension

We begin by examining the bicoherence spectra observed in the $+0^\circ$ configuration to discern the undisturbed nonlinear behavior of the wavepackets. Representative bicoherence spectra for condition Re33 are shown in figure 6.3 for three distinct streamwise stations, annotated with red lines in the top meanflow image. Each of these regions corresponds to 21 pixels located along the pseudo-streamline. Well upstream of the corner, the dominant nonlinear interaction is fundamental resonance at 210 kHz, as expected based on prior literature. This resonance shifts to lower frequencies downstream to match the fundamental second-mode peak frequency.

Early on the extension, illustrated by the middle contour plot of figure 6.3, the bicoherence spectrum reaches elevated levels around $[f_1, f_2] = [165\,\text{kHz}, 30\,\text{kHz}]$. Such peaks which occur in the vicinity of the second mode and involve low frequencies are typically attributed to sideband interactions, though it is potentially significant that 30 kHz roughly corresponds to the braided structures observed in the SPOD analysis. The final contour of figure 6.3 demonstrates that these resonant and sideband interactions persist far along the extension, where the instantaneous images have show that the boundary layer tends to be only intermittently transitional.

We may better visualize the spatial development of these interactions as in figure 6.4, which shows the rms bicoherence that has been computed within two select regions of the frequency plane (annotated in figure 6.3 with dashed boxes) for each pixel within the field of view. The bottom image corresponds to fundamental resonance, and we see the interaction is largely concentrated along the pseudo-streamline and amplifies along the frustum. The energy signature of this interaction begins to disperse slightly over the extension where the boundary-layer is intermittently transitional, but maintains its presence until the end of the field of view. Note that the resonant peak shifts to frequencies too low to be captured by this contour far downstream. The top image of figure 6.4 illustrates the spatial distribution of the low-frequency coupling, which appears to be concentrated along the boundary-layer edge and only appears along the pseudo-streamline at approximately $X = 415\,\mathrm{mm}$. This concentration above the pseudo-streamline matches the peak intensity of the structures seen in the top SPOD contour of figure 5.2.

At condition Re45, fundamental resonance (at approximately 260 kHz) remains the primary interaction of note far upstream, as seen in the first contour of figure 6.5. However, spectra for the downstream regions demonstrate a reduction in fundamental resonance and, at the furthest downstream location, there are no relevant peaks in the bicoherence spectrum; the boundary layer at this location is no longer well-described by modal interactions. The spatial development of fundamental resonance is illustrated in figure 6.6 where the interaction appears along the pseudo-streamline until approximately $X = 400\,\mathrm{mm}$ and again around $X = 430\,\mathrm{mm}$. Oddly, the interaction mimics the appearance of second-mode wavepackets; this may be because the interaction is resolved near the upper vertex of OT in the bicoherence spectra. Due to aliasing, this vertex corresponds to QPC between the triplet $[\frac{1}{3}f_s, \frac{1}{3}f_s, \frac{1}{3}f_s]$.

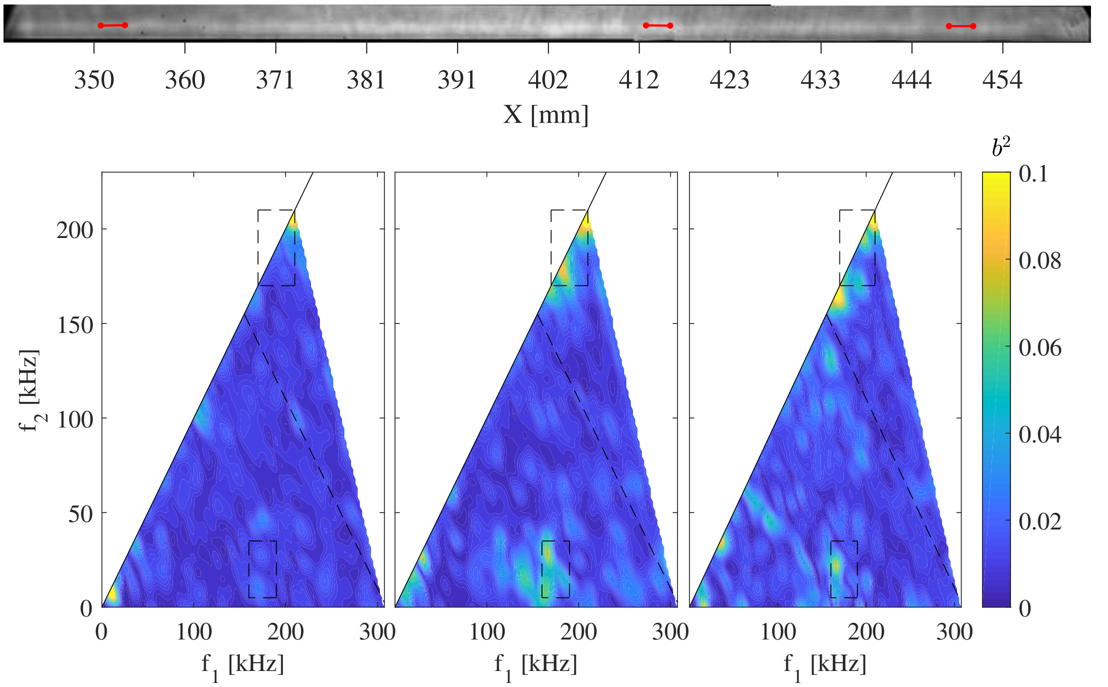

Figure 6.3: (Top) Time-averaged, flow-on image for the +0° configuration at condition Re33 with red circles denoting distinct regions for computing the bicoherence. (Bottom) Bicoherence spectra for each annotated region with the contours ordered stream-wise from left to right.

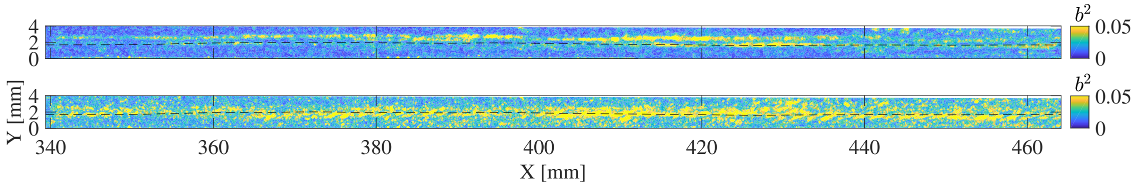

Figure 6.4: Spatial bicoherence contours at condition Re33 for frequency triplets of (top) [175,20,195], and (bottom) [190,190,380].

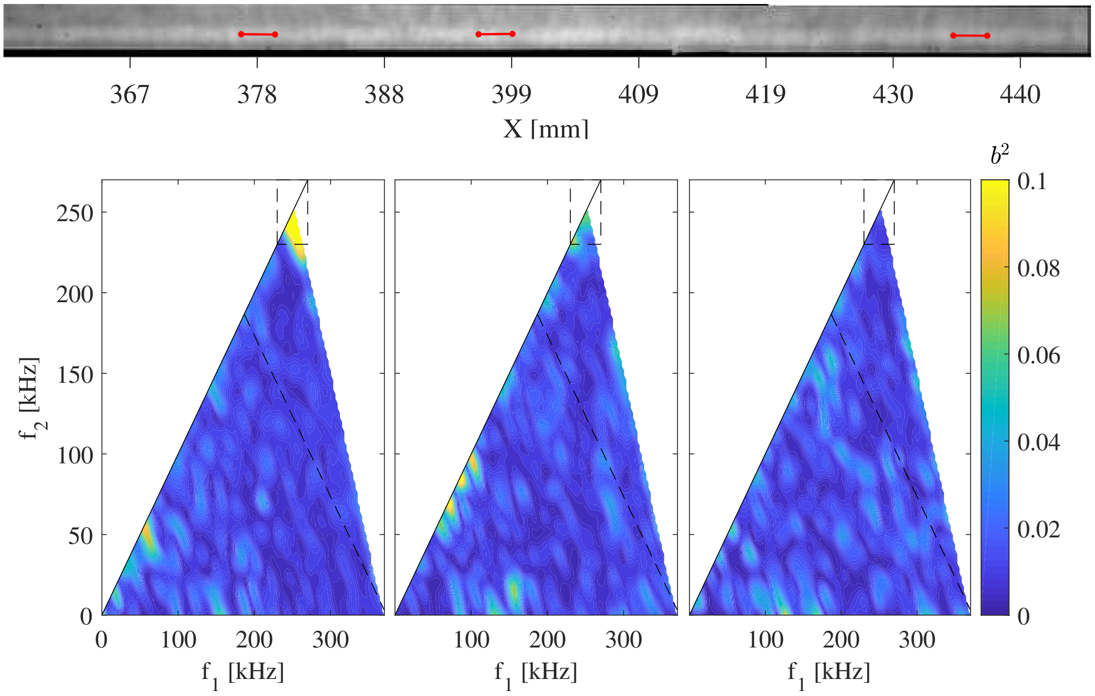

Figure 6.5: (Top) Time-averaged, flow-on image for the +0° configuration at condition Re45 with red circles denoting distinct regions for computing the bicoherence. (Bottom) Bicoherence spectra for each annotated region with the contours ordered stream-wise from left to right.

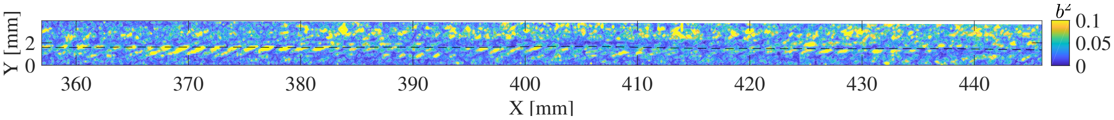

Figure 6.6: Spatial bicoherence contours at condition Re45 for the frequency triplet [250,250,500].

The lower-frequency resonance which appears around $80 - 100\,$kHz has little spatial coherence and is believed to be unphysical. Note that the turbulent nature of the downstream boundary layer at condition Re52 results in bicoherence spectra dominated by noise and thus results will not be presented; this holds for all configurations.

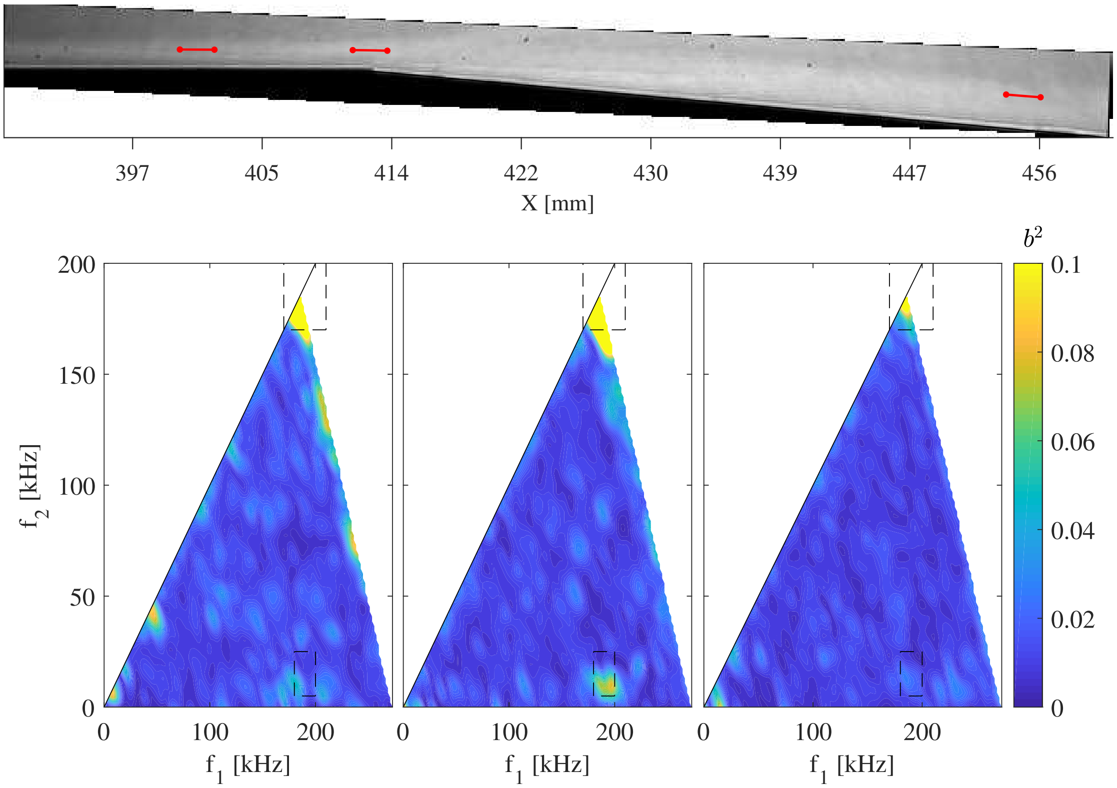

Figure 6.7: (Top) Time-averaged, flow-on image for the -5° configuration at condition Re33 with red circles denoting distinct regions for computing the bicoherence. (Bottom) Bicoherence spectra for each annotated region with the contours ordered stream-wise from left to right.

6.2 -5 ° Extension

As may be expected from its effect on the boundary-layer disturbances, the expansion acts largely to dampen nonlinear interactions. Upstream of the corner at condition Re33 (figure 6.7), the primary peaks correspond to fundamental resonance and sideband interactions/low-frequency coupling. Downstream these interactions diminish substantially, with no new peaks appearing in the bicoherence spectra.

The top contour of figure 6.8 was computed for interactions within the region $[f_1,f_2] = [190 \pm 20\,\mathrm{kHz}, 190 \pm 20\,\mathrm{kHz}]$, corresponding to fundamental resonance.

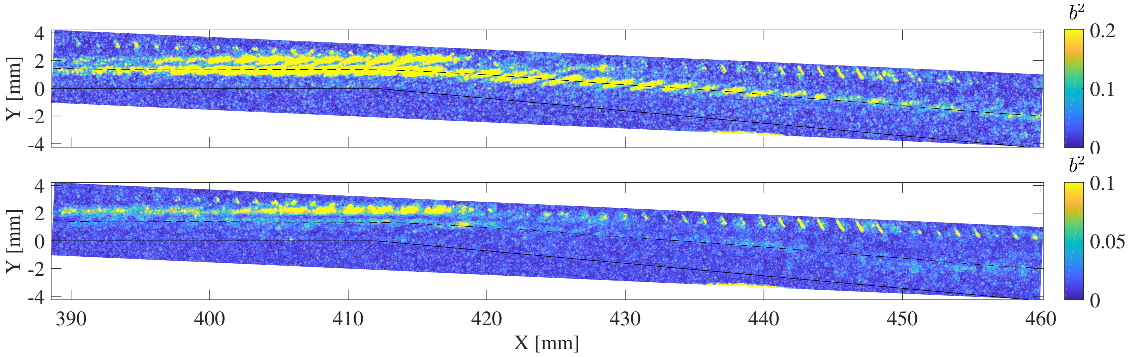

Figure 6.8: Spatial bicoherence contours at condition Re33 for frequency triplets of (a) [190,190,380] and (b) [190,15,205].

This interaction amplifies until the corner before gradually diminishing along with the second-mode waves. While this interaction is largely concentrated along the pseudo-streamline, there also appears to be a band of elevated bicoherence above the streamline upstream of the corner. It is along this upper band that the lower contour of figure 6.8, $[f_1,f_2] = [190 \pm 10\,\mathrm{kHz}, 15 \pm 10\,\mathrm{kHz}]$, demonstates significant intensity. This corresponds to low-frequency coupling with the second-mode disturbances and appears similar to the phenomenon observed along the stright cone in figure 6.4. It is worth emphasizing again that bispectral analysis is incapable of distinguishing between sum and difference interactions. It is thus ambiguous as to whether this interaction corresponds to deconstructive interference between second-mode structures at 190 kHz and 205 kHz to produce low-frequency content or if content at approximately 15 kHz is facilitating energy exchange between second-mode structures; the latter explanation seems more likely, however, given the presence of the 13 kHz structures upstream of the bicoherence peak revealed by the SPOD analysis.

This dampening effect is further exaggerated at condition Re45, as seen in the spectra of figure 6.9. Upstream of the corner we see what are likely aliased second-mode interactions around [220 kHz,120 kHz]. As a reminder, interactions which occur along the right edge of the triangle may also be mapped to resonant interactions at [f_1,f_1]. However, the spatial contour for this interaction (lower image of figure 6.10) demonstrates limited coherence. This interaction occurs alongside low-frequency resonance at $80 - 90$ kHz with corresponding low-frequency coupling. Immediately downstream of the corner these interactions all vanish, leaving only a peak at 10 kHz of dubious significance. Probing the spatial distribution of the 80 kHz resonance reveals something surprising in that the bicoherence intensity is concentrated in a fashion which resembles the fundamental resonance at condition Re33. These interactions may thus relate to the first harmonic of the second mode, as content at $80 - 90$ kHz would also correspond to aliased content from $460 - 470$ kHz and, although no coherent flow structures were observed in the SPOD mode shapes within this frequency range, harmonic structures were revealed by the bandpass-filtered images.

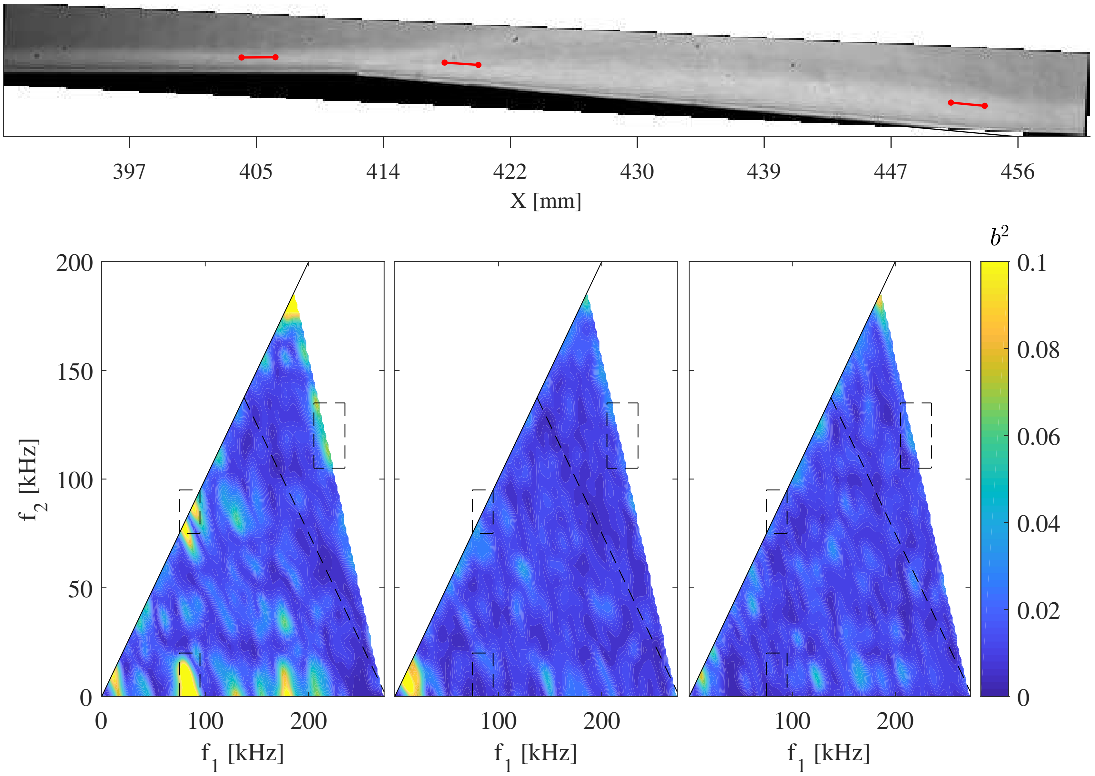

Figure 6.9: (Top) Time-averaged, flow-on image for the -5° configuration at condition Re45 with red circles denoting distinct regions for computing the bicoherence. (Bottom) Bicoherence spectra for each annotated region with the contours ordered stream-wise from left to right.

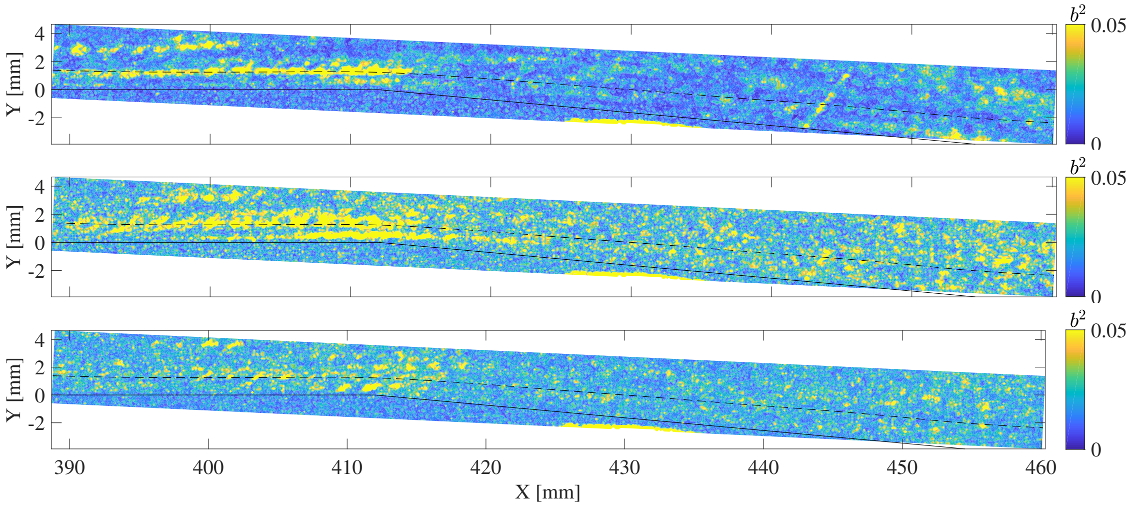

Figure 6.10: Spatial bicoherence contours at condition Re45 for frequency triplets of (top to bottom) [85,10,95], [85,85,170], and [220,120,340].

6.3 $+5\,^\circ$ Extension

The compression corner configurations generally lead to the development of new nonlinear exchange mechanisms. Figure 6.11 demonstrates this point for the +5° configuration at condition Re33, for which the increased framerate of the test (822 kHz) facilitates better resolution of interactions. The top-left contour verifies the presence of fundamental resonance near 200 kHz as well as low-frequency coupling in the immediate vicinity of the corner. From the spatial contour of figure 6.12(d) we see that this resonance enters from upstream of the field of view concentrated along the pseudo-streamline, and persists downstream of the corner until approximately $X = 430\,\mathrm{mm}$, at which point the interaction dissipates and moves closer to the wall. Indeed, the second streamwise station in figure 6.11 demonstrates the continued presence of 200 kHz resonance, but it is absent at the third station.

Additional resonant interactions develop at the second station of figure 6.11 around frequencies of 80 kHz and 160 kHz, which happen to be a harmonic pair. There also appears to be an interaction between these frequencies, with a peak occuring at $[f_1, f_2] = [160\,\mathrm{kHz}, 70\,\mathrm{kHz}]$, and a large degree of low-frequency coupling is seen in the vicinity of [160 kHz,10 kHz]. As seen in figures 6.12(b) and (c), these interactions peak sharply from $X = 420 - 430\,\mathrm{mm}$. This region corresponds closely to where the 77 kHz and 161 kHz SPOD mode shapes presented in figure 5.10 first develop, with the 160 kHz structure appearing slightly further upstream. The interaction at [160 kHz,70 kHz] may thus be explained as deconstructive interference between second-mode wavepackets at 230 kHz and the low-frequency content to pro-

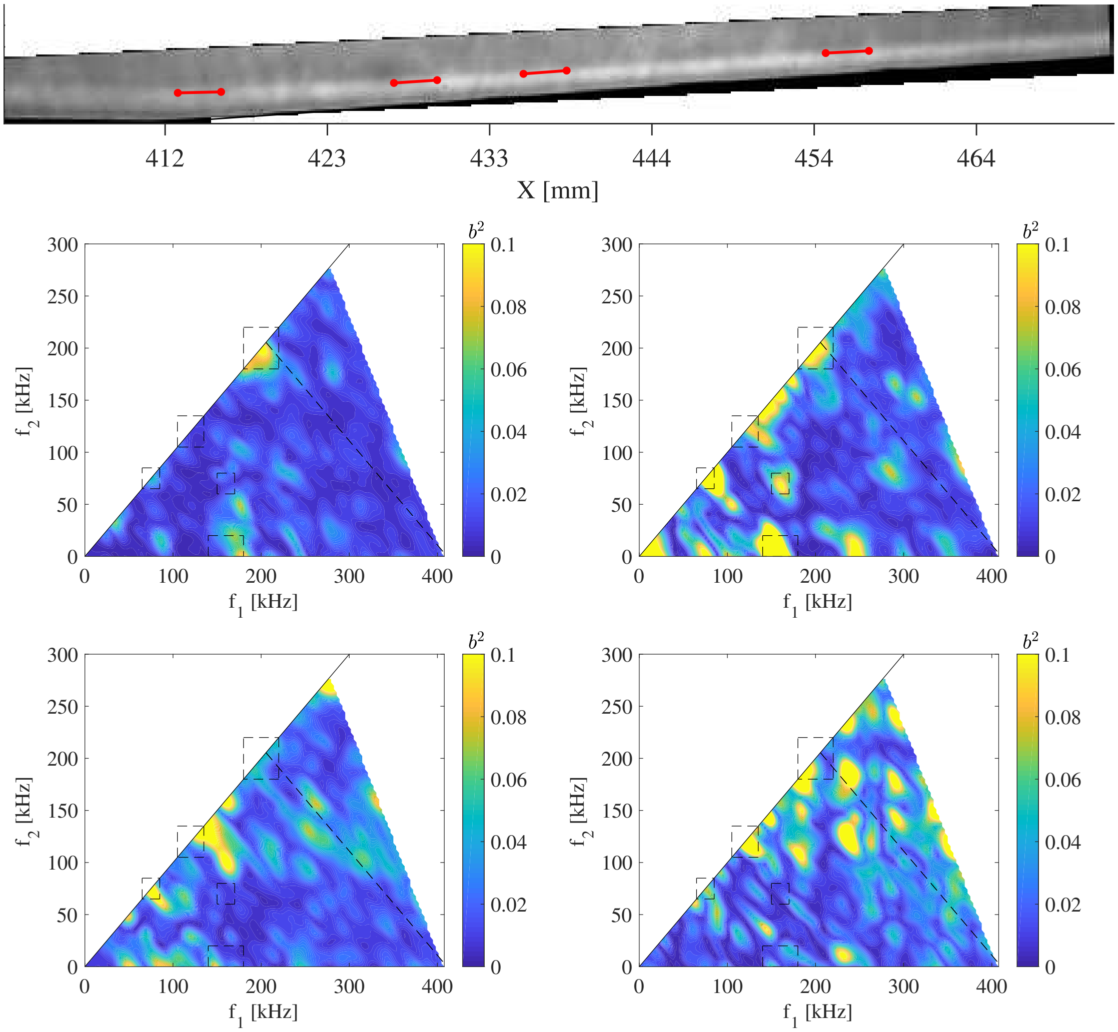

Figure 6.11: (Top) Time-averaged, flow-on image for the +5° configuration at condition Re33 with red circles denoting distinct regions for computing the bicoherence. (Bottom) Bicoherence spectra for each annotated region with the contours ordered stream-wise from top-left to bottom-right.

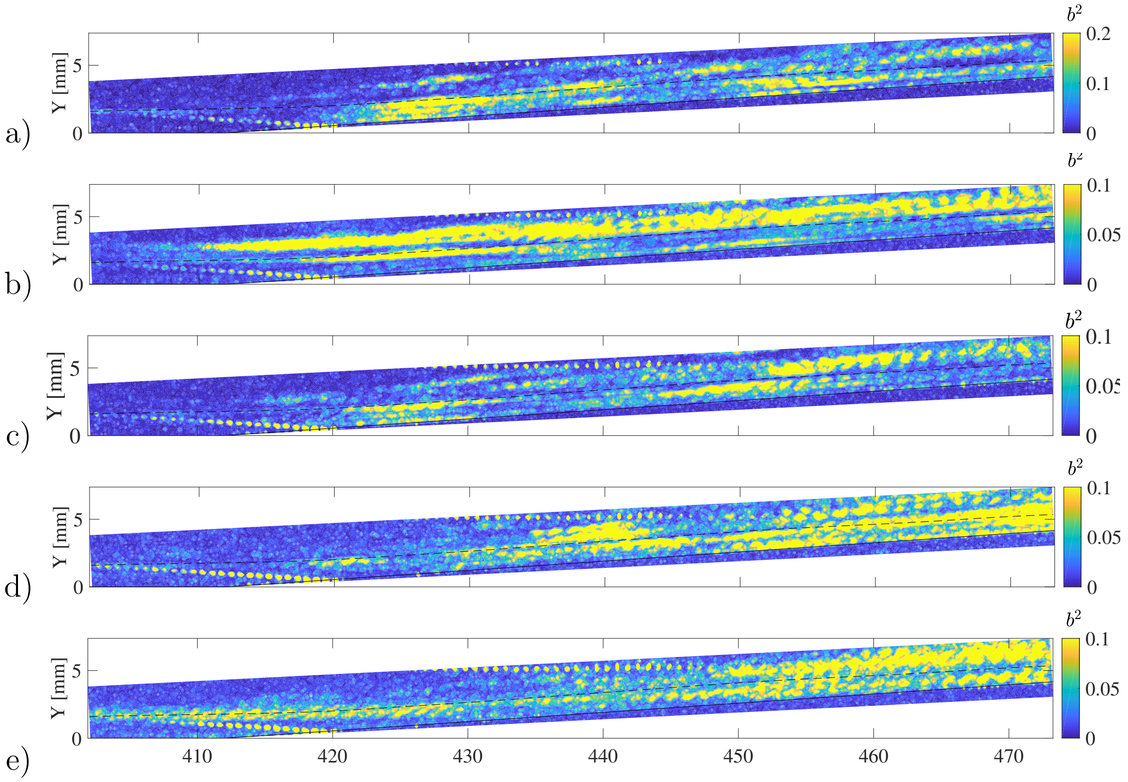

Figure 6.12: Spatial bicoherence contours for the +5° flare at condition Re33 for frequency triplets of (a) [75,75,150], (b) [160,10,170], (c) [160,70,230], (d) [120,120,240], and (e) [200,200,400].

duce additional low-frequency structures. This conclusion seems far more likely than the alternative that the second-mode waves are amplified by interaction of separate, lower-frequency disturbances. Notably, the interaction at [160 kHz,10 kHz] actually emanates energy from just upstream of the corner; this likely corresponds to the corner shock, as mean flow interactions are captured by this contour.

The resonant interaction at 120 kHz which peaks at the third pixel station has the same general spatial distribution (seen in figure 6.12d) as the preceding interactions, but shifted downstream. This interaction can be matched to the SPOD structure at 125 kHz, which peaks in amplitude within the vicinity of $X = 440$ mm. At the furthest downstream station, the bicoherence spectra has developed a grid of

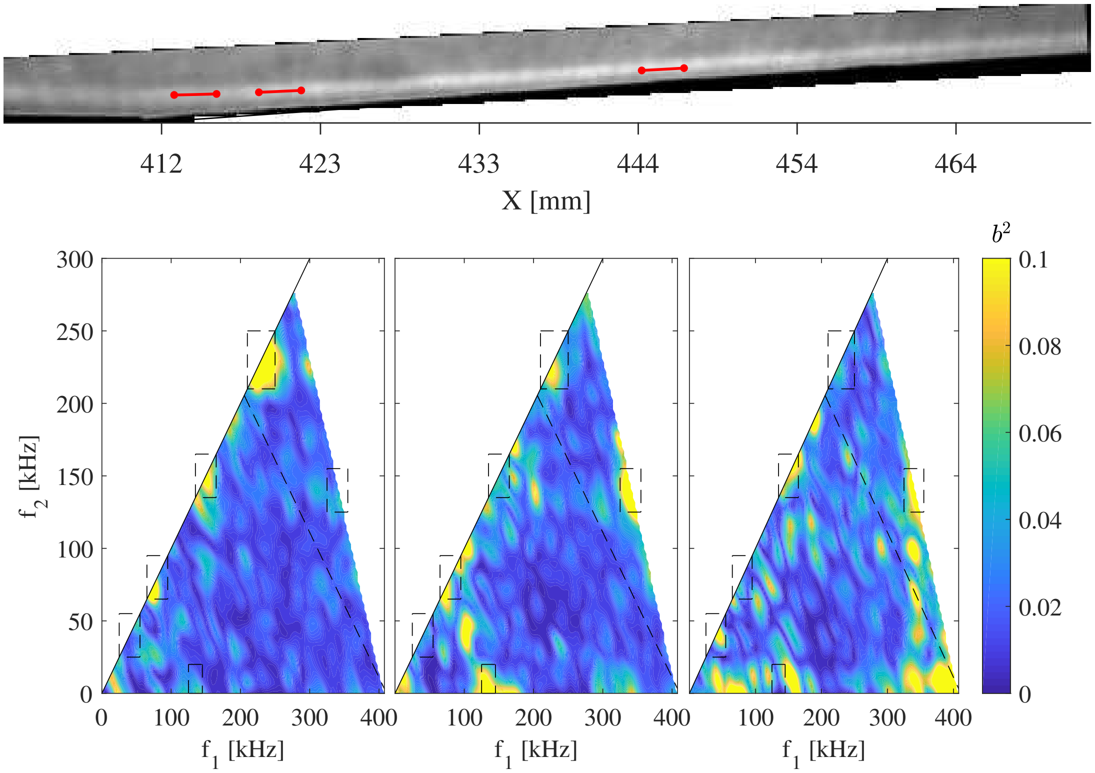

Figure 6.13: (Top) Time-averaged, flow-on image for the +5° configuration at condition Re45 with red circles denoting distinct regions for computing the bicoherence. (Bottom) Bicoherence spectra for each annotated region with the contours ordered stream-wise from left to right.

peaks with a spacing of approximately 60 kHz, suggesting there may exist some key structure at this frequency which facilitates energy transfer. That said, this station lies far enough downstream that the flow is consistently transitional and intermittently turbulent, which may contaminate the spectra and produce less meaningful results. In fact, it should be noted that the spatial bicoherence distributions of all interactions illustrated by figure 6.12 appear dominated by turbulent artifacts downstream of $X = 450\,\text{mm}$.

Figure 6.13 shows bicoherence spectra computed for pixel stations on the +5° flare at condition Re45. Right at the corner, the primary interaction is still

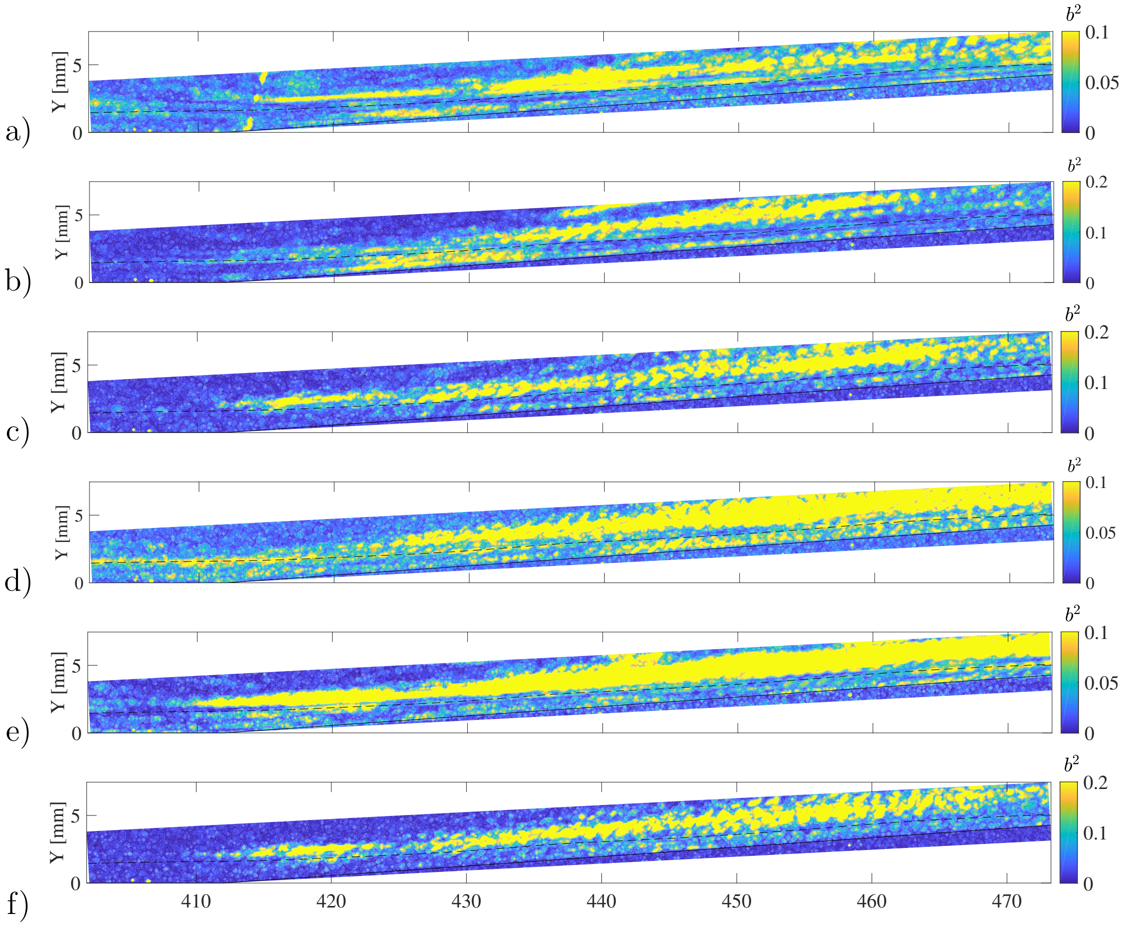

Figure 6.14: Spatial bicoherence contours for the +5° flare at condition Re45 for frequency triplets of (a) [40,40,80], (b) [80,80,160], (c) [150,150,300], (d) [230,230,460], (e) [135,10,145], and (f) [340,140,480].

fundamental resonance at 230 kHz, though there appear to be additional resonances at 75 and 150 kHz. Slightly downstream, strong peaks appear at [135 kHz, 0 kHz] and [340 kHz, 140 kHz]. These interactions along with the second-mode resonance dissipate quickly, with a new resonant interaction at 165 kHz appearing in the spectrum of the third station. The majority of high-frequency interactions observed at the most downstream pixel station were found to have little spatial coherence and are believed to be turbulent artifacts.

Spatial bicoherence distributions for the primary interactions mentioned above are given in figure 6.14. The first four contours correspond to resonant interactions at 40 kHz, 80 kHz, 150 kHz, and 230 kHz, respectively. The dominant feature for all these interactions is a band of substantially elevated signal which emanates away from the boundary layer. This band originates from $X = 415 - 435\,\mathrm{mm}$ depending on the resonant frequency and likely corresponds to turbulent features. Resonance of the second-mode fundamental at 230 kHz (figure 6.14d) is seen along the pseudo-streamline at the beginning of the field of view but rapidly drops off downstream of the corner. There is some evidence of continued fundamental resonance within the flare boundary layer, but it is difficult to assign physical significance to the elevated signal here given the obvious turbulent contamination. The other interactions spike in amplitude dramatically from $410 - 420\,\mathrm{mm}$, with much of the signal concentrated above the streamline. Synthesizing the results for both conditions, the $+5^{\circ}$ compression results in a spike in nonlinear interaction within a small region early on the flare which may alter the transition process significantly.

6.4 $+10^{\circ}$ Extension

The appearance of the separation bubble and the shear-generated disturbances with the $+10^{\circ}$ flare has a significant impact on the bicoherence computed along the pseudo-streamline. That said, figure 6.15 shows that fundamental resonance is still captured upstream of the separation point at [220 kHz, 220 kHz] at condition Re33. Low-frequency coupling is simultaneously observed at approximately [230 kHz, 20 kHz], corresponding to energy exchange with the upper sideband of the

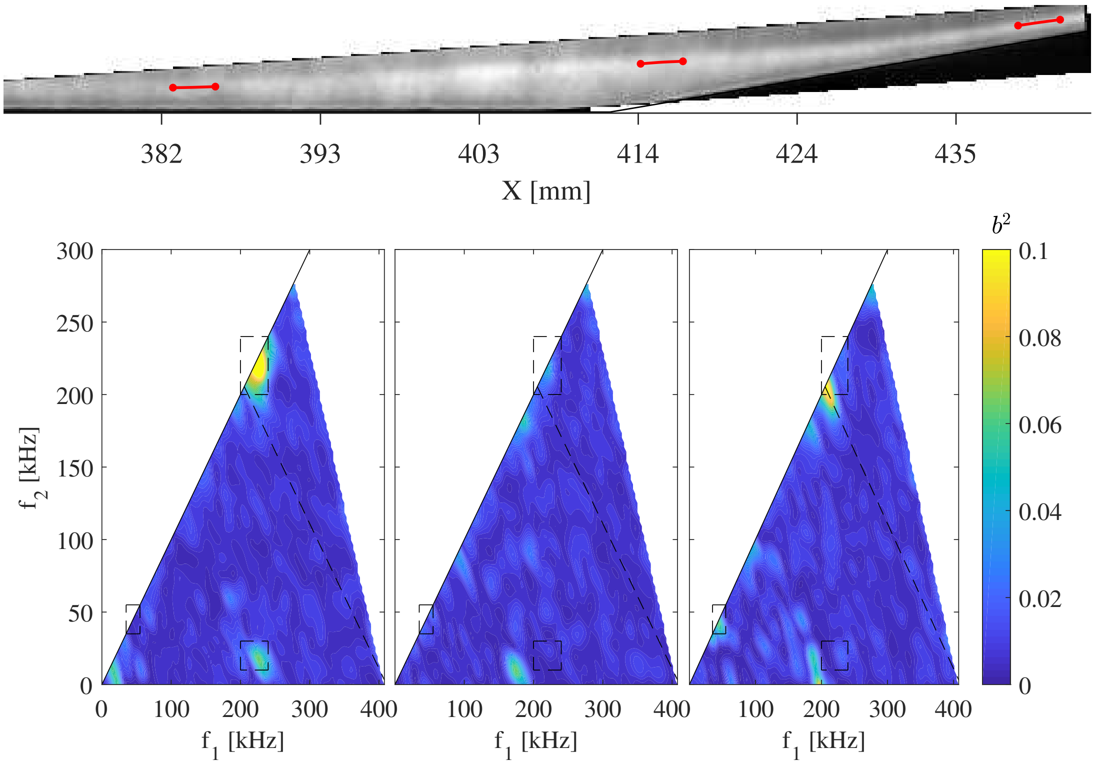

Figure 6.15: (Top) Time-averaged, flow-on image for the +10° flare at condition Re33 with red circles denoting three distinct regions for computing the bicoherence. (Bottom) Bicoherence spectra for each annotated region with the contours ordered stream-wise from left to right.

second-mode disturbances. Within the separation bubble, these peaks drop off and there is little evidence of nonlinearity along the pseudo-streamline. Downstream of reattachment there is a resurgence in fundamental resonance, though the peak now lies at [205 kHz, 205 kHz]. There is also weak evidence of a new, low-frequency resonant interaction at [45 kHz, 45 kHz].

The disappearance of second-mode interactions downstream of separation is further demonstrated by the bottom two spatial contours in figure 6.16 which correspond to [220 ± 20 kHz,20 ± 10 kHz] and [220 ± 20 kHz,220 ± 20 kHz]. Fundamental resonance amplifies up until $X = 392$ mm, at which point the peak diminishes

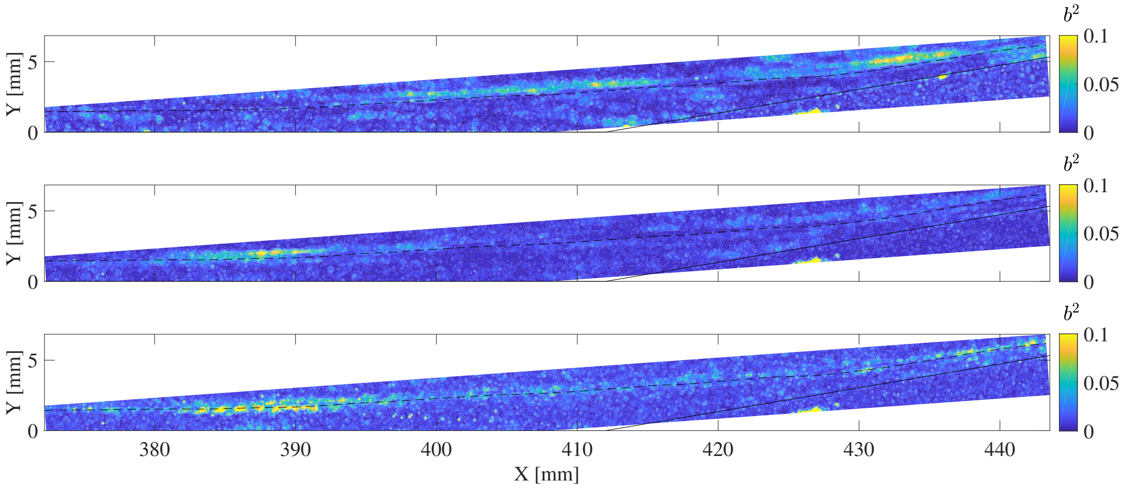

Figure 6.16: Spatial bicoherence contours for the +10° flare at condition Re33 for frequency triplets of (top) [45,45,90], (middle) [220,20,260] and (bottom) [220,220,440].

rapidly. This is mimicked by the interaction at [220 kHz,20 kHz], which is again concentrated above the pseudo-streamline. The top contour of figure 6.16 reveals a coherent structure to the 45 kHz resonance which is obscured when restricting our analysis to the pseudo-streamline. This interaction appears along the upper edge of the separation bubble and peaks in the vicinity of reattachment. We will see a similar structure for resonance of the shear mode with the +15° configuration.

Bicoherence spectra within the separation bubble and in the vicinity of reattachment are given in figure 6.17 for condition Re45. There is a significant increase in nonlinearity within the separation region relative to condition Re33. There now exist two distinct resonant interactions at approximately [140 kHz, 140 kHz] and [70 kHz, 70 kHz]. There are also prevalent high-frequency interactions in the vicinity of [320 kHz, 10 kHz] and [320 kHz, 180 kHz]. These interactions likely correspond to harmonic content aliased down from 500 kHz. Just upstream of reattachment, we see the development of significant resonances near 55 kHz and 160 kHz. The upper spatial contour of figure 6.18 shows that the 55 kHz interaction peaks within a confined spatial region along the pseudo-streamline. From the SPOD analysis we can conclude that this behavior corresponds to the lower-frequency shear mode observed at 61 kHz (in figure 5.15). As with the +5° configuration, the streamline curvature appears to create a concentrated region close to the corner in which the nonlinear interactions occur. Resonance of the high-frequency, shear-generated structures at [75 kHz, 75 kHz] appears in the middle contour of figure 6.18, and is visible further upstream but does not peak as significantly in the vicinity of reattachment. By contrast, the 160 kHz interaction in the lower contour demonstrates little spatial coherence and appears largely due to turbulence. The significance of interactions which appear in the third pixel station of figure 6.17, just downstream of reattachment, is likewise unclear.

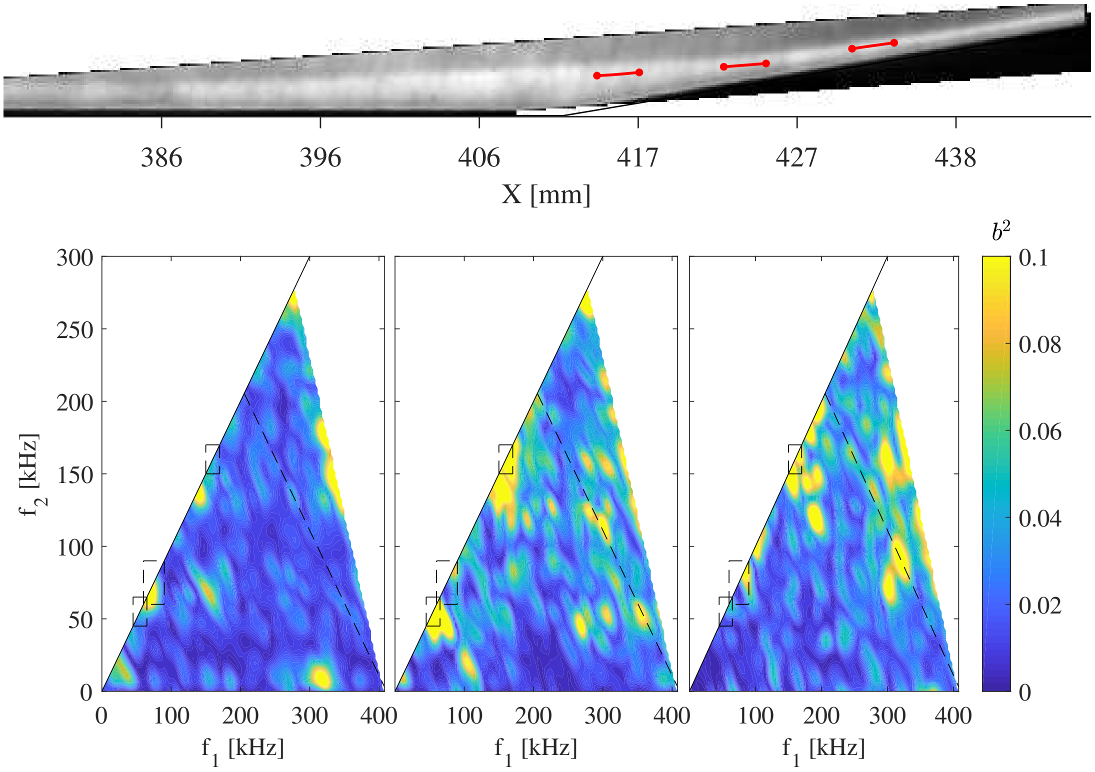

Figure 6.17: (Top) Time-averaged, flow-on image for the +10° flare at condition Re45 with red circles denoting three distinct regions for computing the bicoherence. (Bottom) Bicoherence spectra for each annotated region with the contours ordered stream-wise from left to right.

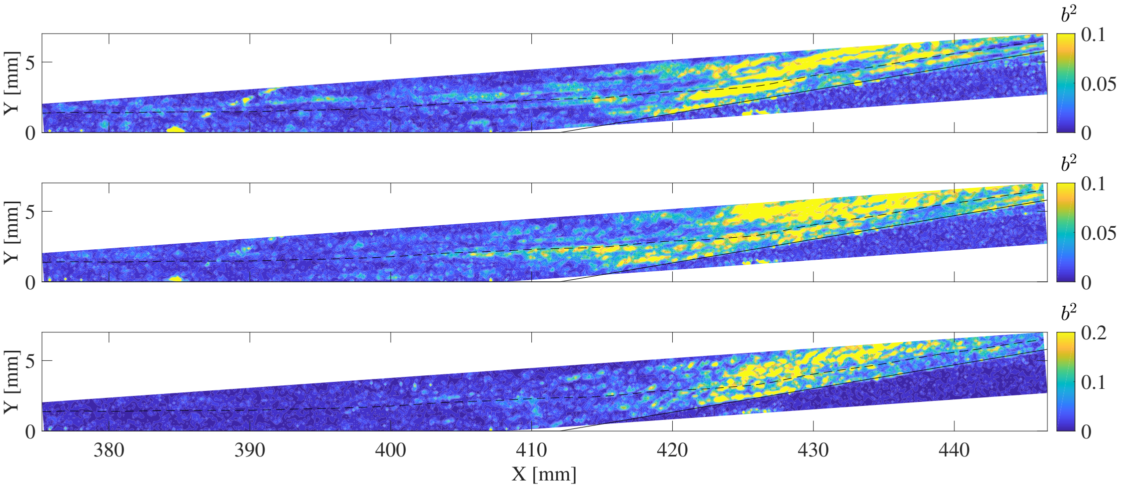

Figure 6.18: Spatial bicoherence contours for the +10° flare at condition Re45 for frequency triplets of (top to bottom) [55,55,110], [75,75,150], and [160,160,320].

6.5 +15 ° Extension

The reduced framerates employed with this configuration (440 kHz at condition Re33 and 550 kHz at Re45) render it impossible to properly resolve nonlinear interactions involving second-mode disturbances without significant aliasing. Fortunately, the preceding sections have demonstrated that the boundary layer in this configuration is largely dominated by lower-frequency structures which are still well-resolved. At condition Re33, as with the +10° configuration, there are no discernible peaks in the bicoherence through much of the upstream portion of the separation bubble. The first region presented in figure 6.19 is located slightly upstream of the corner and is near where the shear-generated disturbances are first observed instantaneously. At this point, the bicoherence spectrum shows weak resonant interactions at 53 kHz and 117 kHz and a stronger, though still mild, interaction at [72 kHz, 12 kHz]. The physical significance of this interaction is unclear. Within the second region, now downstream of the corner, a strong peak develops at [40 kHz, 40 kHz] corresponding to self-resonance of the shear-generated disturbances. The upper spatial contour of figure 6.20 shows this interaction is concentrated near the pseudo-streamline, though not aligned with it, from $X = 418 - 425$ mm as the boundary layer recompresses. This correlates well with the peak interaction region seen for the +10° configuration in figure 6.18. Interestingly, there is an additional band of elevated bicoherence for this interaction above the pseudo-streamline; this band is seen as far upstream as 385 mm but peaks in the vicinity of reattachment.

Downstream of reattachment, a series of interactions can be seen in figure 6.19

to lie approximately along lines corresponding to $f_1 = 40\,\mathrm{kHz}$ and $f_2 = 40\,\mathrm{kHz}$. It is also worth noting that these peaks have approximately uniform spacing of $\Delta F = 20\,\mathrm{kHz}$. The interactions at [42 kHz, 20 kHz] and [60 kHz, 40 kHz] are presented in the lower contours of figure 6.20. Both contours share a similar structure with the 14 kHz SPOD mode in figure 5.18. As with the 40 kHz resonance, these interactions peak in strength as the boundary layer reattaches, but are visible far upstream. All this suggests that low-frequency oscillation of the separation bubble and the shear-generated disturbances couple together to facilitate energy transfer within the shear layer. This also demonstrates the shortcomings of the pseudo-streamline for this analysis, as these interactions follow very different trajectories.

At conditon Re45, resonance of the shear-generated instability at [50 kHz, 50 kHz] is observed in the first probed region of figure 6.21 as far upstream as $X = 405\,\mathrm{mm}$. This interaction amplifies downstream and new resonances appear at 25 kHz and 95 kHz within the second region. These are notable in that they correspond approximately to the subharmonic and harmonic of the shear-generated disturbances. The spatial distribution of the shear-mode resonance is shown in the second contour of figure 6.22 to peak just above the pseudo-streamline as the boudary layer recompresses, just as it did at condition Re33. However, the bicoherence peak no longer outlines the entirety of the separation bubble, and a ray of elevated signal is seen emanating from the shear layer. The bicoherence peak and ray of elevated signal align well with the SPOD structure displayed in figure 5.19 at 99 kHz. This suggests that the ribbon-like waves of energy which emanate from the boundary-layer may be caused by nonlinear resonance of the shear waves as they ap-

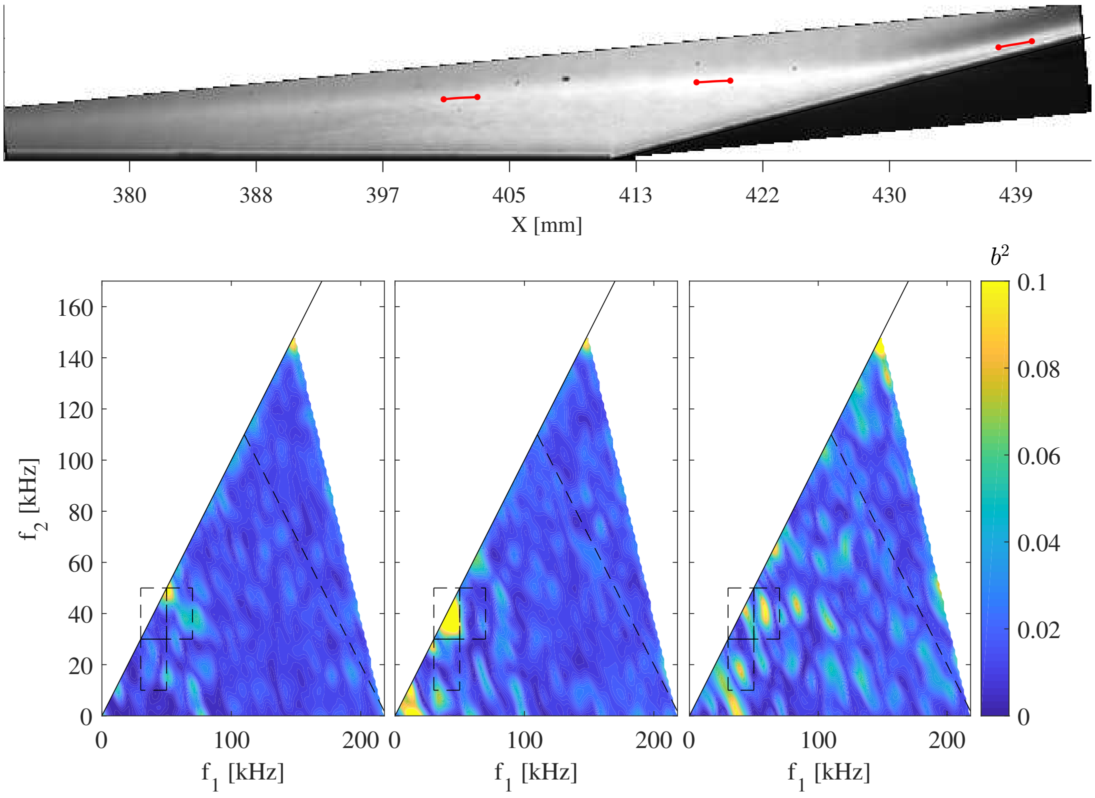

Figure 6.19: (Top) Time-averaged, flow-on image for the +15° configuration at condition Re33 with red circles denoting distinct regions for computing the bicoherence. (Bottom) Bicoherence spectra for each annotated region with the contours ordered stream-wise from left to right.

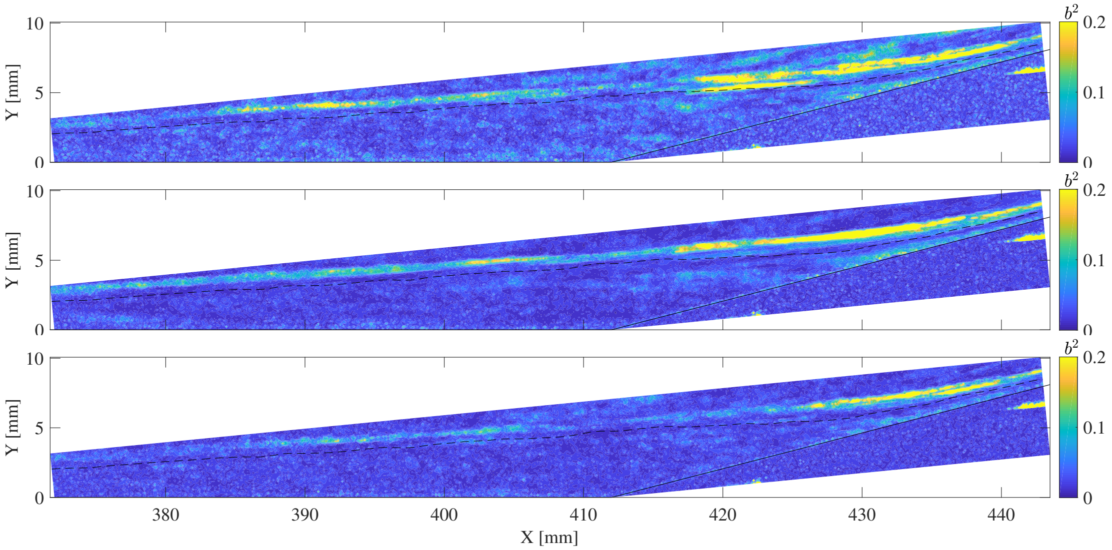

Figure 6.20: Spatial bicoherence contours for the +15° flare at condition Re33 for frequency triplets of (top to bottom) [40,40,80], [40,20,60] and [60,40,100].

proach reattachment. The potential subharmonic resonance at 25 kHz is illustrated by the upper-most contour of figure 6.22 and peaks above the pseudo-streamline within the same region as the fundamental shear-mode resonance; however, this interaction also displays elevated signal below the pseudo-streamline. Overall, this interaction correlates well with the 26 kHz structure resolved by the SPOD analysis in figure 5.19.

Another interesting feature of the bicoherence spectrum of the second station is the peak which develops at [100 kHz, 50 kHz], potentially corresponding to an interaction between the shear-generated disturbances and its first harmonic. The spatial distribution of this interaction (second contour of figure 6.22) again appears as a ray emanating from $X = 418\,\mathrm{mm}$ and closely aligns with the 146 kHz SPOD mode shape from figure 5.19, providing further evidence that second-harmonic content is generated within this interaction region.

Within the vicinity of reattachment, around $X = 430\,\mathrm{mm}$, interactions develop along the band corresponding roughly to $f_2 = 20\,\mathrm{kHz}$. This band of interactions persists and strengthens downstream (note the increased contour limits of the final station). These interactions are likely facilitated by a low-frequency structure similar to the 17 kHz SPOD mode which was concentrated near reattachment. Notably, these downstream interactions involve some much higher frequencies. The bottom contour of figure 6.22 shows that the coupling between [215 kHz, 20 kHz] is concentrated entirely within the compressed boundary-layer downstream of reattachment. This correlates with the high-frequency structures resolved within this region by the SPOD analysis.

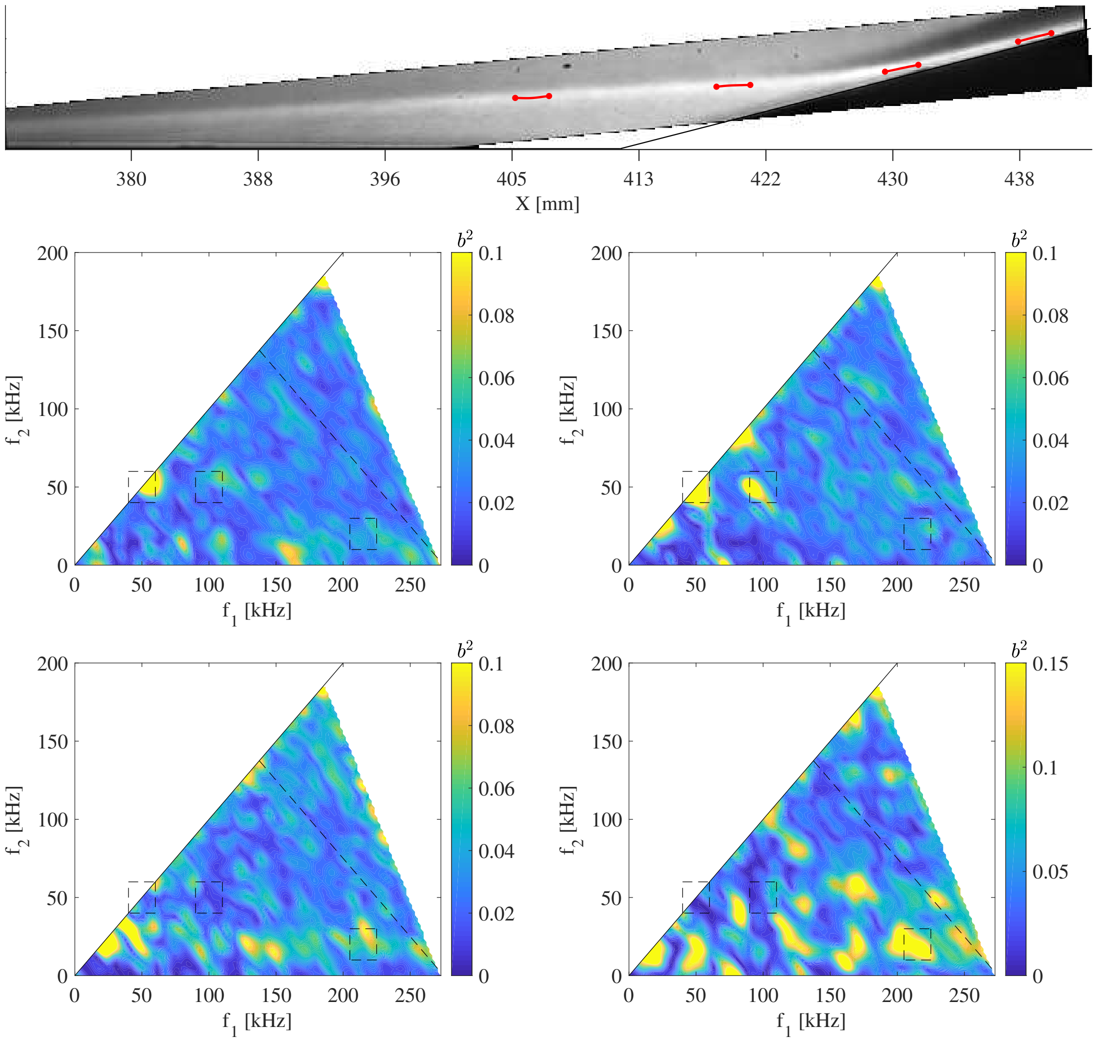

Figure 6.21: (Top) Time-averaged, flow-on image for the +15° configuration at condition Re45 with red circles denoting distinct regions for computing the bicoherence. (Bottom) Bicoherence spectra for each annotated region with the contours ordered stream-wise from left to right.

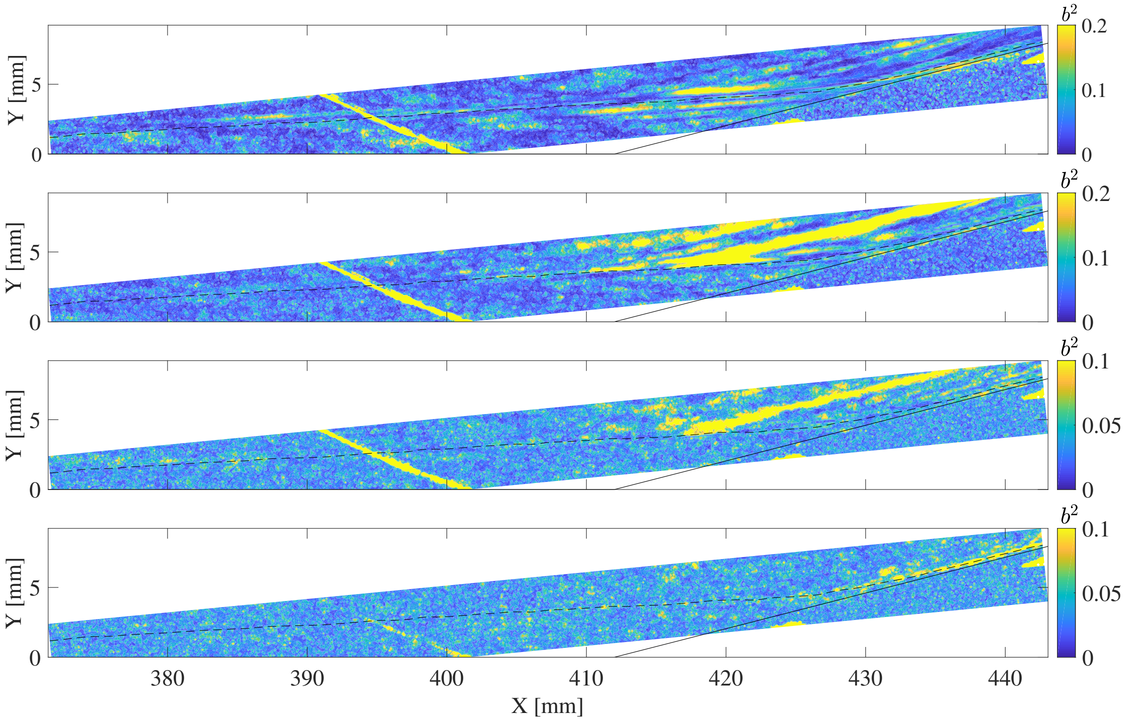

Figure 6.22: Spatial bicoherence contours for the +15° flare at condition Re45 for frequency triplets of (top to bottom) [25,25,50], [50,50,100], [100,50,150] and [215,20,235].

Chapter 7: LASTRAC

A limited computational study of the +10° configuration was carried out using LASTRAC (Langley Stability and Transition Analysis Code) at condition Re33. This was meant as a check on the fidelity of the experimental results and an attempt to computationally validate the appearance of the shear-generated instability. Only condition Re33 was selected for analysis due to the transitional nature of the flow at higher Re_m, which degrades the applicability of LST and PSE.

LASTRAC is a transition-prediction code developed by NASA which offers computations based on either quasi-parallel linear stability theory (LST) or the parabolized stability equations (PSE). The PSE formulation may be either linear (LPSE) or nonlinear, the latter of which requires knowledge of the incoming disturbance amplitude. All of these formulations are built upon a decomposition of the Navier-Stokes equations into mean and fluctuating components. By subtracting the mean-flow component, one arrives at the governing equations for disturbances imposed on the flow. In the linear formulations, these disturbances are assumed to be very small relative to the mean quantities, allowing the equations to be linearized. This means the Fourier modes develop independently and any nonlinear interactions are ignored. LST relies upon the assumption that the flow is locally quasi-parallel, meaning that streamwise variations are negligible. This results in the disturbance mode shape (χ) formulated as

$$\chi(x, y) = \psi(y)e^{i\alpha x}, \tag{7.1}$$

where α is the local complex wavenumber and ψ is the shape function which varies only with y.

Clearly, this assumption breaks down when considering separated flow over a compression corner. For this reason, the LST computations of this chapter were used primarily to identify the dominant instabilities and were supplemented by LPSE calculations at these discrete frequencies. LPSE accounts for nonparallel effects by decomposing the disturbances into a wave component described by the complex wave number, α, and a shape function, ψ, which is now allowed to vary with x. This formulation is given by

$$\chi(x, y) = \psi(x, y)e^{i\int_{x_0}^{x} \alpha(\xi)d\xi}. \tag{7.2}$$

Note that the history of the wavenumber is preserved within the integral. This results in upstream dependence, a feature which is absent in LST computations. A full description of the governing equations and numerical formulation of LASTRAC are given in the user manual [50].

Re_m [10^6/m]	U_∞ [m/s]	P_∞ [Pa]	T_∞ [K]	ρ_∞ [kg/m^3]
3.02	1279	601	113	0.019

Table 7.1: Inflow properties for the STABL2D mean flow computation.

7.1 Mean Flow

Computation of the mean flow was carried out using STABL2D (Stability and Transition Analysis for hypersonic Boundary Layers), developed by the University of Minnesota. The flow solver is based on the implicit Data Parallel-Line Relaxation method developed by Wright et al.[51] and employs a second-order, finite-volume formulation. A full description of the governing equations and implementation for 2-D/axisymmetric flows is given by Johnson [52]. Although the computations we performed for reservoir conditions equivalent to Re33, the freestream properties were instead computed based on the assumption of vibrational equilibrium throughout the nozzle and are given by table 7.1. The switch to a frozen-flow assumption from the nozzle throat was made after these computations had been completed. The mean flow was treated with a calorically perfect gas assumption; this is justified by the relatively low freestream temperature (113 K). The cone surface was treated as an isothermal wall at 300 K.

The computational grid was generated in a two-step process. First, the grid over the nosetip and frustum was generated with STABL's built-in grid solver including a nosetip bluntness of radius 0.1 mm. The flare geometry was then added within Pointwise. The full grid was dimensioned 1535 x 351 in the streamwise and wall-normal directions, and is shown in the left image of figure 7.1. Note that only

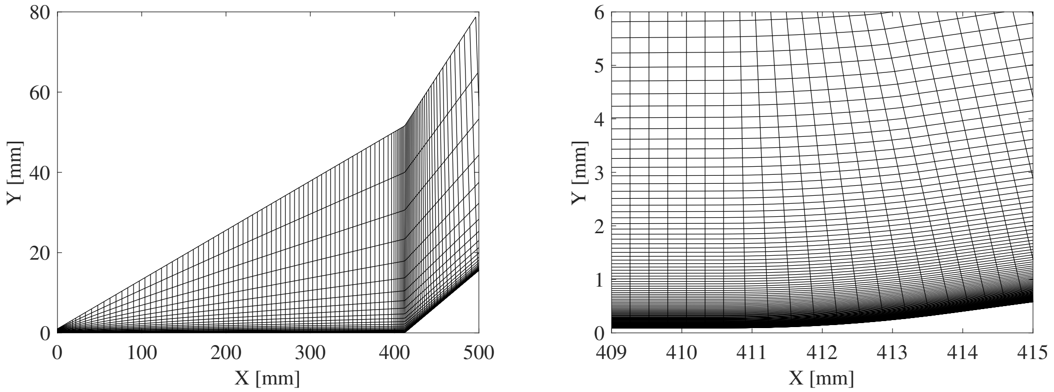

Figure 7.1: (Left) Full computational domain for mean-flow computations with reduced resolution for clarity and (right) half-resolution grid in the vicinity of the corner.

every tenth grid line is displayed to aid visual inspection. Wall-normal stretching was employed to cluster grid points within the boundary layer and the mean-flow computations were analyzed to ensure a resolution of at least 150 nodes. The grid was also stretched in the streamwise direction to increase resolution near the nosetip and within the separation region. Particular care was taken to keep the grid lines normal to the flare surface. This was accomplished by modelling the corner junction with a radius from $X = 411 - 413\,\mathrm{mm}$, as can be seen in the right image of figure 7.1, where the visible grid resolution has been halved.

Contours of x-velocity for the mean flow computation are shown in figure 7.2. Overlaid on the contour plot are: the boundary-layer thickness determined from the computation based on a 99.7% total enthalpy condition (solid line); the pseudo-streamline for the equivalent experiment (dashed line); and the separation and reattachment locations determined from the computation (solid) and the experiment (dashed). We see reasonable agreement between the experiment and computation for all metrics. It is expected that the pseudo-streamline would lie closer to the

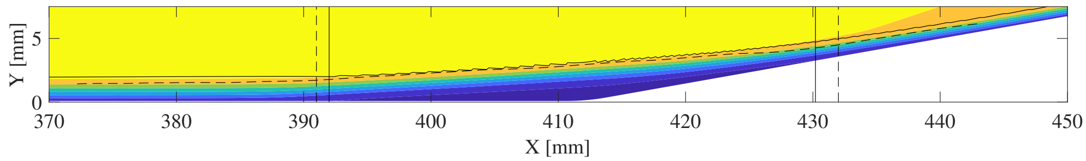

Figure 7.2: Mean flow contour of x-velocity overlaid with lines representing: the boundary-layer edge (solid); the pseudo-streamline for the corresponding test (dashed); the separation and reattachment locations determine from the computation (solid) and the experiment (dashed).

surface than the boundary-layer edge as the maximum second-mode fluctuations are typically observed around 80-90% of the boundary-layer thickness.

7.2 LST Results

LST calculations were performed for frequencies from $60 - 450\,\mathrm{kHz}$ over the length of the model with a quasi-parallel flow assumption. Resulting amplification rates and N factors over the parameter space are displayed in figure 7.3; the computationally determined separation and reattachment locations are included for reference. Note that within the gray regions, the local eigenvalue search returned no unstable modes and no data is given. The N factors are integrated from the first appearance of an unstable mode at each frequency. The second mode is the only amplifying disturbance over much of the frustum, first appearing at $X = 179\,\mathrm{mm}$ around $300\,\mathrm{kHz}$ (not pictured) and peaking in amplitude at $222\,\mathrm{kHz}$ just prior to separation. This is a slightly higher peak frequency than that observed experimentally along the pseudo-streamline, but still represents acceptable agreement. Within the separation region, amplification shifts to lower frequencies, with three distinct shear-generated modes appearing. The middle mode overlaps significantly with

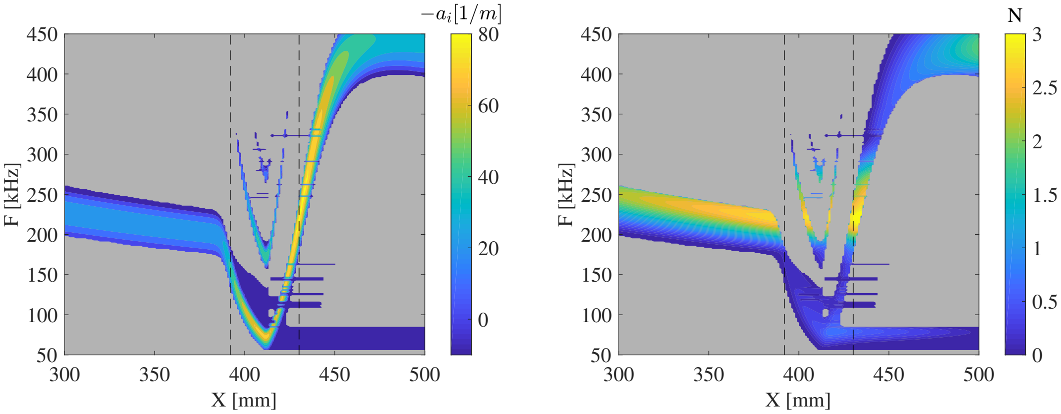

Figure 7.3: LST contours of (left) amplification rate and (right) N-factor as functions of streamwise location and frequency.

the second mode, resulting in N factors which likely are not representative of the shear-generated disturbance. The lower frequency mode is the one which persists downstream of reattachment, peaking at around 78 kHz. This is also slightly higher than the 71 kHz peak observed experimentally.

7.3 LPSE Results

Based on the preceding results, non-parallel LPSE computations were performed at frequencies of 222 kHz (the peak second-mode frequency upstream of separation) and 78 kHz (representing the shear-generated disturbances). Disturbance eigenfunctions of pressure, temperature and numerical "schlieren" (vertical density gradient) are visualized spatially in figure 7.4 for the 222 kHz disturbance. Note the visualization domain has been cropped to approximate the field of view in the experiments. This "schlieren" contour reveals a spatial structure which closely matches that observed in the reference-subtracted image sequences and the SPOD analysis. Upstream of separation, the disturbances are characterized by the typical

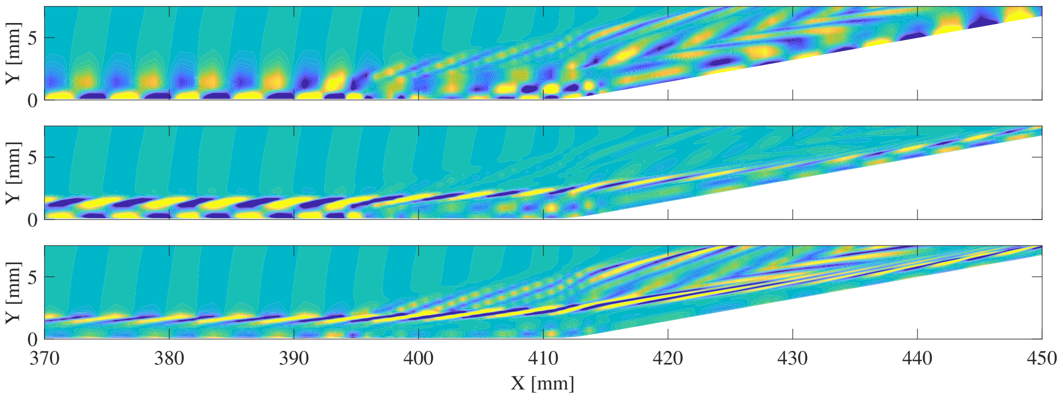

Figure 7.4: Fluctuation eigenvalue contours computed for a 222 kHz disturbance: (a) pressure, (b) temperature, and (c) numerical schlieren.

rope-like appearance. Traversing the separation bubble, the disturbances flatten out substantially and radiation of disturbance energy is observed at both separation and reattachment.

These same eigenfunction contours are shown for the 78 kHz disturbance in figure 7.5. Encouragingly, the "schlieren" eigenfunction for this disturbance shows excellent agreement with the structure of the shear-generated disturbances revealed in the 71 kHz SPOD contour of figure 5.14. There is also a strong ray of disturbance energy emanating away from the shear layer at around $X = 415\,\text{mm}$. This feature appears to be acoustic in nature, as it is also apparent in the pressure contour. Although this radiation is cut off in the SPOD mode by the field of view, there is some elevated signal visible near the top of the frame which correlates well with the LPSE structure. The shear-layer disturbance is visible in the temperature and "schlieren" contours even upstream of separation; however, the pressure disturbances do not become apparent until the immediate vicinity of the corner, where they amplify rapidly near the model surface. This is consistent with the observations of the disturbance

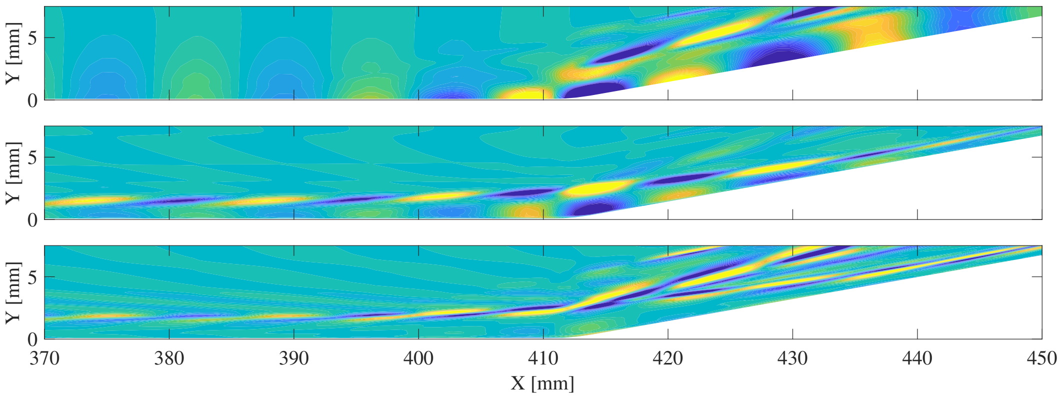

Figure 7.5: Fluctuation eigenvalue contours computed for a 78 kHz disturbance: (a) pressure, (b) temperature, and (c) numerical schlieren.

in the spectra of PCB D1. Overall, these experiments show good agreement with the experimental results.

Chapter 8: Conclusions

A notable gap in the literature surrounding high-speed boundary-layer transition concerns the interaction of disturbances with the mean flow structures imposed by sudden angle changes. This study has sought to fill this gap and characterize the development of second-mode wavepackets in the vicinity of axisymmetric compression and expansion corners.

All experiments were conducted at the University of Maryland - College Park in our HyperTERP reflected-shock facility. For these experiments, HyperTERP was equipped with a contoured nozzle with a nominal exit Mach number of 6. Pitot rake characterization studies suggest this is a good approximation of the freestream conditions considering the effects of vibrational nonequilibrium. Three test conditions were considered with the total specific enthalpy held constant in order to isolate the effects of Reynolds number. A model consisting of a 5° half-angle, conical forebody was selected to encourage the dominance of second-mode wavepackets upstream of the interaction region. Interchangeable afterbody attachments corresponding to flow deflections of -5° to +15° in 5° increments were considered. High-speed schlieren photography was employed as the primary means of flow interrogation, with supplemental surface measurements provided by PCB132B38 pressure transducers. A lens calibration was applied to the images to provide quantitative fluctuations in density gradient.

Reference-subtracted image sequences revealed the time-resolved, qualitative behavior of wavepackets in the vicinity of the corner. With the +0° extension, the boundary layer was dominated by the typical, rope-like structure of second-mode wavepackets. Transitional behavior was observed near the forebody/afterbody junction and generally moved upstream with increasing Re_m. Surface pressure spectra demonstrated peak second-mode frequencies in the range of $200-300\,\mathrm{kHz}$. Significant spectral broadening occured in the PCB spectra within the transitional flow region.

The primary visible effect of the expansion corner was the suppression of disturbances. This applied to second-mode wavepackets as well as turbulent structures, and was accompanied by a decrease in the magnitude of surface pressure fluctuations. Interestingly, second-mode energy was observed emanating away from the boundary layer along the head of the expansion wave. A similar phenomenon was witnessed in the +5° configuration whereby second-mode wavepackets would radiate energy along the corner shock. Even this modest compression appeared to encourage transition of incoming wavepackets, though qualitative alterations to the structure of the incoming disturbances was difficult to identify.

When the flow deflection reached +10° the boundary layer separated upstream of the corner, resulting in a recirculation region bounded by separation and reattachment shocks (along which additional second-mode radiation was observed). The second-mode disturbances would generally lift off the surface at the separation point and propagate largely within the separated shear layer, flattening as they travelled downstream. At the lowest studied Re_m, the boundary layer was found to remain laminar through both separation and reattachment, though the disturbances appeared significantly modulated over the flare with clearly reduced structure angles. At the highest Re_m, the observed instabilities would break down immediately upon encountering the separation shock, resulting in a predominantly turbulent boundary layer on the flare.

The +15° extension produced a much larger separation region which was no longer characterized by second-mode wavepackets at low Re_m. Instead, the corner region was dominated by shear-generated disturbances which amplified significantly within the downstream portion of the separation bubble. These disturbances appeared as braided structures in the schlieren images and emanated wavy energy structures as they reattached on the flare. These structures persisted downstream of reattachment in the thin, flare boundary layer. The few second-mode wavepackets observed at low Re_m generally lost distinction over the corner and appeared to merge with the shear waves. At the highest-studied Re_m, the separation region shrunk significantly and second-mode disturbances again became dominant. As in the +10° case, the SWBLI would provoke bypass transition of the disturbances, leading to a consistently turbulent flare boundary layer. There was some evidence of unsteadiness in the mean flow field for this high Re_m case, as particularly strong bursts of turbulence would collapse the separation bubble which would then reform over time.

To facilitate novel image analysis, the camera framerate was kept at or above the Nyquist sampling rate of the dominant second-mode frequencies being studied. These time-resolved image sequences thus permitted the use of spectral analysis techniques to study the spatial development of modal content. For the expansion case, this revealed growth of lower-frequency second-mode content even as the incoming disturbances decayed. In all compression cases, the radiation phenomenon observed instantaneously appeared to cause a small but abrupt drop in second-mode energy. The +5° compression was shown to amplify not only high-frequency disturbances but also low-frequency content below 50 kHz. Complex growth and decay trends of second-mode disturbances were seen through separation and reattachment in the +10° configuration. The power of the disturbances appeared largely to freeze within the upstream portion of the bubble before amplifying again near reattachment. This spectral analysis technique also demonstrated the presence of low-frequency ($70-80\,\text{kHz}$), shear-generated disturbances within the separation region that were not obvious in the reference-subtracted sequences. The absence of second-mode wavepackets was confirmed for the +15° configuration and the shear generated disturbances were assigned dominant frequencies in the range of $40-60\,\text{khz}$.

Temporally bandpass-filtering the image sequences proved a useful technique for isolating instantaneous modal disturbances. In all cases, this method could be used to accentuate the structure of second-mode disturbances. The previously obscured shear-generated disturbances for the +10° configuration were shown to have a braided structure oriented nearly parallel to its propagation direction, matching the observations for the +15° tests. By leveraging aliasing effects, this technique was even proven capable of resolving instantaneous second-mode harmonic structures.

A more powerful technique for resolving coherent flow structures was demonstrated in spectral proper orthogonal decomposition. This technique provides ranked, orthogonal modes which both optimally capture the flow energy provided by snapshots and oscillate at distinct frequencies. While this technique performed well at demonstrating the development of second-mode frequencies, it was perhaps more useful for identifying less prominent structures related to amplification peaks from the spectral analysis. Through SPOD, the amplifying lower-frequency second-mode waves downstream of the expension corner could be visualized. This technique also revealed the structure of low-frequency disturbances amplified by the $+5^\circ$ configuration and provided an additional method by which to observe the shear-generated disturbances in the $+10^\circ$ case. For the stronger shear waves generated by the $+15^\circ$ compression, SPOD resolved the structures emanating from the downstream portion of the separation region which appeared to correspond to the first and second harmonics of the shear disturbances. At high enough Re_m, high-frequency structures were observed within the reattached boundary layer. The capability of determining second-mode propagation speeds from these SPOD modes was also demonstrated.

Nonlinear interactions were probed through bispectral analysis, which confirmed the presence of fundamental resonance and sideband interactions of the second mode upstream of the corner junction. Both of these interactions have been documented by prior researchers. Notably, bicoherence spectra were computed for each pixel in the field of view, permitting a global view of the spatial distribution of key nonlinear interactions. The expansion corner caused substantial decay of nonlinear behavior, although fundamental resonance persisted for some distance downstream. The spatial contours revealed low-frequency coupling between between second-mode waves and low-frequency content to be concentrated near the boundary-layer edge. The +5° compression provoked the development of many new resonant interactions which could be matched to structures resolved by the SPOD analysis. The streamline curvature imposed by the compression appeared to create a concentrated region early on the flare which led to a localized spike in nonlinear behavior. At the lowest studied Reyolds number, the separation bubble of the +10° configuration served largely to damp nonlinear interactions, with fundamental resonance ceasing immediately downstream of separation. At higher Reynolds numbers, significant low-frequency resonance was found to occur within the separation region, particularly in the vicinity of reattachment, with additional high-frequency and non-resonant interactions appearing on the flare. Even stronger resonance of the shear-generated disturbances was observed in the +15° case, again peaking upstream of reattachment. Spatial contours again revealed a region of elevated nonlinear activity which correlated with streamline curvature. These bispectral results suggest that the energy structures seen emanating from the shear layer near reattachment in the SPOD analysis are formed due to self-resonance of the shear waves. Evidence of subharmonic growth related to these shear waves was also presented.

Finally, a limited computational study was performed using LASTRAC to serve as a first comparison against results compiled for the +10° configuration. The mean flow, computed using STABL2D, demonstrated reasonable agreement with the experiments in terms of both boundary-layer thickness and separation length. The peak second-mode frequency upstream of separation was predicted to be 222 kHz based on linear stability theory, again representing good agreement with experiments. Multiple unstable modes were predicted within the separation region, with the maximum amplification acheived at 78 kHz. Additional computations were performed for these two frequencies employing the linear parabolised stability equations to examine their structural development through the SWBLI. Disturbance eigenfunction contours from the LPSE analysis showed excellent agreement with the disturbance structures resolved by SPOD, particularly for the shear-generated disturbances.

Continuation of this work should look first at improving the fidelity of the data set. The nature of impulse facilities produces a noisy flow environment, which has manifested itself throughout this work in the form of anomalous turbulent bursts which contaminate the data and make robust computation of modal structures and nonlinear interactions difficult. It would thus be greatly beneficial to obtain similar measurements in a tunnel following a different operating principle (such as a Ludwieg Tube) where freestream disturbances are likely to be of lower magnitudes. Another line of inquiry would involve mounting the cone at various angle of attack, which would introduce crossflow instability. This added instability mechanism may fundamentally alter the SWBLIs, particularly in the separated cases where the crossflow may interact with the shear-generated disturbances. The parameter space could be enhanced further by examining the effects of nosetip bluntness. Boundary-layer structures not resembling second-mode disturbances have been observed on cones with sufficient bluntness [18]. It would be interesting to observe these structures passing through the corner interaction regions presented in this study.

Bibliography

[1] P. Balakumar, H. Zhao, and H. Atkins. Stability of hypersonic boundary-layers over a compression corner. 2002. AIAA Paper 2002-2848.

[2] A. Dwivedi, G Sidharth, J. Nichols, G. Candler, and M. Jovanović. Reattachment streaks in hypersonic compression ramp flow: an input-output analysis. *J. Fluid Mech.*, 880:113–115, 2019.

[3] R. L. Kimmel and J. M. Kendall. Nonlinear disturbances in a hypersonic laminar boundary layer. 1991. AIAA Paper No. 91-0320.

[4] N. Chokani. Nonlinear spectral dynamics of hypersonic laminar boundary layer flow. *Physics of Fluids*, 11(12):3846–3851, 1999. doi:10.1063/1.870243.

[5] A. Fedorov. Transition and stability of high-speed boundary-layers. *Annual Review of Fluid Mechanics*, 43:79–95, 2011.

[6] L. M. Mack. Linear stability theory and the problem of supersonic boundary-layer transition. *AIAA Journal*, 13(3):278–289, 1975.

[7] A. Demetriades. Hypersonic viscous flow over a slender cone, part iii: Laminar instability and transition. In *7th AIAA Fluid and Plasma Dynamics Conference*, 1974. AIAA Paper No. 74-535.

[8] J. Potter and J. Whitfield. Boundary-layer transition under hypersonic conditions. In *AGARDograph No 97, Part III*, 1965.

[9] M. C. Fischer and R. D. Wagner. Transition and hot-wire measurements in hypersonic helium flow. *AIAA Journal*, 10(10):1326–1332, 1972.

[10] Stetson K. F., Thompson E. R., Donaldson J. C., and Siler L. G. Laminar boundary layer experiments on a cone at mach 8, part 1: Sharp cone. 1983. AIAA Paper 83-1761.

[11] K. F. Stetson and R.L. Kimmel. On hypersonic boundary-layer stability. 1992. AIAA Paper No. 92-0737.

[12] S. P. Schneider. Effects of high-speed tunnel noise on laminar-turbulent transition. *Journal of Spacecraft and Rockets*, 38(3):323–333, 2001.

[13] S. Laurence, A. Wagner, K. Hannemann, V. Wartemann, H. Lüdeke, H. Tanno, and K. Itoh. Time-resolved visualization of instability waves in a hypersonic boundary layer. *AIAA Journal*, 50(1):243–246, 2012.

[14] S. Laurence, A. Wagner, and K. Hannemann. Schlieren-based techniques for investigating instability development and transition in a hypersonic boundary-layer. *Experiments in Fluids*, 55(1782), 2014.

[15] S. Laurence, A. Wagner, and K. Hannemann. Experimental study of second-mode instability growth and breakdown in a hypersonic boundary-layer using high-speed schlieren visualization. *Journal of Fluid Mechanics*, 797:471–503, 2016. doi:jfm.2016.280.

[16] K. Casper, S. Beresh, J. Henfling, R. Spillers, and B. Pruett. High-speed schlieren imaging of disturbances in a transitional hypersonic boundary-layer. In *51st AIAA Aerospace Sciences Meeting including the New Horizons Forum and Aerospace Exposition*, 2013. doi:10.2514/6.2013-376.

[17] R. E. Kennedy, S. J. Laurence, M. S. Smith, and E. C. Marineau. Investigation of the second-mode instability at Mach 14 using calibrated schlieren. *Journal of Fluid Mechanics*, 845:R2, 2018.

[18] G. Grossir, F. Pinna, G. Bonucci, T. Regert, P. Rambaud, and O. Chazot. Hypersonic boundary-layer transition on a 7-degree half-angle cone at mach 10. In *AIAA Aviation Forum*, 2014.

[19] D. S. Miller, R. Hijman, and M. E. Childs. Mach 8 to 22 studies of flow separations due to deflected control surfaces. *AIAA Journal*, 2(2):312–321, 1964.

[20] A. Roghelia, H. Olivier, I. Egorov, and P. Chuvakhov. Experimental investigation of Gortler vortices in hypersonic ramp flows. *Exp. Fluids*, 58(139), 2017.

[21] G. Sidharth, A. Dwivedi, G. Candler, and J. Nichols. Onset of three-dimensionality in supersonic flow over a slender double wedge. *Phys. Rev. Fluids*, 3(093901), 2018.

[22] K. S. Heffner, A. Chpoun, and J. C. Lengrand. Experimental study of transitional axisymmetric shock-boundary-layer interactions at Mach 5. 1993. AIAA Paper No. 93-3131.

[23] R. Benay, B. Chanetz, B. Mangin, L. Vandomme, and J. Perraud. Shock wave/transitional boundary-layer interactions in hypersonic flow. *AIAA Journal*, 44(6):1243–1254, 2006.

[24] C. L Running, T. J. Juliano, J. S. Jewell, M. P. Borg, and R. L. Kimmel. Hypersonic shock-wave/boundary-layer interactions on a cone/flare model. 2018. AIAA Paper No. 2018-3702.

[25] C. L. Running, T. J. Juliano, M. P. Borg, and R. L. Kimmel. Characterization of post-shock thermal striations on a cone/flare. *AIAA Journal*, 58(5):2352–2358, 2020.

[26] E. K. Benitez, J. S. Jewell, S. P. Schneider, and S. Esquieu. Instability measurements on an axisymmetric separation bubble at Mach 6. 2020. AIAA Paper 2020-3072.

[27] A. Novikov, I. Egorov, and A. Fedorov. Direct numerical simulation of wave packets in hypersonic compression corner flow. *AIAA Journal*, 54(7):2034–2050, 2016.

[28] M. Lugrin, S. Beneddine, C. Leclercq, E. Garnier, and R. Bur. Transition scenario in hypersonic axisymmetrical compression ramp flow. *Journal of Fluid Mechanics*, 907:1–40, 2020.

[29] P. A. Sullivan. Interaction of a laminar hypersonic boundary layer and a corner expansion wave. *AIAA Journal*, 8(4):765–771, 1970.

[30] V. Zakkay, K. Toba, and T. Kuo. Laminar, transitional, and turbulent heat transfer after a sharp convex corner. *AIAA Journal*, 2(8):1389–1395, 1964.

[31] A. W. Bloy. The expansion of a hypersonic turbulent boundary layer at a sharp corner. *J. Fluid Mech.*, 67(4):647–655, 1975.

[32] K. Chung and F. K. Lu. Damping of surface pressure fluctuations in hypersonic turbulent flow past expansion corners. *AIAA Journal*, 31(7):1229–1234, 1993.

[33] J. A. Dawson, M. Samimy, and S. A. Arnette. Effects of expansions on a supersonic boundary layer: Surface pressure measurements. *AIAA Journal*, 32(11):2169–2177, 1994.

[34] Ames Research Staff. Equations, tables, and charts for compressible flow. NACA Report 1135, 1953.

[35] A. Amadio. Driver-gas tailoring for test-time extension using unconventional driver mixtures. *Electronic Theses and Dissertations*, page 992, 2006.

[36] M. Nishida. *Shock Tubes: Handbook of Shock Waves*, volume 1. Academic Press, 2001.

[37] W.C. Starshak, C.S. Butler, and S.J. Laurence. Optical free-flight measurements using gpu-accelerated computer graphics. 2018. AIAA Paper No. 2018-5385.

[38] D. Ort and J. Dosch. Influence of mounting on the accuracy of piezoelectric pressure measurements for hypersonic boundary-layer transition. 2019. AIAA Paper No. 2019-2292.

[39] M. Hargather and G. Settles. A comparison of three quantitative schlieren techniques. *Optics and Lasers in Engineering*, 50:8–17, 2012.

[40] R. Kennedy. An experimental investigation of hypersonic boundary-layer transition on sharp and blunt slender cones. In *Ph.D. Thesis*. University of Maryland - College Park, College Park, Maryland, 2019.

[41] J. Sawaya, V. Sassanis, S. Yassir, and A. Sescu. Assessment of the impact of two-dimensional wall deformation shape on high-speed boundary-layer disturbances. *AIAA Journal*, 56(12):4787–4800, 2018. doi:10.2514/1.J057045.

[42] A. Towne, O. T. Schmidt, and T. Colonius. Spectral proper orthogonal decomposition and its relationship to dynamic mode decomposition and resolvent analysis. *Journal of Fluid Mechanics*, 847:821–867, 2018.

[43] A. Hameed, N. J. Parziale, L. Paquin, C. Butler, and S. J. Laurence. Spectral analysis of a hypersonic boundary layer on a right, circular cone. In *AIAA SciTech 2020 Forum*, 2020. doi:10.2514/6.2020-0362.

[44] D. Brillinger. An introduction to polyspectra. *The Annals of Mathematical Statistics*, 36(5):1351–1374, 1965. doi:10.1214/aoms/1177699896.

[45] S. A. Craig, R. A. Humble, J. W. Hofferth, and W. S. Saric. Nonlinear behaviour of the mach mode in a hypersonic boundary layer. *Journal of Fluid Mechanics*, 872:74–99, 2019. doi:10.1017/jfm.2019.359.

[46] Y. C. Kim and E. J. Powers. Digital bispectral analysis and its applications to nonlinear wave interactions. *IEEE Transactions on Plasma Science*, (2):120–131, 1979.

[47] M. J. Hinich and M. Wolinsky. Normalizing bispectra. *Journal of Statistical Planning and Inference*, 130:405–411, 2005.

[48] N. Chokani, D. A. Bountin, A. N. Shiplyuk, and A. A. Maslov. Nonlinear aspects of hypersonic boundary-layer stability on a porous surface. *AIAA Journal*, 43(1):149–155, 2005. doi:10.2514/1.9547.

[49] A. N. Shiplyuk, D. A. Bountin, A. A. Maslov, and N. Chokani. Nonlinear interactions of second mode instability with natural and artificial disturbances. 2003. AIAA Paper No. 2003-787.

[50] Chang C.-L. Langley stability and transition analysis code (lastrac) version 1.2 user manual. In *NASA TM-2004-213233*. NASA, 2004.

[51] M. J. Wright, G. V. Candler, and D. Bose. Data-parallel line relaxation method for the navier-stokes equations. *AIAA Journal*, 36(9):1603–1609, 1998.

[52] H. Johnson. Thermochemical interactions in hypersonic boundary-layer stability. In *Ph.D. Thesis*. University of Minnesota, Minneapolis, Minnesota, 2000.